Single-Electron Spin Qubits in Silicon for Quantum Computing

Hu, Guangchong; Huang, Wei Wister; Cai, Ranran; Wang, Lin; Yang, Chih Hwan; Cao, Gang; Xue, Xiao; Huang, Peihao; He, Yu

DOI
10.34133/icomputing.0115

Publication date
2025

Document Version
Final published version

Published in
Intelligent Computing

Intelligent Computing
A SCIENCE PARTNER JOURNAL

REVIEW ARTICLE

Single-Electron Spin Qubits in Silicon for Quantum Computing

Guangchong Hu[1,2,†], Wei Wister Huang[3†], Ranran Cai[4,5†], Lin Wang[6], Chih Hwan Yang[7], Gang Cao[4,5,2], Xiao Xue[8,2,1*], Peihao Huang[2,1,*], and Yu He[2,1,*]

[1]International Quantum Academy, Shenzhen 518048, China. [2]Hefei National Laboratory, Hefei 230088, China. [3]Department of Physics, Faculty of Science, National University of Singapore, Singapore 117551, Singapore. [4]CAS Key Laboratory of Quantum Information, University of Science and Technology of China, Hefei, Anhui 230026, China. [5]CAS Center for Excellence in Quantum Information and Quantum Physics, University of Science and Technology of China, Hefei, Anhui 230026, China. [6]Department of Physics, University of Konstanz, D-78457 Konstanz, Germany. [7]School of Electrical Engineering and Telecommunications, University of New South Wales, Sydney, New South Wales, Australia. [8]QuTech and Kavli Institute of Nanoscience, Delft University of Technology, 2628 CJ Delft, Netherlands.

*Address correspondence to: xueqinfo@gmail.com (X.X.); huangpeihao@iqasz.cn (P.H.); hey@iqasz.cn (Y.H.)
†These authors contributed equally to this work.

Citation: Hu G, Huang WW, Cai R, Wang L, Yang CH, Cao G, Xue X, Huang P, He Y. Single-Electron Spin Qubits in Silicon for Quantum Computing. *Intell. Comput.* 2025;4:Article 0115. https://doi.org/10.34133/icomputing.0115

Submitted 14 August 2024
Revised 26 January 2025
Accepted 12 February 2025
Published 2 May 2025

The recent decade has witnessed substantial advancements in silicon quantum computing. Important milestones include demonstrations of quantum gates exceeding the fault-tolerance threshold, high-fidelity single-shot spin readout, hot quantum bits (hot qubits), and compact scalable spin arrays. Silicon qubits hold promise to leverage semiconductor industry technologies into scalable qubit manufacturing. Both the academic and industry communities are striving to push this advantage into reality. However, formidable challenges persist in the quest to develop a fully operational universal quantum computer. This review focuses on single-spin qubits in silicon. First, we start with foundational spin qubit theory. Then, we discuss gate-defined quantum dots and donor dot systems, with a particular emphasis on two-qubit gate operations and the scalability of qubit arrays. Lastly, we address long-distance coupling, highlighting key areas for future research and potential scale-up strategies for this rapidly evolving field.

Introduction

Quantum computing has been developed for over four decades [1] and is one of the major themes of the second quantum revolution [2]. It has garnered increasing global attention due to accelerating breakthroughs and vast potential for application in a wide variety of industries and fields. Quantum computers, as disruptive computation machines, harness quantum phenomena such as superposition, interference, and entanglement, providing exponential speed-ups in solving critical tasks [3–5]. Quantum computing is widely anticipated to revolutionize various sectors such as chemistry, drug design, economics, and national security. Now, we are in the noisy intermediate scale quantum (NISQ) era [6]. Superconducting and photonics platforms have showcased quantum advantages [7–12], and superconducting qubits are already on the verge of a break-even point for fault-tolerant logic qubits [13–15]. Several applications, including topological braiding operations [16], solving computationally complex problems in the analog quantum simulation approach [17], and time crystals [18], have already been demonstrated. Recently, trapped-ion and neutral-atom systems have pushed quantum gate fidelities and qubit numbers to higher levels [19,20]. These advancements have bolstered confidence in realizing a universal quantum computer, a previously formidable goal that now appears reachable.

Although millions of physical qubits are deemed necessary for a universal quantum computer to fulfill its potential [15,21,22], only a few hundred qubits are available in the NISQ era. Despite attempts to reduce the size of this considerable gap, challenges remain, especially considering the need for long-distance qubit coupling and high-efficiency quantum memory [23]. Moreover, the need for bulky controlling electronics contributes to the high cost of systems with millions of qubits. Among the various physical quantum computing platforms under study, silicon spin qubits stand out due to their compatibility with existing semiconductor industry fabrication processes [24–28]. This unique feature holds the promise of leveraging the semiconductor industry's know-how and technologies to scale up quickly. In addition to this prominent advantage, silicon spin qubits also possess distinctive properties and have seen increasingly rapid progress in recent years.

The fundamental building block of spin-based silicon quantum computing is the spin qubit, which stores quantum information

processed through electrical or magnetic operations [29]. Silicon spin qubits have emerged as suitable platforms for universal quantum computing due to their remarkable attributes, which include long coherence times up to 0.5 s [30], single-qubit gate fidelities exceeding 99.95% [31–34], and two-qubit gate fidelities surpassing the fault-tolerant threshold [26,33,35–42]. Recent advancements made by several research groups have expanded these capabilities to control small qubit arrays and perform multiqubit operations [43,44]. Additionally, silicon spin qubits excel in operating as "hot qubits", achieving functionality at or above 1 K [45–47], even demonstrating fault-tolerant operations at this temperature [38]. Combined with research on cryogenic complementary metal-oxide-semiconductor (cryo-CMOS) technologies [48,49], the silicon spin qubit offers the possibility of integrating quantum computers into a quantum-classical hybrid chip, and perhaps also the possibility of a quantum system-on-chip (QSoC). Companies and research institutes including Intel [25], CEA-Leti [27], HRL Laboratories [42], and IMEC [50] have made strides in manufacturing foundry-compatible silicon quantum computing chips. These recent advancements have shined a light on integrating silicon spin qubits into a large system for future large-scale universal quantum computers (see Fig. 1 for milestone advancements in silicon quantum computing).

Amid the development of silicon quantum dot systems, electron spin qubits are becoming more important than other silicon qubit types, such as charge qubits [51,52], singlet–triplet qubits [53,54], valley qubits [55], and exchange-only qubits [42,56,57]. Spin qubit operation technologies, readout methods, and scaling architectures are becoming more mature. Electron spins confined within silicon quantum dots exhibit prolonged coherence times and can operate at fault-tolerant quantum gate fidelity, distinguishing themselves as prominent qubits in silicon. Meanwhile, hole spin qubits benefit from different physical mechanisms compared to electron spin qubits: strong spin orbital coupling, weak nuclear hyperfine oscillation, and absence of degenerate valleys. Hole spin qubits in silicon-based quantum systems have demonstrated appealing quantum computing capabilities, such as single-qubit gate operation with high fidelity (over 99.97%) [40], two-qubit gates with a fidelity of 99.3% [40], and strong spin–photon coupling [58]. In this review, we focus on electron spin systems, including gate-defined quantum dots and donor-based quantum dots. For details on hole spins in silicon, readers are directed to the relevant literature [47,59,60]. In a gate-defined quantum dot, gate electrodes on top of semiconductor devices provide electrical confinement that captures electrons from a two-dimensional electron gas (2DEG). In a donor-based quantum

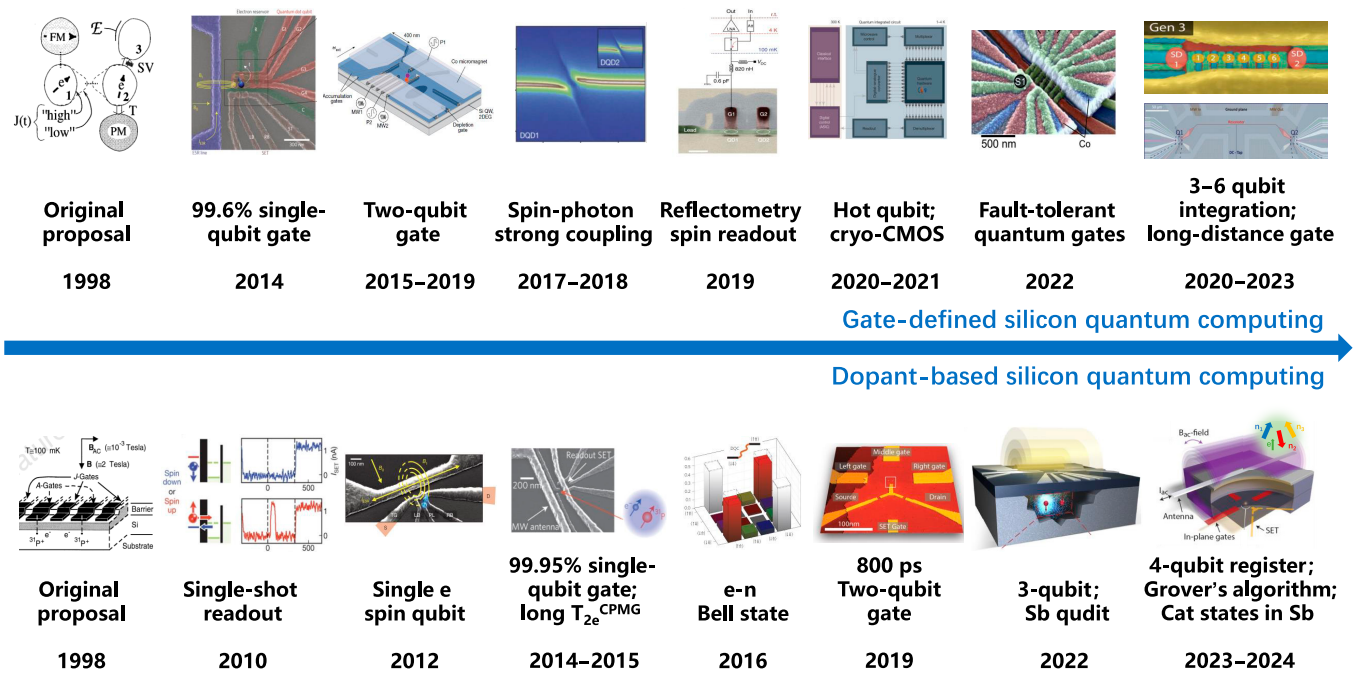

Fig. 1. Milestone advancements in donor-based and gate-defined silicon quantum computing. Along the development timeline, we show the essential achievements and the year or period in which they occurred. The milestone works of gate-defined quantum dots are listed in the top panel, including the original proposal [113], the high-fidelity single-qubit gate [87], a serial of two-qubit gates [102,175,180,183,187,320], the strong coupling of an electron and cavity photon [294,295,321], the refractometry-based single lead or cavity dispersive spin readout [283,322,323], hot qubits [45,46] and related cryo-CMOS controller [48], fault-tolerant quantum gates [33,35,36], the 3-qubit entanglement [324] and 6-qubit integration [43], and the microwave photon mediated long-distance two-spin interaction [293,305] and two-qubit gate via cavity [258]. In the bottom panel, the critical works of donor-based quantum computing include the original proposal [204], the single-shot spin readout [207], the single electron spin qubit in natural silicon [208], the long coherence times of an electron spin and a nuclear spin [30], the high-fidelity single-qubit gate [31], the electron spin and nuclear spin entanglement [259], the fast exchange-based two-qubit gate between donors [248], the tripartite entanglement of one electron and two nuclear spins [37] and a high-spin qudit of an antimony donor [325], a high-fidelity 4-qubit register consisting of 3 nuclear spins and one electron spin [260], the demonstration of Grover's algorithm and above fault-tolerant gates on this 4-qubit device [41], and the creation and manipulation of Schrödinger cat states on an Sb donor [310]. Building on these technological advancements, donor-based and gate-defined silicon quantum computing are poised for scaling up the systems, though difficult challenges still lie ahead. The images in the top panel are adapted from our own work [87, 322], Springer Nature; from [45, 183, 294] with permission, Springer Nature; from [113] with permission, the American Physical Society; from [33] with permission, American Association for the Advancement of Science (AAAS); and from [43], Springer Nature, under a CC BY license. The images in the bottom panel are adapted from our own work [248], Springer Nature; from [30, 37, 204, 207, 208, 259] with permission, Springer Nature; and from [260], Springer Nature, under a CC BY license.

dot, the dopant potential binds electrons around its nuclei, and the hyperfine interaction links the electron spins to their respective nuclear spins, providing excellent physical degrees of freedom for encoding qubits [61,62].

This review has 4 main sections. The first section delves into the theory of electron spin qubits. The next 2 sections review gate-defined quantum dots and donor-based quantum dots. Each of these 2 sections covers basic fabrication processes, qubit state preparation and measurements, and the implementation of quantum gates, and especially toward scaling up, reviews and perspectives on the two-qubit gate and quantum dot array are emphasized. The last section discusses long-distance coupling, which is crucial for increasing the number of qubits and enabling distributed quantum computing architectures.

Basic Theory

Modeling of quantum dots

A semiconductor quantum dot, also called an artificial atom, has an electronic structure that depends on the shape of the quantum dot and the band structure of the semiconductor [63,64]. In a semiconductor, the electrons stay at the conduction band minimum, and the holes are at the top of the valence band. In the following, we discuss the model Hamiltonian of electrons in semiconductor quantum dots.

If there are multiple electrons in silicon quantum dots, the Coulomb interaction between the electrons plays an important role. Consider N electrons in arrays of quantum dots. The quantum dots can be formed by either the electric potential of the electrodes or the potential of the nuclei of the dopant in silicon. Then, the Hamiltonian is

$$H = \sum_i h_i + \sum_{ij} H_{C,ij}, \tag{1}$$

where h_i and $H_{C,ij}$ are the single-particle and two-particle terms.

In silicon, there are 6 degenerate valley states in the bulk. In the presence of confinement, the valley states split, and the single-particle Hamiltonian is

$$h_i = \sum_j h_{i,1-\text{valley}} |j\rangle\langle j| + \sum_{j,k} c_{jk} |j\rangle\langle k|, \tag{2}$$

where the single-particle Hamiltonian $h_{i,1-\text{valley}}$ is assumed to be valley independent, and the valley coupling c_{jk} depends on the details in the atomic scale, such as interface disorder, steps, and.

For electrons in semiconductor quantum dots, the single-particle Hamiltonian of the ith electron in a single jth valley (i.e., one of the conduction band minimum) can be written as

$$h_{i,1-\text{valley}} = \frac{p_i^2}{2m^*} + V_D(\vec{r}_i) + H_{Z,i} + H_{SO,i} + H_{A,i}, \tag{3}$$

where the first term is the kinetic energy of the ith electron, $V_D(\vec{r})$ is the electrical potential of the quantum dots the electron experiences, the last three terms are due to the Zeeman interaction, the spin-orbit interaction (SOI), and the hyperfine interaction. Here, $\vec{r}_i$ and $\vec{p}_i = -i\hbar\vec{\nabla}_i - q\vec{A}(\vec{r}_i)/c$ are the coordinate and momentum operator of the ith electron, m^* is the effective mass of the electron, $q = -|e|$ is the charge of the electron, and $\vec{A}(\vec{r}_i)$ is the vector potential.

The potential $V_D(\vec{r})$ is tunable electrically via the metallic electrodes, and it can also be the Coulomb potential of the nuclei of the dopant. In the case of a dopant, $V_D(\vec{r}) = V_G(\vec{r}) + V_N(\vec{r})$, where $V_G(\vec{r})$ is the potential due to the electrodes, and the additional Coulomb potential $V_N(\vec{r}_i)$ that the electron experiences is

$$V_N(\vec{r}_i) = \sum_j \frac{N_j e^2}{\epsilon|\vec{r}_i - \vec{R}_j|}, \tag{4}$$

where N_j and $\vec{R}_j$ are the charge and position of the jth nuclei, and ϵ is the permittivity in the semiconductor material. When magnetic field $\vec{B}$ presents, there is Zeeman splitting for the electron spins. The corresponding Hamiltonian for the ith electron is $H_{Z,i} = g\mu_B\vec{B}\cdot\vec{S}_i = \frac{E_{Z,i}}{2}\sigma_{i,Z}$, where $E_{Z,i}$ is the Zeeman energy of the ith electron.

In semiconductor quantum dot systems, there is also SOI that is important for spin qubit operations. Possible SOI mechanisms include the intrinsic SOI in the material and the synthetic SOI induced by the external inhomogeneous magnetic field. The intrinsic SOI includes the Dresselhaus SOI due to the bulk inversion symmetry breaking and the Rashba SOI due to the structural inversion symmetry breaking [65–68]. For example, the Rashba SOI in $H_{SO,i}$ can be given by

$$H_{R,SO,i} = \alpha_{\text{so}}\vec{E}\times\vec{p}_i\cdot\vec{\sigma}_i, \tag{5}$$

where α_{so} denotes the strength of the SOI, $\vec{E}$ is the electric field, and $\vec{p}_i$ and $\vec{\sigma}_i$ are the momentum and spin operators of the ith electron.

In the presence of the nuclear spins near the quantum dots, there is hyperfine interaction between the electron spins and the nuclear spins, $H_{A,i} = \sum_j H_{A,ij}$, where

$$H_{A,ij} = A_{ij}\vec{S}_i\cdot\vec{I}_j, \tag{6}$$

where A_j is the hyperfine interaction between the electron and the nuclei in jth quantum dot when the electron is localized in the quantum dot. S_i and I_j are the electron and nuclear spin operators of the ith electron and the jth nuclei.

The physics is governed by the total Hamiltonian $H = \sum_i h_i + \sum_{ij} H_{C,ij}$, where the Coulomb interaction between the ith and the jth electron is

$$H_{C,ij} = H_C(\vec{r}_i, \vec{r}_j) = \frac{e^2}{\epsilon|\vec{r}_i - \vec{r}_j|}. \tag{7}$$

One can solve the problem by using the full configuration interaction (FCI) method, where the basis for the many-electron system is constructed from the Slater determinants of a set of single-particle states. By increasing the size of the basis (i.e., increasing the number of single-particle states), results can be obtained until convergence.

The FCI method requires expansive computational resources even for a small number of quantum dots. To a good approximation in many cases, one can choose only a single orbital state $\Phi_i(\vec{r})$ for each quantum dot, and then construct the many-body wave function as basis states. Then, the system Hamiltonian can be written in the second quantization representation.

In the absence of SOI and hyperfine interaction, the Hamiltonian of the quantum dot system after the second quantization can be modeled by an extended Hubbard model (see [69]):

$$\begin{aligned} H = & \sum_{i\sigma} \epsilon_{i\sigma} c_{i\sigma}^{\dagger} c_{i\sigma} + \sum_{ij\sigma} \left(t_{ij} c_{i\sigma}^{\dagger} c_{j\sigma} + h.c. \right) \\ & + \sum_{i} U_i \hat{n}_{i\uparrow} \hat{n}_{i\downarrow} + \sum_{ij\sigma} V_{C,ij} \hat{n}_{i\sigma} \hat{n}_{j\sigma} \\ & + \sum_{ij\sigma\neq\sigma'} J_{C,ij} c_{i\sigma}^{\dagger} c_{j\sigma'}^{\dagger} c_{j\sigma'} c_{i\sigma} + \sum_{ij\sigma} W_{ij} \hat{n}_{i\sigma} c_{j\sigma}^{\dagger} c_{i\sigma}, \end{aligned} \tag{8}$$

where the detuning $\epsilon_{i\sigma}$ and tunneling t_{ij} is tunable by the gate voltages, and the interaction energies U_i, $V_{C,ij}$, $J_{C,ij}$, W_{ij} are determined by the sizes of the quantum dots and distances between the quantum dots.

Effective Hamiltonian of spin qubits

From the extended Hubbard model, one can further study the interaction of spins and define different types of spin qubits.

For simplicity, we consider the unit of two electrons in a double quantum dot (DQD). Then, the Hamiltonian is

$$\begin{aligned} H = & \sum_{i=1,2;\sigma} \left(\epsilon_i + \frac{E_{Z,i}}{2} \sigma \right) c_{i\sigma}^{\dagger} c_{i\sigma} + \left(t_{12} c_{1\sigma}^{\dagger} c_{2\sigma} + h.c. \right) \\ & + \sum_{i=1,2} U_i \hat{n}_{i\uparrow} \hat{n}_{i\downarrow} + \sum_{\sigma} V_{C,12} \hat{n}_{1\sigma} \hat{n}_{2\sigma}, \end{aligned} \tag{9}$$

where $i = 1, 2$ denotes the two sites of the quantum dots. The system can host different numbers of electrons. Next, we consider the single-electron and the two-electron cases separately.

Single-electron system

If there is only one electron, the system Hamiltonian without a spin degree of freedom can be simplified as

$$H_0^C = \frac{\epsilon}{2} \sigma_z^C + t \sigma_x^C, \tag{10}$$

where $\epsilon = \epsilon_2 - \epsilon_1$ and $t = t_{12}$ are the detuning and the tunneling between the left and the right dot, respectively, and $\sigma_z^C = c_{2\sigma}^{\dagger} c_{2\sigma} - c_{1\sigma}^{\dagger} c_{1\sigma}$ and $\sigma_x^C = c_{1\sigma}^{\dagger} c_{2\sigma} + c_{2\sigma}^{\dagger} c_{1\sigma}$ are the operators for the charge states in the system.

Then, a charge qubit can be defined by the eigenstates $|0_C\rangle$ and $|1_C\rangle$ of the Hamiltonian. If the localized states at the two dots are $|L\rangle$ and $|R\rangle$, then the eigenstates of the charge qubit are $|0_C\rangle = \cos(\theta/2)|L\rangle + \sin(\theta/2)|R\rangle$ and $|1_C\rangle = -\sin(\theta/2)|L\rangle + \cos(\theta/2)|R\rangle$. In the presence of a driving electric field $E_{\mathrm{ac}}(t)$, the detuning between the two dots becomes time dependent $\epsilon = \epsilon_0 + \epsilon_1(t)$, where $\epsilon_1 = eE_{\mathrm{ac}}(t)d_0$ and d_0 is the distance between the two dots. Thus, we have $H^C = H_0^C + H_1^C$, where $H_1^C = \epsilon_1(t)/2\sigma_z$. Since the charge qubit is not only coupled to the driving electric field, but also coupled to the noisy electric field in the environment, the coherence of the charge qubit is usually as short as 10 ns [70]. By engineering the energy-level structure of the charge qubit, the dephasing time can also be extended to be around 200 μs [71].

A spin qubit in a quantum dot is of great interest since it is better protected from electrical noise. In the presence of the SOI and external magnetic field, the single-electron Hamiltonian is

$$H_0 = \frac{E_Z}{2} \sigma_z + \frac{\epsilon}{2} \sigma_z^C + t \sigma_x^C + \sum_{ij} \alpha_{\mathrm{so},ij} \sigma_i \sigma_j^C, \tag{11}$$

where $E_Z = g\mu_B B$ is the Zeeman splitting of the electron spin in an external magnetic field $\vec{B}$. Here, the strength of the SOI is $\alpha_{\mathrm{so},ij}$. The spin qubit is defined by the eigenstates of the spin Hamiltonian.

When an external oscillating alternating current (AC) magnetic field $B_{\mathrm{ac}}(t)$ is applied along the x-axis, an electron spin resonance (ESR) operation can be induced. Since the mixing between the spin and the charge states is relatively weak, the Hamiltonian of the spin qubit is approximately

$$H^S = H_0^S + H_1^S, \tag{12}$$

with $H_0^S = E_Z \sigma_z / 2$ and $H_1^S = g\mu_B B_{\mathrm{ac}}(t)\sigma_x / 2$. If $B_{\mathrm{ac}}(t) = B_{\mathrm{ac0}} \cos\left(\omega_{\mathrm{ac}} t + \phi_{\mathrm{ac}}\right)$ is perpendicular to the external magnetic field $\vec{B}$, where ω_{ac} and ϕ_{ac} are the frequency and the phase of the applied AC magnetic field, then the Rabi frequency of the electron spin is $\Omega_R = g\mu_B B_{\mathrm{ac0}}$.

Because of the SOI, the spin and charge states are mixed, which allows for electric manipulation of the spin states. The electric field couples to the charge dipole of the charge qubit and induces a type of spin resonance called electric dipole spin resonance (EDSR). In the presence of an oscillating electric field, the Hamiltonian of the spin-charge qubit is $H = H_0 + H_1$, where H_0 is the H_0 defined above, and $H_1 = H_1^C = \epsilon_1(t)\sigma_z / 2$. Thus,

$$\begin{aligned} H = & \frac{E_Z}{2} \sigma_z + \frac{\epsilon}{2} \sigma_z^C + t \sigma_x^C \\ & + \sum_{ij} \alpha_{\mathrm{so},ij} \sigma_i \sigma_j^C + \frac{\epsilon_1(t)}{2} \sigma_z^C, \end{aligned} \tag{13}$$

which is simplified as if we consider only the spin degree of freedom,

$$H_{\mathrm{eff}} = \frac{E_Z}{2} \sigma_z + \frac{1}{2} g\mu_B B_{\mathrm{eff}}(t) \sigma_x, \tag{14}$$

where the effective oscillating magnetic field $B_{\mathrm{eff}}(t)$ is due to the oscillating electric field $\epsilon_1(t) = eE_{\mathrm{ac}}(t)d_0 = eE_{\mathrm{ac0}}d_0 \cos\left(\omega_{\mathrm{ac}} t + \phi_{\mathrm{ac}}\right)$ and the SOI. The physics of the Rabi oscillation due to the EDSR is thus similar to the ESR. The Rabi frequency $\Omega_{R,\mathrm{EDSR}}$ due to $B_{\mathrm{eff}}(t)$ is proportional to the strength E_{ac0} of the electric field and the strength α_{so} of the SOI.

In the case of the EDSR, the SOI can be provided by an intrinsic SOI such as the Dresselhaus SOI due to bulk inversion symmetry breaking, or the Rashba SOI due to structural inversion symmetry breaking [65–68]. In the case of the gate-defined quantum dot, the Rashba SOI is $H_R = \alpha_R \left(p_x \sigma_y - p_y \sigma_x \right)$, where α_R is the coupling strength of the Rashba SOI, $\vec{p} = \left[p_x, p_y \right]$ is the 2D momentum operator acting on charge states [which can be expressed in the basis of the eigenstates $|0_C\rangle$ and $|1_C\rangle$ of the charge qubit], and the Dresselhaus SOI is $H_D = \alpha_D \left(p_x \sigma_x + p_y \sigma_y \right)$. The SOI can also be the result of an inhomogeneous magnetic field (in which case it is called synthetic SOI) or the hyperfine

coupling field [72–74]. Recently, hole spins are of particular interest due to the large strength of the SOI of holes, and the low effective mass of heavy holes for the in-plane motion in planar Ge [59]. The requirements on nanofabrication are relaxed due to the low effective mass, making the fabrication process less challenging.

The benefits of EDSR include less cross-talk due to rapid decay of the electric field over distance, space savings due to the absence of an ESR line, faster operation speed, and greater ease of generation of electrical fields, compared with the ESR method. However, EDSR relies on the sizable strength of the SOI; thus, charge noise can play a role and causes spin decoherence.

Single-electron and single-hole spin qubits in quantum dots have been studied intensively during the last few years because of their good coherence, fast EDSR manipulation, high-fidelity gate operations, and potential for scalability. However, it is still challenging to scale up such systems due to the difficulty of fabricating small-footprint devices, and there is cross-talk error during spin manipulation in the presence of multiple spin qubits. Seeking to overcome some of these challenges, researchers have studied spin qubits encoded on multiple electrons, such as the ST_0 qubit and exchange-only qubit, which work in lower magnetic fields and operate with baseband pulses [42]. Moreover, two-electron and multielectron (or hole) systems are also essential for two-qubit and multiqubit gates for universal quantum computing. Next, we discuss the Hamiltonian of the two-electron system and then the case of the multielectron system.

Two-electron system

Here, we consider a two-electron system in a DQD, which can be used for the ST_0 qubit or the two-qubit operation of two single-spin qubits. In the presence of two electrons, the relevant two-electron states are denoted as $\left|\left(N_L,N_R\right)X\right\rangle$, where N_L and N_R are the number of electrons in the left and right dot, and $|X\rangle$ is the spin state of the two electrons. For two electrons, the spin state $|X\rangle$ can be the spin-singlet $|S\rangle$ or the spin-triplet states $\left|T_+\right\rangle$, $\left|T_0\right\rangle$, or $\left|T_-\right\rangle$. In the (1,1) charge regime, $|(1,1)X\rangle$ are the 4 lowest states of the system, in which $|(1,1)S\rangle$ is tunnel-coupled to the two doubly occupied states $|(2,0)S\rangle$ and $|(2,0)S\rangle$. If the $J_{C,12}$ and W_{12} terms are negligible, then, from Eq. 8, the two-electron Hamiltonian in the basis of the lowest 3 singlet states is

$$H_S=\begin{bmatrix} 0 & \sqrt{2}t & \sqrt{2}t \\ \sqrt{2}t & U_1-V_c-\epsilon & 0 \\ \sqrt{2}t & 0 & U_2-V_c+\epsilon \end{bmatrix}, \tag{15}$$

where U_i is the on-site Coulomb interaction and V_c is the Coulomb interaction between electrons in the neighboring quantum dots. Because of the tunnel coupling between $|(1,1)S\rangle$ and the doubly occupied singlet states, the singlet state $|(1,1)S\rangle$ is lowered. However, for the triplet state $\left|(1,1)T_m\right\rangle$, there is no such coupling due to the absence of the $\left|(2,0)T_m\right\rangle$ and $\left|(2,0)T_m\right\rangle$ states, according to the Pauli exclusion principle. Thus, the energy of singlet state $|(1,1)S\rangle$ becomes lower than the energy of the triplet state $\left|(1,1)T_m\right\rangle$ (in the absence of a magnetic field), and results in an exchange interaction J. [Note that although $\left|(0,2)T_m\right\rangle_{o_1,o_2}$ are not absent if two electrons are occupying different orbital states $\left|o_1\right\rangle$ and $\left|o_2\right\rangle$ with $\left|(0,2)T_m\right\rangle_{o_1,o_2}$ tunnel-coupled to $\left|(1,1)T_m\right\rangle$, there is also the $|(0,2)S\rangle_{o_1,o_2}$ state that occupies the $\left|o_1\right\rangle$ and $\left|o_2\right\rangle$ orbital states with $|(0,2)S\rangle_{o_1,o_2}$ tunnel-coupled to $|(1,1)S\rangle$, so that the same energy shifts are induced for $\left|(1,1)T_m\right\rangle$ and $|(1,1)S\rangle$ by these tunneling processes, and thus, the presence of $\left|(0,2)T_m\right\rangle_{o_1,o_2}$ and $|(0,2)S\rangle_{o_1,o_2}$ in general does not result in net exchange interaction. Moreover, $\left|(0,2)T_m\right\rangle_{o_1,o_2}$ is also generally too high in energy to be relevant here.] The effective interaction between the two electron spins is

$$H_{ex}=\frac{J}{4}\left(\vec{\sigma}_1\cdot\vec{\sigma}_2-I\right), \tag{16}$$

where $J=\left(2t^2\right)/\left(U_1-V_c-\epsilon\right)+\left(2t^2\right)/\left(U_2-V_c+\epsilon\right)$ is the strength of the exchange interaction, and I is an identity operator. The exchange interaction arises from the quantum mechanical effect of the antisymmetric statistics of the electrons.

In the presence of a magnetic field, there is Zeeman splitting of the spin qubits,

$$\begin{aligned} H_Z&=\frac{1}{2}\sum_{i=1,2}g\mu_B\vec{B}_i\cdot\vec{\sigma}_i \\ &=\frac{\overline{E}_Z}{2}\sum_i\sigma_{i,z}+\frac{\Delta E_Z}{2}\left(\sigma_{1,z}-\sigma_{2,z}\right), \end{aligned} \tag{17}$$

where $\overline{E}_Z=\left(E_{Z,1}+E_{Z,2}\right)/2$ and $\Delta E_Z=\left(E_{Z,1}-E_{Z,2}\right)/2$ are the average Zeeman splitting and the difference between the Zeeman splittings in the left and right quantum dots. The Zeeman energy difference ΔE_Z can arise from the inhomogeneous magnetic field, g-factor inhomogeneity, hyperfine coupling of electrons and nuclear spins, etc. Then, the Hamiltonian $H=H_Z+H_{ex}$ is

$$H=\frac{\overline{E}_Z}{2}\sum_i\sigma_{i,z}+\frac{\Delta E_Z}{2}\left(\sigma_{1,z}-\sigma_{2,z}\right)+\frac{J}{4}\left(\vec{\sigma}_1\cdot\vec{\sigma}_2-I\right). \tag{18}$$

From the Hamiltonian, various two-qubit gates can be constructed. Moreover, a two-electron singlet–triplet (ST_0) qubit can be defined by the eigenstates of the Hamiltonian in the $|(1,1)S\rangle$ and $\left|(1,1)T_0\right\rangle$ subspace. Since the exchange $J(\epsilon)$ is tunable via the detuning of the DQD through the dc pulsing of the detuning ϵ or by directly pulsing the tunnel barrier as is often done, e.g., for high-fidelity two-qubit gates [24], universal single-qubit operation of the ST_0 qubit can be constructed based on the Hamiltonian with tunable exchange interaction (detailed forms of two-qubit gates are discussed below in the subsection on qubit operations).

Once we have the effective Hamiltonian of the two-electron system, we can further obtain the three-spin Hamiltonian that is coupled by the exchange interaction. We have

$$H=\sum_{i=1,2}\frac{J_{i,i+1}}{4}\vec{\sigma}_i\cdot\vec{\sigma}_{i+1}+\sum_{i=1,2,3}\frac{E_{Z,i}}{2}\sigma_{z,i}, \tag{19}$$

where J_{ij} is the exchange interaction between the neighboring spins, and $E_{Z,i}$ is the Zeeman splitting of an electron in the ith quantum dot. The exchange-only qubit can be defined by the two eigenstates of the Hamiltonian.

In a more general case, we have

$$H=\sum_{\langle ij\rangle}\frac{J_{ij}}{4}\vec{\sigma}_i\cdot\vec{\sigma}_j+\sum_i\frac{E_{Z,i}}{2}\sigma_{z,i}. \tag{20}$$

From the above Hamiltonian, various interesting spin physics and operations of spin qubits in the system can be studied.

Qubit operations

The interaction Hamiltonian between the electron spins and the electromagnetic fields allows the operations of the single-qubit and the two-qubit gates of the spin qubits. In the following, we discuss how to construct these gates based on the effective Hamiltonian of the single-electron and two-electron systems.

Single-qubit operations

The interaction between an electron spin and a magnetic field results in an energy difference between the spin $|\uparrow\rangle$ and $|\downarrow\rangle$ states. The electron spin's behavior in a static magnetic field is described by a Hamiltonian that can be manipulated with an AC magnetic field perpendicular to the static field to drive spin transitions. If the AC magnetic field is $\vec{B}_{\mathrm{ac}} = B_{\parallel}\cos(\omega_{\mathrm{ac}}t+\phi_{\mathrm{ac}})\hat{x}$, then the Hamiltonian Eq. 12 becomes:

$$H = \frac{E_Z}{2}\sigma_z + \frac{g\mu_{\mathrm{B}}B_{\parallel}}{2}\left(I\cos(\omega_{\mathrm{ac}}t)+Q\sin(\omega_{\mathrm{ac}}t)\right)\sigma_x, \quad (21)$$

where $I = \sin\phi_{\mathrm{ac}}$ and $Q = \cos\phi_{\mathrm{ac}}$. For ease of understanding, the magnetic field is aligned along the $+\hat{z}$ direction, with the Hamiltonian expressed as $H = g\mu_{\mathrm{B}}\boldsymbol{B}\cdot\boldsymbol{\sigma}/2 = E_Z\sigma_z/2$, where g is the Landé g-factor, μ_{B} is the Bohr magneton, $\boldsymbol{B}$ signifies the magnetic field strength, and $\boldsymbol{\sigma}$ signifies the Pauli matrices. The oscillating electromagnetic wave component, represented by the off-diagonal elements, is used to control the qubit. The in-phase (I) and quadrature (Q) components of the microwave, alongside the applied microwave frequency ω_{ac}, are crucial for this control. For simplicity, the AC magnetic field is aligned along the $\hat{x}$-axis.

Under the rotating frame transformation and rotating wave approximation, where rapidly oscillating terms $e^{\pm 2i\omega_{\mathrm{ac}}t}$ are neglected for simplicity [75], the transformation is governed by the Hamiltonian $H_{\mathrm{RWA}} = UHU^{\dagger} - i\hbar\frac{\partial U}{\partial t}U^{\dagger}$. The unitary transformation U is represented by the matrix $\begin{pmatrix} e^{\frac{i\omega t}{2}} & 0 \\ 0 & e^{\frac{-i\omega t}{2}} \end{pmatrix}$, with $\hbar\omega = g\mu_{\mathrm{B}}B$ and $\hbar\Omega_{\parallel} = g\mu_{\mathrm{B}}B_{\parallel}$. The resulting Hamiltonian in the rotating wave approximation is expressed as:

$$H_{\mathrm{RWA}} = \frac{\hbar}{2}(\omega-\omega_{ac})\sigma_z + \frac{\hbar\Omega_{\parallel}}{2}I\sigma_x + \frac{\hbar\Omega_{\parallel}}{2}Q\sigma_y. \quad (22)$$

The pulse duration and I/Q component of the microwave define the spin's rotation angle and axis, respectively. For on-resonance driving, the AC field fully rotates the spin from $|\downarrow\rangle$ to $|\uparrow\rangle$. The symbols $X_{\frac{\pi}{2}}$ and $Y_{\frac{\pi}{2}}$ indicate 90° rotations around the $\hat{x}$- and $\hat{y}$-axes, enabling arbitrary two-axis control within the SU(2) group.

Two-qubit operations

A universal quantum gate set must include single-qubit rotations and at least one two-qubit entangling gate. For Loss–DiVincenzo (LD) qubits in quantum dots, the direct exchange interaction, resembling Heisenberg-like coupling, is the primary method for executing two-qubit gates. This occurs when electron wave functions overlap in 3 dimensions, enabling spin coupling and various two-qubit gates (refer to the "Two-qubit gates and entanglement" subsection under the "Gate-Defined Quantum Dots" section below).

From the two spin-qubit Hamiltonian Eq. 18, the two-electron spin Hamiltonian in the presence of a driving magnetic field is

$$\begin{aligned} H = {} & \frac{\overline{E}_Z}{2}\sum_i \sigma_{i,z} + \frac{\Delta E_Z}{2}\left(\sigma_{1,z}-\sigma_{2,z}\right) \\ & + \frac{J}{4}\left(\vec{\sigma}_1\cdot\vec{\sigma}_2 - I\right) + \sum_{i=1,2}\frac{g\mu_{\mathrm{B}}}{2}B_{i,\mathrm{ac}}(t)\sigma_{i,x}, \end{aligned} \quad (23)$$

where $B_{i,\mathrm{ac}}(t)$ is the AC magnetic field acting on the ith electron spin. Based on the Hamiltonian, several different two-qubit gates can be constructed. Below, we discuss the basic principles of the SWAP gate, the controlled-phase (CPHASE) gate, and the resonant controlled-not (CNOT) gate.

SWAP gates: When $\Delta E_Z \ll J$ and $B_{i,\mathrm{ac}} = 0$, the exchange interaction dominates the Hamiltonian Eq. 23. At a given J, with a controlled duration of the exchange interaction, an entangling $\sqrt{\mathrm{SWAP}}$ gate can be achieved by setting $t = 1/(4J)$:

$$U_{\sqrt{\mathrm{SWAP}}} = e^{-iH_{\mathrm{ex}}t/\hbar}\Big|_{t=\frac{1}{4J}} = \begin{pmatrix} 1 & 0 & 0 & 0 \\ 0 & \frac{1}{\sqrt{2}} & \frac{-i}{\sqrt{2}} & 0 \\ 0 & \frac{-i}{\sqrt{2}} & \frac{1}{\sqrt{2}} & 0 \\ 0 & 0 & 0 & 1 \end{pmatrix}. \quad (24)$$

When the $\sigma_{z1}\sigma_{z2}$ term is absent in the exchange Hamiltonian, which resembles the interaction between distant spins mediated by virtual photons in a resonator, the operator above turns into an $\sqrt{\mathrm{iSWAP}}$ gate (refer to the "Spin–Photon Interface for Scaling up" section below).

CPHASE gates: When $\Delta E_Z \gg J$ and $B_{i,\mathrm{ac}} = 0$, in the rotating frame of the $|\downarrow\uparrow\rangle, |\uparrow\downarrow\rangle$ space, the time-dependent evolution operator of the Hamiltonian Eq. 23 becomes a CPHASE gate:

$$U_{\mathrm{CPHASE}}(t) = \begin{pmatrix} 1 & 0 & 0 & 0 \\ 0 & e^{i\pi Jt/\hbar} & 0 & 0 \\ 0 & 0 & e^{-i\pi Jt/\hbar} & 0 \\ 0 & 0 & 0 & 1 \end{pmatrix}. \quad (25)$$

When $2\pi Jt = (2n+1)\pi$ with n integer, this operator produces a controlled-Z (CZ) gate together with single-qubit Z rotations:

$$U_{CZ} = Z_1\left(\frac{\pi}{2}\right)Z_2\left(\frac{\pi}{2}\right)U_{\mathrm{CPHASE}}\left(\frac{1}{2J}\right) = \begin{pmatrix} 1 & 0 & 0 & 0 \\ 0 & 1 & 0 & 0 \\ 0 & 0 & 1 & 0 \\ 0 & 0 & 0 & -1 \end{pmatrix}. \quad (26)$$

Resonant CNOT gates: CNOT gates can be compiled by using a $\sqrt{\mathrm{SWAP}}$ gate or a CPHASE gate together with additional single-qubit gates. The Hamiltonian Eq. 23 in the two-spin basis $(\uparrow\uparrow, \uparrow\downarrow, \downarrow\uparrow, \downarrow\downarrow)$ can be approximated as [76]

$$H=\frac{1}{2}\begin{pmatrix} 2\overline{E}_Z & \gamma_2 B_1 & \gamma_1 B_1 & 0 \\ \gamma_2 B_1^* & \Delta E_Z - J & J & \gamma_1 B_1 \\ \gamma_1 B_1^* & J & -\Delta E_Z - J & \gamma_2 B_1 \\ 0 & \gamma_1 B_1^* & \gamma_2 B_1^* & -2\overline{E}_Z \end{pmatrix}, \quad (27)$$

Here, $\gamma_{n\downarrow}(\gamma_{n\uparrow})$is the effective gyromagnetic ratio that couples qubit n to the oscillating magnetic field B_1. The Hamiltonian can be diagonalized into the new basis $(\uparrow\uparrow, \tilde{\uparrow\downarrow}, \tilde{\downarrow\uparrow}, \downarrow\downarrow)$:

$$H=\frac{1}{2}\begin{pmatrix} 2\overline{E}_Z & \gamma_{2\uparrow} B_1 & \gamma_{1\uparrow} B_1 & 0 \\ \gamma_{2\uparrow} B_1^* & \Delta\tilde{E}_Z - J & 0 & \gamma_{1\downarrow} B_1 \\ \gamma_{1\uparrow} B_1^* & 0 & -\Delta\tilde{E}_Z - J & \gamma_{2\downarrow} B_1 \\ 0 & \gamma_{1\downarrow} B_1^* & \gamma_{2\downarrow} B_1^* & -2\overline{E}_Z \end{pmatrix}, \quad (28)$$

where $\Delta\tilde{E}_z=\sqrt{J^2+\Delta E_Z^2}$, and $|\tilde{\downarrow\uparrow}\rangle=\cos\frac{\theta}{2}|\downarrow\uparrow\rangle+\sin\frac{\theta}{2}|\uparrow\downarrow\rangle$, $|\tilde{\uparrow\downarrow}\rangle=|\tilde{\uparrow\downarrow}\rangle=-\sin\frac{\theta}{2}|\downarrow\uparrow\rangle+\cos\frac{\theta}{2}|\uparrow\downarrow\rangle$, here, $\cos\frac{\theta}{2}=\frac{\Delta E_Z+\sqrt{J^2+\Delta E_Z^2}}{\sqrt{\left(\Delta E_Z+\sqrt{J^2+\Delta E_Z^2}\right)^2+J^2}}$ and $\sin\frac{\theta}{2}=\frac{J}{\sqrt{\left(\Delta E_Z+\sqrt{J^2+\Delta E_Z^2}\right)^2+J^2}}$, and thus the effective gyromagnetic ratios follow the rotation $\gamma_{1\uparrow(1\downarrow)}=\gamma_1\cos\frac{\theta}{2}\mp\gamma_2\sin\frac{\theta}{2}$, $\gamma_{2\uparrow(2\downarrow)}=\gamma_2\cos\frac{\theta}{2}\pm\gamma_1\sin\frac{\theta}{2}$. This results in 4 resonance frequencies, which are $f_{1\uparrow(1\downarrow)}=\overline{E}_Z+\frac{\Delta\tilde{E}_Z\pm J}{2}$, $f_{2\uparrow(1\downarrow)}=\overline{E}_Z+\frac{-\Delta\tilde{E}_Z\pm J}{2}$.

In a time-dependent frame with a rotating matrix $R=\mathrm{diag}\left\{e^{-i\overline{E}_Z t}, e^{-i(\Delta\tilde{E}_Z-J)t}, e^{i(\Delta\tilde{E}_Z+J)t}, e^{i\overline{E}_Z t}\right\}$, applying microwave pulses at one of four selected frequencies leads to a conditional rotation.

In short, the SWAP gate, the CPHASE gate, and the resonant CNOT gate are the two-qubit gates commonly implemented in silicon spin-qubit experiments. By using one of the two-qubit gates and arbitrary single-qubit rotations, it is possible to construct universal quantum logic for silicon spin-based quantum computing.

Spin decoherence in quantum dots

When a quantum system is coupled to a noisy environment, quantum decoherence occurs. We first introduce a general theory for quantum decoherence and then discuss in more detail the decoherence mechanism in semiconductor quantum computing.

If a qubit system is coupled to a noisy environment, in the so-called Markov approximation, the decoherence of the off-diagonal elements of the reduced density matrix is given by [68]

$$1/T_2=1/(2T_1)+1/T_\phi, \quad (29)$$

where the relaxation rate due to the transverse coupling to the noise is

$$\frac{1}{T_1}\approx S_{XX}^{+}(\omega_Z)+S_{YY}^{+}(\omega_Z), \quad (30)$$

where $S_{ii}^{+}(\omega)$ can be rewritten as the Fourier transformation

$$S_{ii}^{+}(\omega)\equiv\frac{g^2\mu_B^2}{2\hbar^2}\int_{-\infty}^{\infty}dt\langle\delta B_i(t)\delta B_i(0)\rangle\cos(\omega t)dt. \quad (31)$$

For the Markovian noise, the pure dephasing is given by $1/T_\phi=S_{ZZ}(\omega=0)$.

In quantum systems, there are non-Markovian types of noise, such as $1/f$ charge noise, where the memory of the environment is long, and the Markov approximation is invalid. Slow noise usually affects the dephasing of the qubit. In this case, the off-diagonal density matrix element for the spin decays in the form $\exp(-\varphi(t))$ with [77,78]

$$\varphi(t)=\int_{\omega_l}^{\omega_h}d\omega S_{ZZ}(\omega)\left[2\sin(\omega t/2)/\omega\right]^2 \quad (32)$$

where ω_h is the high-frequency cutoff and ω_l is the lower cutoff frequency chosen as the inverse of the experiment time. In the presence of low-frequency $1/f$ noise, $S_{ZZ}=A_0/\omega$, the analytical result suggests that spin dephases as $\varphi\propto A_0 t^2\ln t$, which has a nearly quadratic dependence on time [70,79]. Then, the pure dephasing rate is defined as $\varphi(T_\phi)=1$, and the pure dephasing rate shows approximately $1/T_\phi\propto\sqrt{A_0}$ dependence.

In semiconductors, there is nuclear spin noise, charge noise, phonon noise, Johnson noise, etc. These noise sources may couple to the qubit states and cause qubit decoherence. Qubit decoherence can be the result of relaxation or pure dephasing. Relaxation involves energy dissipation and, thus, is mainly due to noise whose spectral density is large at the qubit frequency. Thus, relaxation is negligible when the noise spectral density is weak at low frequencies. Normally, the spectral density of phonon noise is weak at low frequencies and large at high frequencies. Thus, phonon noise is normally the main source of qubit relaxation [80–83], and Johnson noise and charge noise can also contribute substantially to spin relaxation in certain cases [84–86].

In contrast, pure dephasing is mainly due to the randomized phase of a qubit and does not involve energy dissipation. Pure dephasing is mainly due to noise sources whose spectral densities are substantial at low frequencies. In semiconductor devices, nuclear spin noise and charge noise can be strong at low frequencies and, thus, can cause considerable pure dephasing of spin qubits through electric or magnetic coupling. In addition, the nuclear noise of ^{29}Si and ^{30}Si can be largely suppressed or eliminated through the so-called isotopic enrichment of silicon material [30,87–89]. Thus, we will mainly focus on charge-noise-induced pure dephasing and introduce only the main results of nuclear-spin-induced pure dephasing.

In the following, we discuss in more detail the relaxation and dephasing of spin qubits in semiconductor quantum dots and discuss the typical situations of spin qubit systems.

Single-spin decoherence

We first focus on single-spin qubits in quantum dots. The frequency domain of phonon spectral density is proportional to the third power or the fifth power of the frequency, depending on the type of coupling (deformation coupling or piezo-electric coupling) [85,90,91]. Thus, phonon-induced charge relaxation is proportional to the third power or the fifth power of the splitting of a charge qubit. For a single-electron spin qubit,

phonons induce spin relaxation via the SOI. In the case of intrinsic SOI, the Van-Vleck cancellation gives rise to an extra B^2 dependence of spin relaxation, and the phonon-induced spin relaxation shows B^5 or B^7 dependence, with the magnetic field depending on whether deformation (GaAs) or piezoelectric (Si) interaction with the phonon dominates [68,84,90,91]. In contrast, in the case of synthetic SOI induced by an inhomogeneous magnetic field, when the inhomogeneous magnetic field from the micromagnet is saturated, the spin relaxation in silicon is proportional to the B^5 with the magnetic field due to phonon at high magnetic fields [86,92].

Johnson noise and charge noise also introduce spin relaxation at low magnetic fields in certain situations. The noise spectral density of phonons is suppressed substantially at low frequencies due to the strong dependence on the frequency. Then, the Johnson noise or charge noise can be dominant at low frequencies. In this case, spin relaxation due to Johnson noise or charge noise shows weak dependence on the magnetic field.

In the case of intrinsic SOI and large valley splitting, spin relaxation at low magnetic fields shows very weak dependence at low frequencies and saturates due to low-frequency charge noise and spin-valley mixing mechanisms, and is observed in silicon quantum dot devices with micromagnets [93].

Nuclear spin noise and charge noise also induce pure dephasing of the spin qubit. In a GaAs quantum dot, there is strong nuclear spin noise, and the pure dephasing of spin qubits is dominated by nuclear spin noise [94–100]. In a natural Si quantum dot, the nuclear spin noise is relatively weak, and the spin coherence time can be as long as 1 μs [25,101]. In an isotopically enriched ^{28}Si, the concentration of the isotope ^{29}Si (with finite nuclear spin) and ^{30}Si is as low as 800 parts per million (ppm) or even 50 ppm; then, the spin coherence is further improved to nearly 100 μs for spin qubits in gate-defined quantum dots [87,102], although coherence times that are tens of microseconds are more often obtained in experiments [25]. Electron spin coherence time has been extended to nearly 1 ms for an electron in a phosphorus donor in an isotopically enriched ^{28}Si substrate, and nuclear spin coherence time has even been extended to 36 s [30]. The fast operation relative to the long coherence time in ^{28}Si makes the spin qubit an attractive platform for quantum computing, as it enables quantum operation fidelity beyond the threshold for quantum error correction and fault-tolerant quantum computing.

In recent experimental studies, the nuclear spin noise in silicon has been largely suppressed using isotopic enrichment. In addition, spin manipulation speed has been enhanced using EDSR through the synthetic SOI from the micromagnet. The combined long coherence and fast spin manipulation result in the above 99.9% fidelity of spin operation [103]. Note that charge-noise-induced spin decoherence can be relevant with or without the presence of the micromagnet [38,103,104]. It is shown that the broken time-reversal symmetry of the synthetic SOI leads to strong coupling between the electron spin and the driving electric field for the EDSR, and it also leads to strong coupling to the electrical noise, especially the charge noise in the environment [103,104]. The charge noise induces strong pure dephasing and limits the spin coherence time. One possible solution to reduce spin dephasing due to charge noise is to suppress the magnitude of charge noise during quantum dot fabrication, or suppress the undesired magnetic field gradient through the design of the micromagnet [103,104].

Decoherence of exchange-coupled spins

In the case of exchange-coupled spin systems, there is also spin decoherence due to noise affecting the exchange interaction, in addition to the single-electron spin decoherence. We next describe the spin decoherence for exchange-coupled spin qubits (for both the ST_0 qubit and the two-qubit gate problems).

In the case of strong exchange interaction, the two-spin system quantization axis is mostly determined by the exchange interaction J_{ex}. The exchange interaction depends on the detuning between the quantum dots, and thus is influenced by the charge noise in semiconductor devices. Strong low-frequency charge noise can induce fluctuation of the exchange interaction and lead to two-spin dephasing. For both the ST_0 qubit and two-qubit gate of two single-spin qubits, the two-spin dephasing mediated by the exchange interaction can be substantial and dominates the pure dephasing in the system. For two electron spins in a double dot, the system can be operated at the symmetry point, where $\epsilon = 0$ is preferable to minimize charge noise effects as $dJ/d\epsilon = 0$ [105–107].

There are still important differences for spin decoherence of an ST_0 qubit system and a two single-spin qubit system in a DQD. For an ST_0 qubit, the only important dephasing channels are the phase errors on states in the subspace of the spin singlet and spin triplet. When the Zeeman energy difference becomes large compared to the exchange interaction, the projection of the noise of exchange interaction on the quantization axis of the ST_0 qubit is suppressed, and the two-spin dephasing can be suppressed to a certain extent and extend the spin coherence time, as has been demonstrated [108]. However, for a two-qubit gate, the phase factors for all four states in the two-spin Hilbert space are important, and the exchange not only affects the relative phase between the state in the subspace of the spin singlet and spin triplet but also lowers the energy of the singlet and triplet states relative to the spin polarized states by a magnitude of the exchange interaction J. This magnitude is not changed by the Zeeman energy difference between the double dot, and thus, the two-spin decoherence in a two-qubit gate system is still considerable when the Zeeman energy difference is much larger than the exchange interaction [79].

In a two-electron spin system, especially for the ST_0 qubit, when the Zeeman energy is large, the qubit pure dephasing is suppressed. In this case, sensitivity to nuclear noise is increased, since the quantization axis of the ST_0 qubit is now determined by the Zeeman energy difference, and the nuclear spin noise in the system is now coupled to the ST_0 qubit and shifts the energy splitting of the ST_0 qubit. The magnitude of the fluctuation of the energy splitting of the ST_0 qubit due to nuclear spins is on the same order as single-spin pure dephasing due to nuclear spin noise. However, to correct the correlated two-spin errors, a quantum error correction (QEC) protocol with a larger code distance may be required. Then, it is still an important task to investigate ways of suppressing the two-spin errors in the system.

Finally, we would like to emphasize that, in a multiple-qubit system, global operations of the qubits [109,110] and multiqubit gates [111,112] are also desired for efficient operation of quantum gates. In these cases, there could be multiqubit error channels. Since a QEC protocol with a larger code distance may be required to correct multiqubit correlated errors, it is an important future task to study the error channels and the efficient multiqubit gates and find a way to suppress multispin errors.

Gate-Defined Quantum Dots

Confining electrons is essential to encoding quantum information using electron spins. Gate-defined quantum dots, often described as artificial atoms, are nanoscale structures that trap electrons using potential barriers created by electrical gate structures [63]. The concept of using quantum dots for quantum computing, pioneered by Loss and DiVincenzo in 1998 [113], involves using pulsed magnetic fields to manipulate the spin of a single electron within a quantum dot for single-qubit operations and leveraging the exchange coupling between adjacent quantum dots for two-qubit operations, with their compact size and compatibility with conventional semiconductor manufacturing making them highly suitable for scalable quantum computing (see Table 1 for the state-of-the-art performance of gate-defined quantum dots).

Device fabrication

Silicon presents a highly coherent medium for spin qubits and is distinguished by its lack of piezoelectric electron–phonon coupling, and the presence of isotopes devoid of nuclear spin [64,114] enables isotopic purification to eliminate hyperfine interactions. Additionally, silicon's compatibility with established industrial manufacturing technologies enhances its practicality for qubit implementation (see Fig. 2 for the major steps in fabricating gate-defined quantum dot devices).

Substrates

Two main strategies are employed in constructing silicon quantum dots [115]. The first involves devices built on a Si/SiGe heterostructure [101,116–118], and the second adopts a silicon-metal-oxide-semiconductor (Si-MOS) structure.

Table 1. Reported state-of-the-art performance of quantum dot qubits. T_1 is the spin relaxation time. T_2^* refers to the inhomogeneous dephasing time. $F_1(F_2)$ and $T_{1Q}(T_{2Q})$ are the gate fidelity and the operation time of single (two)-qubit manipulation. N_{dot} and N_{qubit} refer to the reported number of quantum dots and the reported number of qubits, respectively. Note that some of the parameters are related to each other; for example, the gate fidelity is the ratio of the gate time to the coherence time.

Property	Parameters	Si-MOS	Si/SiGe
Spin coherence	T_1 (s)	9 [326]	>5 [93]
	T_2^* (μs)	120 [87], 2,000[a] [194]	21 [327]
	T_2^{Hahn} (ms)	1.2 [87]	1.0 [87]
Gate fidelity	F_1 (%)	99.96 [32,43]	99.956 [141]
	F_2 (%)	>99 [26,38,39]	>99 [33, 35 36]
Number of qubits	N_{dot}	4 [328]	9 [128]
	N_{qubit}	4 [328]	6 [43]

[a]A coherence time of 2 ms was measured using the sinusoidally modulated, always rotating, and tailored (SMART) qubit protocol.

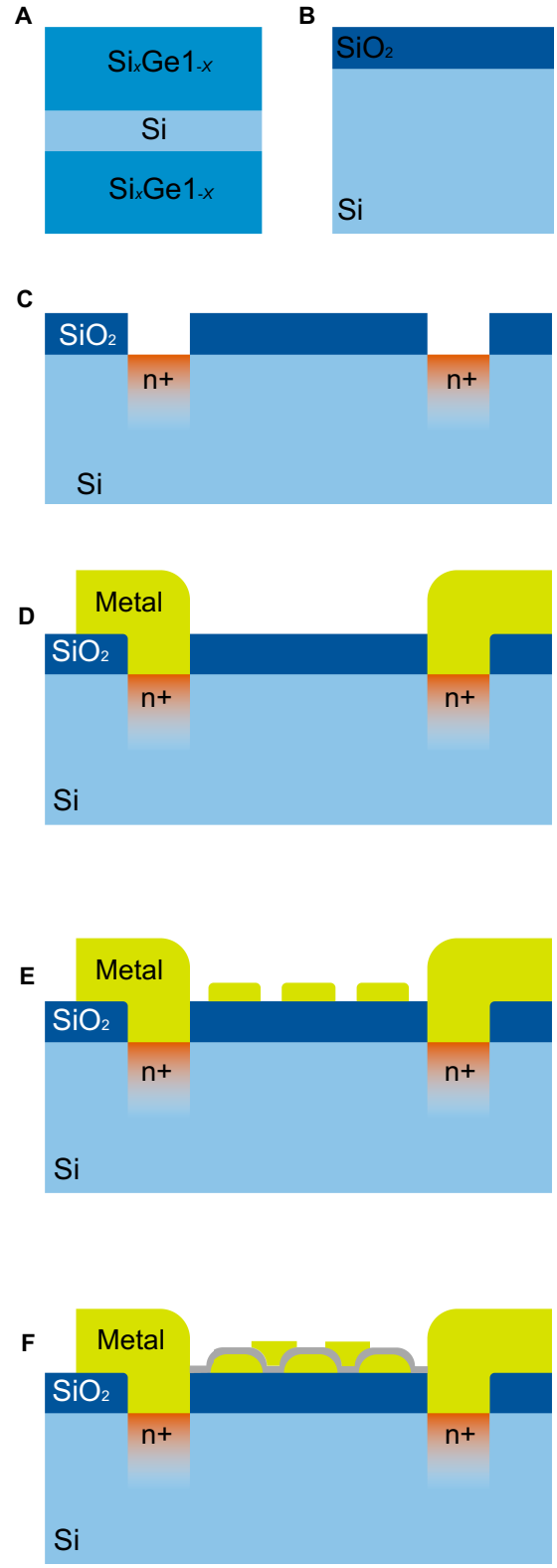

Fig. 2. Fabrication sequence for Si gate-defined quantum dot devices. (A) Cross-sectional representation of the SiGe/Si/SiGe quantum well heterostructure. (B) Si-MOS structure. (C) Ohmic contacts are formed by phosphorus diffusion: a top layer of high-quality oxide is thermally grown, followed by the definition of an aperture for ion implantation. Phosphorus ions are implanted and RTA is conducted to repair the formed defect and damages. (D) The metal ohmic contact bonding pads are made. (E) Deposition of first layer gates. (F) Oxidation is applied to form an insulating layer between stacked gates, followed by stacking layers of gates through repeated cycles.

The Si/SiGe method uses a $Si_{1-x}Ge_x$ barrier to separate the Si quantum well, which is grown on a strain-relaxed SiGe buffer, from the interface. This material's mobility can reach approximately 3.14×10^5 cm^2/Vs, and the percolation density can achieve roughly 6.9×10^{10} cm^{-2} [119]. However, the low valley splitting, due to the $Si_{1-x}Ge_x$ barrier's weak confinement, presents challenges. This issue is compounded by the variability in valley splitting across different devices [120], which could lead to quick spin relaxation [82,93] and state leakage. Strategies to enhance the valley splitting [121] in silicon quantum dots include creating sharp interfaces to increase the quantum well confinement potential, using both uniform and nonuniform distributions of germanium within the quantum well, and optimizing the interface width along with alloy disorder management.

The Si-MOS approach confines a 2DEG at the silicon–silicon oxide interface, where strong confinement leads to considerable, tunable valley splitting [82]. As the electrons are confined at the interface, the electrons maximally experience the disorders at the amorphous oxide interface. Consequently, the formation of the oxide layer is crucial for Si-MOS quantum dot fabrication. In the university fabrication process, the MOS device fabrication is centered around the formation of oxide layers. The process begins with cleaning the wafer using a variety of solutions, including piranha etch, deionized water, RCA-2 solution, and HF, to remove the natural oxide layer. The wafer is then subjected to oxidation at 900 °C using dry O_2, wet O_2, and N_2. High-quality Si-MOS fabrication processes have enabled mobility to reach approximately 1.75×10^4 cm^2/Vs [122] and the percolation density to achieve roughly 10^{11} cm^{-2} [123].

Due to its compatibility with industrial-level fabrication, the silicon qubit effort has inspired leading institutions and companies to adopt advanced industrial fabrication nodes. Technologies such as fully depleted silicon-on-insulator (FDSOI) enable precise control over the conduction channel and vertical confinement through independent top and bottom gates [124], and fin field-effect transistor (FinFET)-like devices have been developed to reduce the qubit footprint [125].

Ohmic contacts

Ohmic contacts are typically formed by phosphorus doping. A doping window is opened by etching with O_2 plasma and buffered HF acid. The sample then undergoes phosphorus doping in a furnace. Si-MOS additionally requires re-oxidation, and gate oxide layers are formed at 800 °C using gases such as dry O_2, dichloroethylene + O_2, and N_2. The microfabrication step concludes with forming gas annealing at 400 °C for at least 15 min [126].

The ohmic contacts can also be replaced by a metallic, nonmagnetic NiSi, which forms a Schottky barrier between the contact and the substrate, allowing for ambipolar operation [125]. The NiSi electrodes are formed using electron beam lithography (EBL), followed by nickel evaporation and lift-off processes, with low-temperature silicidation annealing conducted at 475 °C for 30 min in an argon ambient. Lateral nickel diffusion beneath the gates tunes the Schottky barrier width. Unreacted nickel is selectively removed. Finally, the devices are shielded by a SiO_2 passivation layer and connected through tungsten interconnects.

Gate deposition and etching

The large effective mass ($\approx 0.19 m_e$) of electrons in silicon constrains the feature size of the quantum dot gate layout, which requires high gate density and small gate size to control the quantum dot and, thus, the qubit. Overlapped gate design [127] allows a higher gate density and has been adapted to Si/SiGe systems [128]. In university cleanroom facilities, metalization involves depositing aluminum or palladium gates via electron-beam evaporation and subsequent metal lift-off. Chips are cleaned with NMP and O_2 plasma etch, followed by patterning with alignment markers, e-beam lithography, and evaporation of Ti/Pt or Ti/Al layers. Further gate patterning uses resist spinning, e-beam lithography, and Al or Pd layer evaporation. Concluding steps include metal lift-off and Al oxidation. This gate patterning process is repeated for a multilayer gate stack.

Electrical isolation between different layers is achieved either through aluminum oxidation or by depositing a few nanometers of a dielectric layer using atomic layer deposition (ALD), typically aluminum oxide (Al_2O_x), hafnium oxide (HfO_2), or silicon oxide (Si_2O_x). For MOS devices, it has been observed that ALD can increase charge noise by an order of magnitude [110,129]. However, this issue is less severe in quantum wells because the 2DEG is situated further from the interface. The fabrication process is completed with the addition of either on-chip micromagnets to create magnetic field gradients or a strip line antenna to produce an oscillating magnetic field for controlling the qubits.

To improve gate density with high precision, a self-alignment technique for enhancing gate pitch precision and increasing gate density for improved control has been integrated with the FinFET fabrication process [130]. This method starts with the formation of the initial gate layer using TiN. Electron beam lithography with hydrogen silsesquioxane resist is performed to pattern the gate layout. The subsequent ALD of the gate stack ensures uniform coverage across the device, filling almost all interstitial spaces between gates. Selective removal of TiN from uncoated flat areas through timed dry etching leaves TiN residues at topographical features. The process concludes with the application of a protective resist mask and an isotropic wet etch, ensuring the removal of any unintended TiN residues.

Another approach involves using the single-layer etch-defined gate electrodes (SLEDGE) technique [57]. This method marks a shift from multilayered structures to a single-layer gate design, which considerably reduces electric field screening, lowers the voltage requirements for qubit operation, and minimizes charge noise due to the absence of an additional dielectric layer below the metals gates. The metal gates likely screen any charge noise from oxides introduced during the back-end-of-line process. The gate metal, TiN, is selected for its low defect density and favorable etch selectivity. In this process, dot-shaped gates are used instead of traditional line shapes, enabling more versatile gate arrangements. The fabrication process includes blanket deposition of the gate dielectric and metal, followed by a coarse etch and e-beam lithography to pattern the gates, with connections made to larger routing interfaces.

The coefficient of thermal expansion mismatch at the interface needs careful consideration, as it can cause strain during cooling to cryogenic temperature. Incorporating poly-silicon gates for the all-silicon process is expected to minimize strain gradients from electrode thermal mismatch [131]. Therefore, the strain-induced quantum dot can be eliminated by replacing the metal gates with poly-silicon gates [132].

Leading institutions and companies have adopted distinct silicon qubit fabrication technologies. IMEC has implemented

a combination of a 300-mm process with a triple-layer EBL process [50,133]. In collaborative efforts, IBM and the University of Basel have developed FinFET-like devices using self-aligned processes to achieve finer control with pitches as small as 60 nm [122,130] (15 nm length and 45 nm spacing). CEA-Leti has innovated with immersion deep ultraviolet lithography for plunger gate definition, while integrating self-aligned barrier gates at pitches of 80 nm, enhancing density [134,135]. Intel has developed FinFET-like devices on isotopically purified 300-mm silicon substrates with advanced lithography, achieving a plunger-barrier pitch of 50 nm, and offers another version for qubit confinement with the Si/SiGe configuration showing high single-qubit gate fidelity [136,137]. Each approach, whether employing traditional EBL, advanced FinFET structures, or the latest EUV techniques, reflects a strategic emphasis on controlling critical dimensions and intergate alignments to ensure coherent and reproducible qubit performance.

Qubit initialization and readout

Direct reading of a spin is challenging because the magnetic nature of spins results in weak interactions with most measurement probes. This necessitates either the use of large-scale setups or the acceptance of slower readout speeds compared to the brief lifetime of the spin's quantum information. Thus, initialization and readout are typically performed in two different styles of spin-to-charge conversion: Elzerman style single-shot readout [138] and singlet–triplet readout [139].

Spin-selective tunneling

Single-shot readout of a single spin utilizes a spin-to-charge conversion method where the electron tunneling to the reservoir depends on the spin states [138]. This readout process is performed by aligning the Fermi level of the reservoir between the spin-up and spin-down energy levels of the quantum dot. This adjustment only allows a spin-up electron to tunnel out to the reservoir, generating a detectable signal in the nearby quantum dot that serves as a sensor, while a spin-down electron remains in the quantum dot. If the electron initially has a spin-down state, it stays within the quantum dot. The final state is initialized to $|\downarrow\rangle$ after completing the load–read cycle.

The tunneling rate must balance the trade-off between detection bandwidth and the relaxation time of the excited state [140]. High-fidelity readout exceeding 99.5% using the Elzerman technique (the spin-selective tunneling readout method) has recently been achieved in Si/SiGe quantum dots, with an integration time of less than 1 ms [141,142].

Pauli spin blockade

Electrons in a reservoir follow a Fermi-Dirac distribution, and their energy levels are broadened at finite temperatures, which can introduce errors in readout mechanisms that rely on reservoirs due to energy level smearing. Thus, readout fidelity is constrained by the electron temperature. Moreover, as a quantum dot array expands, tunneling to a distant reservoir becomes challenging, necessitating complex spin shuttling [143,144] and a series of SWAP operations. Consequently, achieving high-fidelity readout without a reservoir becomes a necessity for scalable quantum computing.

Singlet–triplet readout, which utilizes Pauli spin blockade between two quantum dots, eliminates the need for a reservoir in the readout process. This method focuses on singlets in the (1,1), (0,2), and (2,0) configurations and triplets in the (1,1) charge state, with doubly occupied triplets being energetically unfavorable due to strong exchange coupling and charging energy. The readout cycle includes initialization, control, and readout phases, starting with spins in a $|(0,2)S\rangle$ state and then separating them for control. The final state is determined by adiabatically returning the singlet states to the (0,2) region, allowing only singlet states to tunnel back and produce a charge signal difference between the (1,1) and (0,2) charge states. This method, unlike the Elzerman technique, does not retain all two-qubit information, but it provides sufficient information to determine the spins within a subsystem, where one of the spins can act as an ancilla spin to indicate the state of the target spin. However, this method allows for decoupling the system from the electron reservoir, enabling operation at effectively higher temperatures [38,45,46].

The dipole moments of double dots can be detected as changes in capacitance using RF resonator circuits, leading to extensive efforts to enhance both the speed and fidelity of readout [145–148]. These efforts have successfully achieved a readout fidelity of 99.975% within an integration time of 980 ns [149].

When the dephasing mechanism between singlet and T_0 states during the (1,1) to (0,2) transition dominates, the Pauli spin blockade readout extends to parity readout [150], allowing two of the four states to be unblocked. This method involves initializing in a mixed state of S_0 and T_0, presenting a classical 50–50 chance of being $|\downarrow\uparrow\rangle$ or $|\downarrow\uparrow\rangle$. A pure two-qubit state can be initialized with active reset [43] or algorithmic initialization [38]. If a reservoir is nearby, fast initialization is possible with the reservoir [148]. An all-electrical quantum nondemolition (QND) measurement technique has been developed for single electron spins in quantum dots. This method transfers the information of the target qubit to the ancillary qubit and performs a single-shot readout of the ancillary qubit, achieving noninvasive projective measurement at a speed considerably faster than the spin's relaxation time [151]. The QND nature of this protocol enhances measurement fidelity through iterative repetition, showing notable improvements over 100 iterations. When applied to silicon spin qubits, this technique can considerably boost qubit readout fidelity by mapping a logical qubit's state to an ancillary qubit and then measuring the ancilla destructively, with an improvement on the readout fidelity from 75% to 94.5% after multiple repetitions [152]. In contrast to traditional thresholding, this method employs soft decoding, a signal processing technique that uses analog information for more accurate state estimation, especially in scenarios with low signal-to-noise ratios.

Qubit operations

Single-qubit gates

Spin qubits can be manipulated through various techniques. These include applying an AC magnetic field to utilize their natural magnetic characteristics, leveraging SOI to link spin with charge, and associating spin with electric fields via exchange coupling. Additionally, qubits can be encoded by using the charge alone or by harnessing the interactions among multiple electron spins, specifically exchange coupling, to tie the spin degree of freedom to an electric field. Research has been dedicated to developing qubits from single electron spins [87,153,154] and pairs of electron spins (e.g., singlet–triplet qubits [155–158] and two-electron flip-flop qubits), charge states [159–162], blends of spin and charge states [163–166], configurations involving three electrons (such as spin-charge

hybrids [164], resonant exchange [167], and exchange-only qubits [168,169]), and 4-electron quadrupole exchange [170]. These initiatives aim to exploit the charge degree of freedom for improved qubit control, seeking to design energy bands that make qubits more resistant to charge or magnetic disturbances, thereby enhancing their coherence. In this review, we focus on the simplest type of qubit—the qubit based on a single spin, also called the LD qubit.

A coherence time of 120 μs and a control fidelity of 99.3% have been achieved in ESR drive systems within a purified 800 ppm Si/SiO_2 device [87]. With the implementation of pulse shaping for optimized control, a Clifford gate fidelity of 99.96% was realized [32,43]. Selecting specific spins in an ESR system presents a difficult challenge. To address this, methods such as leveraging intrinsic SOI for *g*-factor control and applying on-site *g*-factor tuning alongside on-demand electrical control have been demonstrated [171], offering pathways to scale up qubits with ESR drive [172]. Another concern with ESR is power dissipation, as device heating can limit the achievable Rabi frequency. New resonator designs and strategies are proposed for global microwave control to minimize energy loss, while localized control is achieved by using local top gates to tune individual qubits in and out of resonance with the global microwave field [109].

Qubits can also be manipulated by electric fields in the presence of a magnetic field gradient created by an on-chip micromagnet, or through SOI. This mechanism shifts the electron's orbital wave function, causing the electron to perceive an oscillating magnetic field. Artificial SOI facilitates the direct coupling of electric fields to spin, enabling faster spin rotations [118]. Although this driving mechanism differs from ESR, the fundamental physics of spin manipulation remains similar, as the effective oscillating magnetic field, perpendicular to the external DC field that splits the spin states, arises from the magnetic field gradient. This approach also improves selectivity, mitigating the challenges associated with ESR. Qubits created with the Si/SiGe heterostructure have reached a fidelity for single-qubit gates exceeding 99.9% [103], surpassing the threshold for fault tolerance [173]. Demonstrations include achieving a single-qubit gate speed up to 30 MHz with fidelity greater than 99.9% in devices on Si/SiGe with a Co micromagnet [103,141]. So far, micromagnets have been incorporated into devices with few quantum dots, but adapting them to large-scale arrays will require further design effort.

Spatially correlated noise and cross-talk

Spatial noise correlations

Small quantum dots may encounter defects comparable to their scale, or even defects that extend across arrays of quantum dots. Various types of noise, such as phonons with specific characteristic scales, highly localized nuclear spin noise, and $1/f$ charge noise, can influence quantum systems differently. The latter, for instance, weakens with distance and can be mitigated by growing a thicker dielectric layer to move the noise source further from the qubit. As the number of noise sources decreases, the behavior of individual impurities becomes more pronouncedly quantum mechanical [174].

There have been a few demonstrations on utilizing noise correlations to identify noise sources in Si-based qubit systems. The resonance frequency of a two-qubit system was tracked in an 800 ppm ^{28}Si-MOS device, identifying a local uncorrelated noise source, probably residual nuclear spins coupling to quantum dots [175]. This was further supported by an NMR spectrum, which exemplifies the identification of the noise source through correlation [176]. Another more careful analysis using a ^{28}Si/SiGe device with a micromagnet observed correlated noise through Ramsey interference, which identifies the correlation strengths up to 0.7 at 1 Hz, and suggests an electrical noise origin [103]. A more efficient approach to quickly extract noise correlations is to monitor the entanglement coherence time in subspaces spanned by different Bell states [177]. However, as concluded in Ref. [177], this method is expected to be more powerful in purified silicon devices, because it does not efficiently distinguish nuclear noise from charge noise, which is more relevant and generally regarded as correlated. Modeling the noise as independent two-level charge defects within the oxide layer accurately reflects these observations [178]. The model also predicts a d^{-2} decay of noise cross-correlations with interqubit separation and could be reduced to d^{-5} with gate metal screening. Moreover, as the impact of electrical noise on spin qubits depends on the qubit implementation, the noise spatial correlation can also be exploited to reduce the influence of charge noise [71,179].

Cross-talk errors in simultaneous single-qubit operations

Simultaneous single-qubit gate fidelities were first reported using randomized benchmarking [180], in which the fidelity decreases more markedly on one qubit than on the other, suggesting that the cross-talk effect can be asymmetric. Later, a simultaneous single-qubit fidelity of 99.1% was reported [141], where the cross-talk error was suggested to be lower than the idling error [141]. However, the result from characterizing the single-qubit fidelity within a single-qubit subspace to a two-qubit subspace reveals a decrease in fidelity from 99.72% to 99.16%, which is attributed to both cross-talk induced by the qubit being driven and dephasing of the idling qubit [36]. The cross-talk error can be mitigated by employing dynamic pulse shaping techniques, such as the DRAG protocol, to minimize cross-talk and phase errors [181]. By adjusting the amplitude and phase of control signals, the optimization ensures that the quantum state evolves as intended, minimizing deviations caused by these coherent error sources. To mitigate decoherence, it is recommended that when one qubit is active, the other should not remain idle; instead, both qubits should be operated simultaneously whenever possible. This is because the idle gate usually has lower fidelity [32,33], while noise can be echoed out to some extent during single-qubit rotations.

Another factor that could contribute to cross-talk in large-scale systems is heating-induced phase shifts [182], particularly pernicious transient qubit frequency shifts associated with microwave-driven qubit operations. Several strategies have been explored to minimize this effect, including the use of off-resonant microwave bursts to stabilize the device [183], implementing wait times prior to measurements, and applying qubit-specific calibrations. However, these strategies pose challenges for device scalability. Operating the qubit device at 200 mK considerably mitigates adverse heating effects without compromising qubit coherence or the benchmarks for single-qubit fidelity [184]. The most plausible explanation for these observations is a temperature-dependent electric field that causes Stark shifts in the Larmor frequencies. Nevertheless, direct evidence of such an electric field is still lacking.

Two-qubit gates and entanglement

The implementation of two-qubit gates for LD qubits in a DQD relies on controlling the exchange interaction, given by $J = \frac{4t^2U}{U^2-\epsilon^2}$, where t is the interdot tunnel coupling, U is the on-site charging energy of each dot, and ϵ is the detuning of chemical potentials. In early approaches, activating the exchange interaction involves pulsing the plunger gates to detune the chemical potentials, thereby increasing ϵ. Electrical detuning ϵ of the quantum dots via their top-gate voltages modifies single-qubit resonance frequencies via the Stark shift [171] and the two-qubit exchange coupling. This method translates to SWAP-like operations under qubits with the same Zeeman energy.

However, due to the presence of spin-orbit effects and potential Zeeman energy difference ΔE_Z, small exchange coupling J can lead to CZ-like operations when $J/\Delta E_Z \ll 1$ [185]. These dynamics are commonly implemented in spin systems, leading to gates such as the $\sqrt{\text{SWAP}}$ gate [155,186], the CPHASE gate [33,35,36,102,180,183], and the controlled-rotation (CROT) gate [102,187–189]. The $\sqrt{\text{SWAP}}$ and CPHASE gates, in particular, require fast temporal control of the exchange interaction J. The strength of Zeeman energy difference ΔE_Z is typically controlled via the intrinsic SOI [190] in a Si-MOS system between 1 and 100 MHz [171], but it can also be controlled artificially by utilizing a micromagnet, which could result in a bigger ΔE_Z difference around 1 GHz [180,183].

Although one of the two-qubit gates is sufficient to span the full Hilbert space, the possibility of being able to implement different types of two-qubit gates could simplify the quantum algorithm. Here, we discuss the operations of different two-qubit gates performed in silicon qubits.

First, we discuss SWAP gates. When $\Delta E_Z \ll J$, the exchange interaction dominates the Hamiltonian. At a given J, the dynamics are purely driven by the exchange Hamiltonian, and the exchange coupling constantly swaps energy between the two spins, thus swapping the states $|\downarrow\uparrow\rangle$ and $|\downarrow\uparrow\rangle$ at a rate of J. This regime typically can only be accessed away from the symmetric operation point, where charge noise introduces strong dephasing. The SWAP operation is generally the fastest among the two-qubit gates, since it is usually operated at a large J to suppress the ΔE_Z contribution. However, the SWAP gate also suffers the most from charge noise because the large J regime is also the regime where $\frac{dJ}{d\epsilon}$ is the largest. By controlling the duration of the exchange interaction, the entangling $\sqrt{\text{SWAP}}$ gate can be achieved (see the description of SWAP gates in the "Two-qubit operations" subsection under the "Basic Theory" section). Here, the nonnegligible Zeeman energy difference ΔE_Z becomes a challenge for implementation of the perfect SWAP gate. Instead, the spin state rotates along an axis determined by ΔE_Z and J. Composite pulses or dynamical pulse shaping can account for the errors caused by the tilted axis [189].

Second, we review CPHASE gates. When $\Delta E_Z \gg J$, in the rotating frame of the $|\downarrow\uparrow\rangle, |\downarrow\uparrow\rangle$ space, the off-diagonal elements in the Hamiltonian, $J(t)/2$, become fast-oscillating terms and can be neglected. The diagonal elements detune the energies of $|\downarrow\uparrow\rangle$ and $|\downarrow\uparrow\rangle$ states by $-J/2$, introducing an extra phase to the $|\downarrow\uparrow\rangle$ and $|\downarrow\uparrow\rangle$ [76] states. This condition $\Delta E_Z \gg J$ is conveniently met in devices with micromagnets. In this regime, a CPHASE gate is realized. Notably, mitigated CZ gates commute with Z gates, allowing for using a decoupling sequence, known as the decoupled CZ gate (see the description of CPhase gates in the "Two-qubit operations" subsection under the "Basic Theory" section). When the condition $\Delta E_Z/J$ is not fully met, unwanted SWAP operations may occur. To minimize residual SWAP actions, an adiabatic pulse can be used instead of instantaneously activating the exchange coupling. However, this approach of gradually changing the gate voltage can slow down the operation time of two-qubit gates. Alternatively, implementing a geometric CPHASE gate allows for synchronizing undesired exchange oscillations with CPHASE oscillations, offering another strategy to address this challenge [191]. Recently, a CZ gate fidelity of 99.81%, determined by randomized benchmarking, was achieved with charge noise identified as a primary limiting factor [33]. Additionally, a fidelity of 99.5% was reported using gate set tomography (GST) [36] (see Fig. 3A and B).

CNOT gates are the most commonly used two-qubit gate in quantum algorithms, especially in quantum error correction circuits. They can be compiled using $\sqrt{\text{SWAP}}$ gates or a CPHASE gate together with additional single-qubit gates, and can also be directly implemented with the exchange interaction. When the two-qubit system is in the (1,1) charge region and far detuned from a doubly occupied charge state (2,0) or (0,2) ($\Delta E_Z \gg J$), similar to the case of the CPHASE gates, applying microwave pulses at one of four selected frequencies leads to a conditional rotation (see the description of CNOT gates in the "Two-qubit operations" subsection under the "Basic Theory" section). However, driving at a specific conditional frequency causes finite rotation and phase shift for states that are associated to nearby qubit frequencies due to the cross-talk between qubit states. To mitigate cross-talk errors, the lengths and amplitudes of all conditional $\pi/2$-pulses can be adjusted so that the off-resonant drive also completes a full cycle. Notably, selecting the shortest possible conditional $\pi/2$-pulse duration for the available microwave power helps minimize dephasing. Phase errors from off-resonance driving can be corrected with a virtual-Z gate [192,193]. A resonant CNOT gate demonstrating 99.5% fidelity was achieved using an "always-on" exchange approach [35] (see Fig. 3C and D). However, this method lacks scalability. Scalability for a resonantly driven CNOT gate, akin to the CPHASE approach, can be achieved by modulating J through corresponding barrier gates. This necessitates pulsed control of the exchange coupling and additional idle periods to mitigate undesired phase accumulation.

To address challenges like microwave cross-talk and CZ mixing with SWAP terms, qubits can be operated with common Larmor frequencies and Rabi strengths, making them degenerate and indistinguishable under microwave control. They can be selectively addressed using Stark shift control or local magnetic field gradients. This global control scheme is essential in scalable quantum computing architectures for several reasons: it simplifies the management of numerous qubits by using shared control resources, mitigates qubit property variations and environmental noise, allows for consistent qubit performance across a large array, and enhances resilience to fluctuations. The degenerated qubits also have the advantage of using only a single microwave frequency to globally control all qubits; thus, they can avoid cross-talk and frequency crowding in a scalable system [194].

Both the primary advantage and the key challenge for spin qubits stem from the same source—their nanometer-scale size

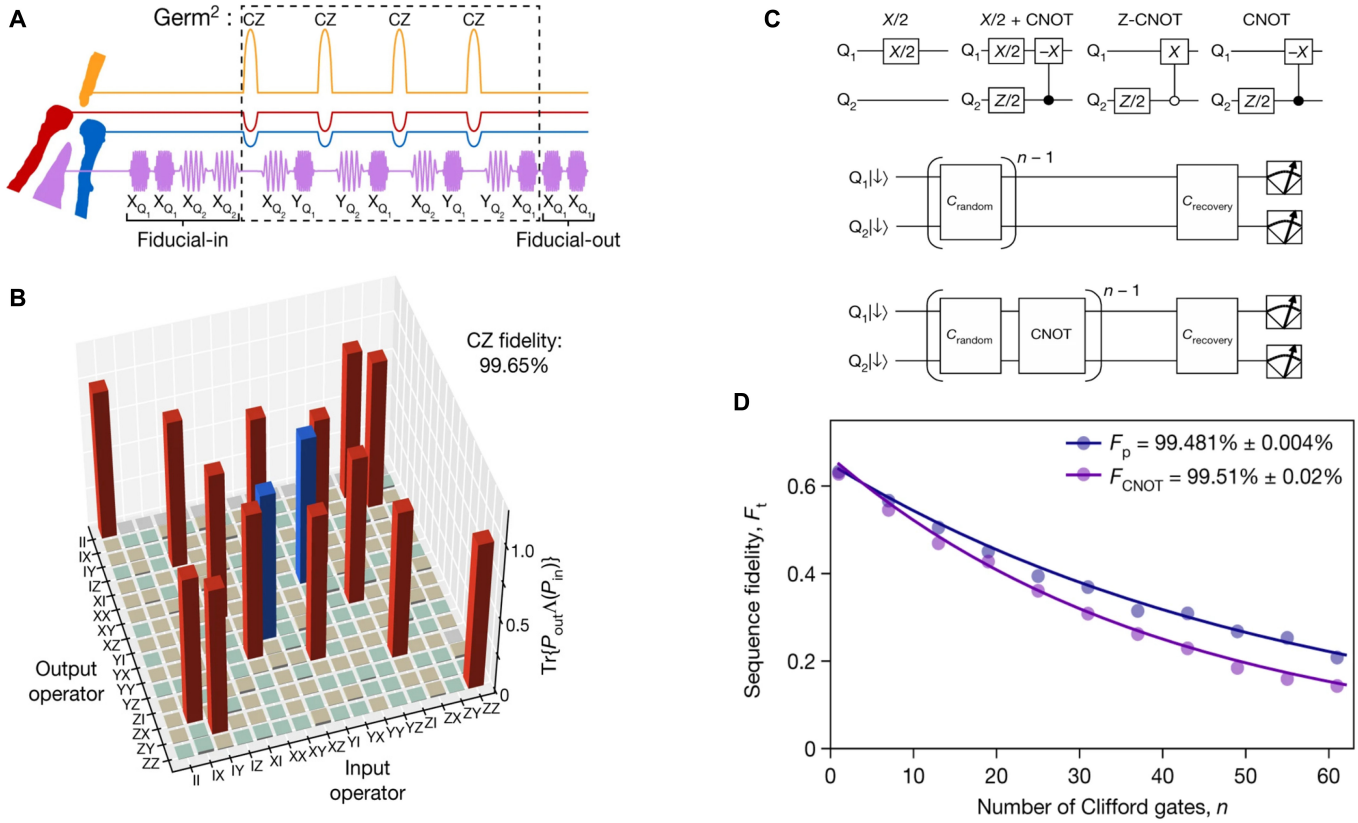

Fig. 3. Two-qubit gate characterization in gate-defined quantum dots. High-fidelity two-qubit gates have been demonstrated in gate-defined quantum dots with two methods, gate-set tomography (GST) [36,39] and Clifford-based interleaved randomized benchmarking [33,35,38]. GST can be utilized to extract the gate fidelity, identify specific errors, and aid in gate optimization, as shown in (A) and (B) [36]. The interleaved randomized benchmarking method evaluates the average fidelity without accounting for SPAM errors, as shown in (C) and (D) [35]. Moreover, Bell state fidelities have been employed to assess the entanglement capabilities of the two-qubit gate in early attempts [183,187]. (A) and (B) are adapted from Ref. [36], Springer Nature, under a CC BY license. (C) and (D) are adapted from Ref. [35], with permission, Springer Nature.

and their potential compatibility with the semiconductor industry. While the fabrication and operation of spin qubits share similarities with conventional transistor technologies, they are different in reality. Optimizing materials in the quantum regime involves different requirements compared to optimizing materials for classical devices. This distinction creates a unique dynamic: universities tend to focus on flexibility, which allows for fast turnaround and the ability to make different types of devices, but this comes with low yield; meanwhile, the industry focuses heavily on reproducibility and high-yield processes, but adapting these processes for quantum architectures takes a lot of time and effort. Communication and understanding between these two ends of the spectrum also takes time, as both sides need to understand each other's mindsets. Recent successful interactions between industry and research groups (see the "Gate deposition and etching" subsection above, under the "Device fabrication" section) offer hope, showing that collaboration can drive progress. If these challenges are addressed, we may see major strides in building large-scale quantum processors in the near future.

Large-scale qubit array

The development of scaling silicon qubits presents multiple challenges and open questions, particularly regarding integration strategies for qubit arrays (Fig. 4). For large systems with very small quantum dots, highly dense gates are necessary, posing complex engineering problems that may involve on-chip electronics and the deployment of cryo-CMOS technology (Fig. 4C). Fortunately, an important advantage of silicon qubits is their ability to integrate with classical electronics [195]. This integration is crucial for minimizing thermal and electronic noise, optimizing space, and improving control and readout speed and fidelity. Proposals have suggested integrating classical electronics directly into sparse quantum arrays [196] to reduce the number of external signal connections. Qubits can be arranged in a two-dimensional (2D) array with a 12-μm pitch to accommodate integrated circuits that correct potential inhomogeneities and allow global sharing of control signals.

CMOS-like technology can also be employed directly above dense qubit layers [197]. This design (Fig. 4A) incorporates a structure based on dynamic random access memory (DRAM) for addressing individual qubits and their coupling, where floating gates can hold an electrical charge for extended periods, thus allowing for persistent control settings that do not require constant and frequent refreshment. This approach is beneficial for compact circuit design, allowing for dense packing of qubits while still maintaining control over each individual qubit.

Different wiring layouts have also been proposed to reduce gate density. Crossbar network design using shared control lines in a grid layout can simplify the control and addressing of qubits without the need for dedicated wires for each qubit [198]. This design (Fig. 4B) features a simple and elegant

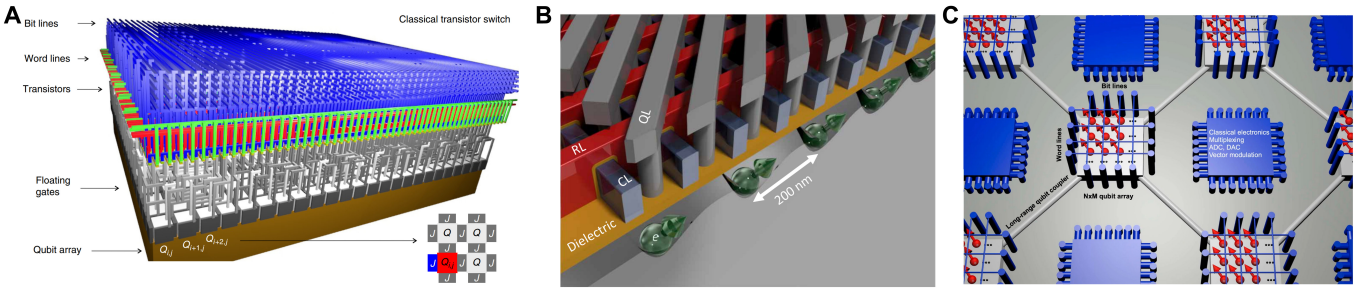

Fig. 4. Large-scale quantum dot array architecture. (A) This integrated MOS chip is fabricated on a silicon-on-insulator wafer. The design features a two-dimensional qubit array in the bottom layer, while the transistor layer is positioned on top to control the qubits. These layers are interconnected through the oxide regions using metal vias, allowing efficient control between the transistors and the qubit array [197], Springer Nature, image adapted under a CC BY license. (B) Three-dimensional model of the crossbar design structure, with dielectrics between the various gate layers omitted for clarity [198], image adapted with permission, AAAS. Blue, red, and gray gate lines connect the qubit grid to outside electronics for control and readout. A combination of these lines enables qubit selectivity. The electrons can be shuttled around by the gate voltages, providing a means to couple nearest neighbors for two-qubit logic gates and readout and to couple to remote qubits for long-range entanglement. (C) A sparse qubit array with local electronics can be advantageous, as long-distance qubit coupling frees up space for local electronics to manage a smaller, denser qubit array. In the schematic, these electronics are integrated within the qubit plane. A crucial aspect of this design is determining the optimal size of the qubit array, represented as $N \times M$, and ensuring the functionality of the local electronics. Ideally, these electronics should include ADC and DAC converters to facilitate precise control and measurement [195], Springer Nature, image adapted under a CC BY license.

structure that avoids extremely small feature sizes, but rather relies on a high level of uniformity to reduce the complexity of interconnects. By employing shared control lines in the crossbar layout, the design minimizes the physical footprint of wiring and maximizes signal routing efficiency, where the number of addressing lines increases proportionally to $\sqrt{N}$, with N being the number of qubits.

Discussions on the topic of large-scale design have considered several different array configurations—linear, bi-linear, and 2D—each of which has its own set of trade-offs regarding interqubit interactions and error correction strategies. Experiments have demonstrated several different configurations of the array. A device featuring a 9-quantum-dot linear array in silicon was fabricated in 2016 [128]. Additionally, a 2×2 quantum-dot array was developed in a ^{28}Si heterostructure, achieving a (1, 1, 1, 1) charge state across four quantum dots [199]. Moreover, it has been shown that qubits in a linear array of six quantum dots maintain high control fidelity [43].

Two types of uniformity are of high importance in the selection of materials for the design of large-scale arrays. The first is electronic uniformity, typically characterized by mobility and percolation density. This is important because it helps ensure the precise formation of quantum dots and the fine control of charge states as well as a predictable electronic excited state such as valley splitting. Quantum dots made with new materials such as germanium provide a platform with low effective mass (approximately $0.05m_e$), high mobility, and strong SOI [60,115]. Recent progress has seen a 4-qubit system with controllable coupling in a 2×2 array [44], and a 16-quantum dot device [200]. Even more recently, a 10-qubit array has been demonstrated [201]. Strong SOI makes it possible to achieve values of the Rabi frequency that exceed 100 MHz [202]. However, faster spin manipulation comes at the cost of unwanted errors. The optimal fidelity (99.992%) was realized at a relatively small Rabi frequency [34]. These advancements demonstrate hole-spin qubits as a promising platform for quantum computing, with important improvements in both control fidelity and coherence times. Moreover, rather elaborate quantum algorithms have been implemented using the set of gates described above. For instance, four qubits were entangled into a Greenberger–Horne–Zeilinger (GHZ) state and subsequently brought back to a product state [44]. Error correction codes have been explored [203].

The second type of uniformity—spin uniformity—is often affected by residual nuclear spins and SOI from interface disorder, which can reduce both the coherence time and the uniformity of spin qubit properties (e.g., the uniformity of the g-factor). Addressing this issue requires a twofold approach. First, continuously improving the material, enhancing interface quality, and optimizing the material stack are crucial. Material improvement is discussed above, in the "Substrates" subsection under the "Device fabrication" subsection. Second, developing a control scheme that can accommodate qubit variability is necessary. The proposal by Kane [204] uses a global microwave field that is typically off-resonance with the qubits, with local controls tuning individual qubits into resonance via gate operations. Various global qubit control strategies suitable for large-scale operation and fabrication have been explored in recent studies [109]. Alternatively, driving all qubits on-resonance by default operates them as dressed qubits, where the global dressing field helps decouple the qubits from environmental noise, extending coherence times but can lead to cross-talk due to variations in resonance frequencies. To improve robustness against frequency deviations and driving field fluctuations, protocols such as SMART [194,205] have been suggested for qubit operations.

Electron Spins in Dopants

Dopants are intentionally introduced atoms that alter the host material's physical properties, and they are categorized as p-type and n-type dopants in semiconductor physics. Dopants also facilitate quantum computing in silicon because they have distinct energy levels in the band gap that are suitable for quantum information applications. The commonly utilized dopants include phosphorus (P), arsenic (As), antimony (Sb), bismuth (Bi), boron (B), aluminum (Al), and gallium (Ga). Among the n-type dopants, phosphorus is extensively researched and holds promise for qubit encoding. The previous decade has witnessed major advancements in this domain. Here, we focus on phosphorus below, and the other dopants are also briefly mentioned. As

nuclear spin qubits are highly related to the electron spin via the hyperfine interaction in the dopants [61,62], here we discuss nuclear spin qubits when necessary.

Device fabrication

In Kane's seminal proposal in 1998 [204], the nuclear spins of phosphorus donors were used to encode qubits to explore the potential of Si:P as a platform for quantum computation. Following this blueprint, two primary experimental routes to fabricate dopant-based quantum computation devices were developed: the ion-implantation method and the scanning tunneling microscope (STM) lithography method (see Fig. 5). The traditional diffusion method can introduce dopants in the transport channel of field-effect transistors (FETs) [206], but the considerable uncertainty in doping position resulting from the post-thermal process constrains its application in scalable quantum computing devices. Similar techniques such as δ doping and bulk doping during the epitaxy process lack controllability of in-plane directions, which limits their application for qubit construction. Thus, in this review, we focus on the ion implantation and STM lithography fabrication methods.

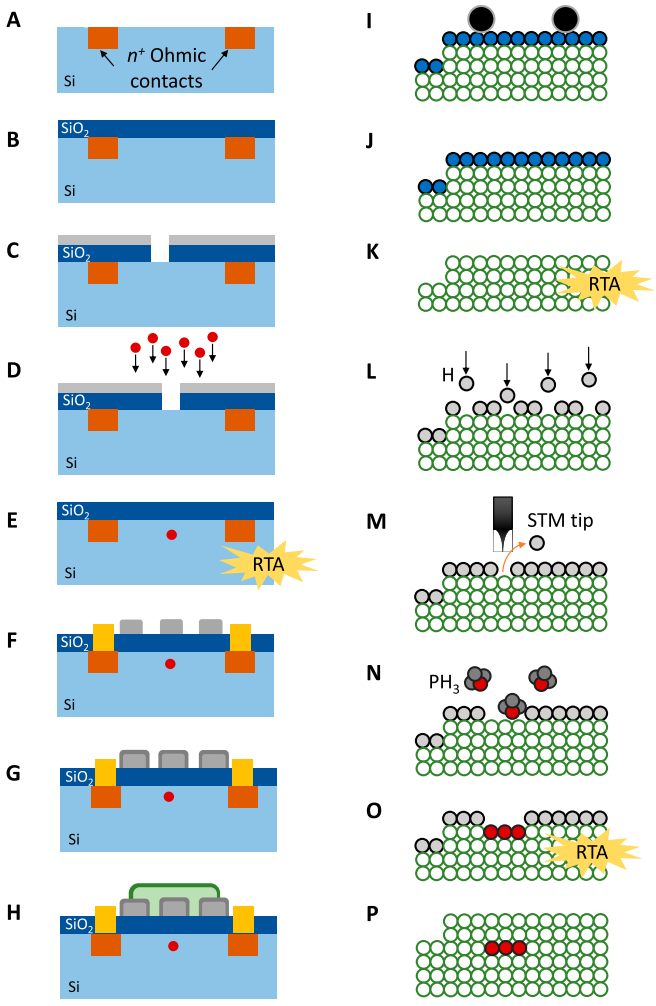

Fig. 5. Fabrication sequences for ion-implanted and STM-patterned MOS devices. (A to H) Process flow for the ion-implanted MOS platform. (A) Formation of ohmic contacts via phosphorus diffusion. (B) Thermal growth of a high-quality oxide top layer. (C) Definition of an aperture for ion implantation. (D) Implantation of phosphorus ions. (E) RTA to repair defects and damages. (F) Fabrication of Al ohmic contact bonding pads and the first layer of gates. (G) Oxidation to form an insulating layer between stacked gates. (H) Stacking of gate layers through repeated cycles. (I to P) Major steps of the STM approach. (I) Wet etching of surface makers, with some potential contamination on the surface. (J) Application of standard silicon cleaning procedures to remove contaminants. (K) Removal of the thin natural oxidation layer and silicon surface reconstruction via high-temperature flash annealing. (L) Production of a hydrogen-terminated surface featuring a monohydride layer. (M) STM atomic precision lithography. (N) Dosing with PH_3. (O) Incorporation annealing to embed phosphorus donors into silicon. (P) Epitaxial growth of a protective silicon layer on top of the device.

Ion-implanted MOS devices

Ion-implanted quantum dot device production [207–209] is compatible with traditional metal-oxide-semiconductor (MOS) chip manufacturing techniques (key steps are shown in Fig. 5A to H). Each device comprises a MOS single-electron transistor (SET) as a charge sensor and close-by implanted phosphorus donors as the qubits. The process begins with either a near-intrinsic natural Si(100) or specially isotopically purified ^{28}Si substrate [30]. The n^+ ohmic contacts for the source and drain are patterned via UV lithography, followed by phosphorus diffusion under ~950 °C. A subsequent step involves growing a 5- to 10-nm-thick high-quality oxide layer through dry thermal oxidation at 800 °C. This is followed by a 5-s rapid thermal annealing (RTA) to minimize interface traps near the conduction-band edge. After the source and drain are fabricated, a 90×90 nm^2 aperture is defined by EBL on polymethyl methacrylate (PMMA) resist, creating the implantation window and protecting the peripheral areas. Phosphorus ions (P^+or P_2^+) are then introduced at energies of 14 to 20 keV to achieve an implantation depth of 10 to 20 nm. Based on Monte Carlo simulation, the ions are randomly implanted into crystalline Si, leading to a lateral position straggle of approximately 10 nm [61]. The mean implanted ion number is meticulously controlled by the ion fluence. Furthermore, to repair the ion-implantation-induced defect cascades or damage clusters within the crystal lattice as well as to activate the donors, a 5-s RTA at 1,000 °C is applied [62].

In the subsequent fabrication, cycles of steps are carried out to place layered gates and dielectric oxide [209]. Aluminum gates are shaped by the EBL, with thermal evaporation and lift-off processes ensuing. Oxide layers are formed with plasma oxidation (4 min, 180 °C), which typically yields a ~5-nm Al_xO_y oxide layer with a breakdown voltage above 4 V. To conclude, a 15-min, 400 °C forming gas annealing (95% N_2 and 5% H_2) is performed to attenuate interface traps and reduce charge noise, which is crucial for operations at low temperatures in the dilution refrigerators. Another approach uses poly-silicon electrodes and applies more sophisticated industrial techniques to fabricate doped Si-MOS quantum devices [210,211].

Donor numbers play a crucial role in achieving controllability and uniformity in qubit arrays, as per Kane's architecture for scalable quantum computing. As aforementioned, the mean implant donor number is controlled via the implantation fluence, which is inherently subject to the Poissonian distribution due to the stochastic nature of the ion sources [62]. Efforts have been made along different technological pathways to decrease uncertainty in the donor number. Recently, a method utilizing an atomic force microscopy (AFM) cantilever as a nanostencil has achieved a remarkable 98.1% implantation yield [212]. This method incorporates an on-chip reverse-biased p-i-n diode detector, which can discern signals from the electron–hole pairs generated through a single-ion implantation event. Typically,

each ion impact event generates approximately 1,000 electron–hole pairs, enabling a 99.85% single-ion-detection confidence by improving the detector performance. The AFM cantilever features a 16-μm-diameter aperture, which serves as a scanning mask to locate the construction sites, where the cantilever with a dimension of 350 × 120 μm^2 acts as a mask to block the remaining ion beam. In the future, a combination of methods [61,62] such as tightly focused ion beams, reduced AFM apertures, and EBL lithographed PMMA masks could further reduce spatial variation. Although the inherent ion straggle remains challenging, heavier ions could be used to mitigate this issue [61].

STM lithographed devices

The second technique developed is hydrogen depassivation lithography (HDL) using STM [213–215], which allows for atomic precision in the fabrication of devices consisting of donors, SETs, and control gates. The major steps to fabricate STM devices are illustrated in Fig. 5I to P. Initially, metallic electrode alignment markers are etched onto a p-type, lightly doped substrate using wet-chemical methods. Next, standard silicon cleaning procedures are performed to remove surface contaminations and the silicon oxidation layer. Then, the sample is loaded into an STM chamber and subjected to a high-temperature flash annealing process (∼1,050 °C for 10 s), resulting in a high-quality Si(100)-2×1 surface suitable for HDL. A monohydride mask layer is formed by exposing the surface to atomic hydrogen from a cracker source. The resulting hydrogen-terminated silicon surface (H-Si) is robust against diffusion up to 200 °C. HDL is employed to pattern features on the hydrogen mask using different STM modes [216]. In a low-bias tunneling mode (2 to 5 V), the lithography achieves sub-nanometer resolution, essentially endorsing an atomic precise (AP) mode. In the high-voltage or field emission (FE) mode (>6 V), wider lines can be lithographed at a higher speed. Notably, single atomic precision hydrogen lithography and repassivation have been demonstrated at 4.5 K [217], establishing this technique as the most precise lithography method. After lithography, the exposed bare silicon surface is dosed with PH_3 molecules, followed by thermal dissociation and incorporation annealing at 350 °C to incorporate phosphorus atoms into the silicon lattice. In the last in situ step, an epitaxial silicon layer approximately 20 to 60 nm thick is grown on top to form the encapsulation layer to protect the patterned structure. Subsequently, the sample is taken out of the STM, then aluminum ohmic contacts and a microwave antenna are fabricated ex situ, enabling the device to function properly.

Deterministic atom placement technologies are essential in the STM route, and several teams have been pursuing this path [215,218]. In 2012, Fuechsle et al. [219] succeeded in fabricating a single phosphorus (P) atom transistor, where the single P is deterministically placed by opening a 3-dimer window, followed by dosing with PH_3 molecules. Upon dosing, 3 PH_3 molecules are absorbed onto the opening and then dissociate into PH_2+H. A series of chemical reactions is triggered by heating the substrate to 350 °C, leaving a single P atom in the window, which is then incorporated into the underlying silicon lattice. Liu et al. [220] also tried applying voltage pulses to the STM tip to steer the dissociation pathway of PH_3 molecules. Later, STM atomic imaging was used to identify adsorption configurations and molecular species, and STM tip manipulation was employed to achieve nearly 100% P atom incorporation [221]. Although deterministic donor array devices for quantum computing have yet to be fully realized, the combination of sophisticated STM tip-assisted surface chemistry and atom manipulation techniques bodes well for precisely engineered P atom arrays. Given that the bond electron Bohr radius is only about 2.5 nm, direct exchange coupled 2-qubit gates put stringent requirements on the precision of the donor's placement (requiring a space as precise as 3 nm [222]), which is a critical factor for scalable donor-based quantum computing.

Qubit initialization and readout

Once donor-based devices are fabricated, LD qubits [113] can be encoded on the donor-bond electron spins. In addition, other qubit types are also explored, including donor nuclear spin qubits [223], dressed qubits encoded on the photon-dressed spin state [224], flip-flop qubits employing the orbital freedom and dipole interactions [74], and singlet–triplet qubits based on 2-electron spin states [155]. A viable physical qubit platform must meet DiVincenzo's criteria [225] to build a programmable quantum computer. In the following, we review crucial advancements in donor-based quantum computing. The important parameters of phosphorus donor spin qubits are summarized in Table 2.

State preparation and measurement

Donor-bond electron spins can be read out in a single-shot manner using a state-to-charge conversion process. This conversion transfers the spin state to a correlated charge tunneling event, which is then detected by an amplified electrical signal. The Elzerman-type spin-dependent process [138] or Pauli spin blockade [226,227] is commonly used to realize the state-to-charge conversion. An SET or a single-lead quantum dot [228] is often fabricated close to the donor to detect the required

Table 2. The quantum performance of the electron spin (e^-), nucleus spin (^{31}P), and ionized nucleus spin ($^{31}P^+$) for phosphorus donors in silicon electronic devices

Property	Parameters	e^-	^{31}P	$^{31}P^+$
Spin coherence	T_1 (s)	9.8(7) [329]	≫100 [223]	-
	T_2^* (ms)	0.268 [30]	1.26 [41]	600 [30]
	T_2^{Hahn} (ms)	0.95 [30]	20 [30]	1,750 [30]
Gate time	T_{1Q} (μs)	0.15 [208]	25 [223]	30 μs [223]
	T_{2Q} (μs)	0.0008 [248]	1.89 [37]	
Gate fidelity	F_1 (%)	99.95 [31]	99.98 [41]	99.99 [31]
	F_2 (%)	86.7(2)[a] [248]	>99[b] [37,41]	

[a] $\sqrt{SWAP}$ gate.

[b] CZ gate.

charge tunneling signal. Using the Elzerman method, a DC readout with 99.6% fidelity has been achieved [229], whereas the RF method has attained a 97% readout fidelity within 1.5 μs [230]. Furthermore, a 98.4% readout fidelity for spin singlet–triplet states has been reported [226]. A novel ramped measurement technique has been developed [231] to improve electron spin readout fidelity and robustness. Single-lead quantum dot readout was also applied to demonstrate its potential for multiplexing readout in a device with 4 donor quantum dots [232]. For nuclear spin states, the readout can be accomplished through discerning the frequencies of the nuclear-spin-correlated ESR transition in a QND approach [223]. The QND method has achieved a nuclear spin readout fidelity exceeding 99.84%. In short, the state-of-the-art electron spin and nuclear spin state readout fidelities satisfy the fault-tolerant requirements of quantum computing.

Spin relaxation and coherence times

Coherence time T_2 is constrained by the upper bound set by the relaxation time T_1 according to the relation $T_2 \leq 2T_1$. Hence, a long T_1 time is the prerequisite for an excellent quantum platform. Notably, the P electron spin in a natural silicon device fabricated by STM showcased a remarkable lifetime of 30 s at a 1.5-T magnetic field [233]. Furthermore, studies exploring the effects of weak SOI have revealed that T_1 can be optimized by adjusting the relative direction of the external field and silicon crystal orientation [234]. Another study achieved a spin lifetime of 6 s in a MOS device [207]. Although the long lifetime sets the upper bound, the pure dephasing time (T_2^*) of donor electron spin in natural silicon was measured as only 55 ns in a MOS device [208]. By applying Hahn echo pulses, a prolonged coherence time of $T_2^{\text{Hahn}} = 206$ μs was realized. In a 1P–2P molecule STM device filled up to the fifth electron, the outer shell electron was shown to have a $T_2^* =$ 295 ns and a $T_2^{\text{Hahn}} = 298$ μs [235], surpassing the 1P case. This enhancement could be due to the reduced hyperfine interaction and suppressed nuclear spin pumping effect during the electron hopping process.

The primary source of decoherence in spin qubits in natural silicon devices is the spectral diffusion caused by the ^{29}Si nuclear spin bath, referred to as the Overhauser field. As creating a nuclear spin-free environment is essential for achieving exceptional coherence times of donor spins, device fabrication using isotopically purified materials is necessary. In the ion-implanted MOS approach, ^{28}Si devices are fabricated by first growing a 0.9-μm-thick isotopically purified ^{28}Si epilayer on a 500 μm-thick $^{\text{nat}}$Si wafer, then followed by similar processes to the implanted P-donor MOS device fabrication in the previous section [30]. A ^{28}Si MOS device exhibits a 1.8-kHz full width at half maximum natural linewidth, corresponding to the expected dephasing time of $T_2^* = 160$ μs, and Hahn echo pulses yield a coherence time of $T_2^{\text{Hahn}} = 0.95$ ms. Implementing the Carr–Purcell–Meiboom–Gill dynamical decoupling pulse sequence extends the coherence time to $T_2^{\text{CPMG}} = 0.56$ s [30]. Furthermore, a record-long coherence time for a $^{31}P^+$ bare nuclei, with $T_2^{\text{CPMG}} = 35.6$ s, was achieved in the same device. As for the other dopants, a coherence time of $T_2^{\text{Hahn}} = 2.7$ s was observed in a Bi device by exploiting the clock transitions [236], and a long coherence time of $T_{2n+}^* = 92$ ms was also reported for an Sb device [237].

Qubit operations

Single-qubit gates

Electron spins can be driven using the standard ESR or EDSR techniques, where EDSR driving usually requires engineered synthetic SOI. Leveraging the extraordinarily long coherence times of the P-donor spins, average Clifford single-qubit gate fidelities of $F_e = 99.90\%$ for electron spin and $F_n = 99.99\%$ for the ionized nuclear spin were revealed using randomized benchmarking [31], both surpassing the fault-tolerant threshold for quantum computing. Furthermore, employing GST to characterize P electron-spin single-qubit gates uncovered systematic errors that the randomized benchmarking does not discern [238]. GST indicates about 4.4% rotation errors in some of the gates. Addressing those errors leads to an enhanced fidelity of $F_e = 99.942\%$. Also, non-Markovian noise is detected from resonant frequency jumps, which can be mitigated by designed pulses to dynamically suppress the errors. Two approaches were proposed to achieve a faster single-qubit gate by EDSR: utilizing the flip-flop (FF) mechanism between a donor bond state and an ionized state [74], and implementing the flopping-mode EDSR driving between 2 quantum dots with asymmetric donor number [239]. A prototype qubit based on the FF mechanism has been demonstrated in a MOS donor device [240], and it has a nuclear spin drive that is 5 times faster than the typical magnetic drive but has a lower fidelity [98.4(2)%]. Furthermore, by combining the ESR and NMR pulses to control the electron spin and donor nuclear spin, electron-nuclear double resonance can be realized. Hence, the electron spin state can be swapped with the nuclear spin, and the electron state can be stored on the long-coherence nuclear spin. In this context, an 80-ms single-atom quantum memory with an overall process storage fidelity of $F \approx 81\%$ was realized [241]. Recently, a novel nuclear spin-driving mechanism based on the nuclear electric resonance phenomena has been demonstrated that utilizes the nuclear quadrupole interaction term of the Sb donor high-spin nuclei with the electric field [237].

Two-qubit gates and entanglement

Two-qubit gates for the donors are difficult to engineer due to the small Bohr radius of the donor-bond electron, which is approximately only 2.5 nm [64]. Furthermore, valley interference causes exchange coupling to oscillate with varying donor distance for 1P–1P [242], making it more difficult to achieve a desired exchange coupling (J). Precise donor placement within a few nanometers is technically essential, but is challenging for the ion-implantation approach [61]. Nevertheless, pursuing two-qubit gates has led to several breakthroughs using fortuitously implanted donor devices, and schemes aimed to alleviate the donor placement limitation have also been proposed [62,74]. In the 1P–1P donor system, a conditional electron spin rotation was realized, with an exchange coupling with $J = 32.06$ MHz between two donor-bonded electrons on an ion-implanted device [243]. Subsequently, a two-qubit CROT gate was reported on a similar device with an always-on exchange interaction of $J = 12$ MHz and an average hyperfine coupling of $\overline{A} = 112$ MHz [244].

The 1P–1P system is traditionally considered convenient for scalability, as per Kane's proposal [204]. The identity of single donors facilitates the calibration of qubit control parameters. Although nuclear spins are used to encode information in Kane's proposal, ensuring the tunability of the exchange coupling

between the two neighboring electrons is crucial. Later, single-donor-based two-qubit gates were studied for different scenarios [188], such as tunable J and fixed always-on type interactions. However, predicting the required donor–donor distance for achieving the target exchange coupling varies substantially across different theoretical studies, making experimental validation of the suitable range of distance range imperative. Meanwhile, several works show that the amplitude of J oscillation varies along different crystalline orientations (refer to [242]). Considering that the donor placement deviates from the ideal axis, the [110] crystallographic axis is recommended [242]. Moreover, the 1P–1P exchange coupling displays lower sensitivity to detuning than the other situations, making it difficult to turn J off [245] effectively. Thus, schemes involving fixed J [188] or using quantum control pulses to mitigate residual J-induced errors [246] should also be explored for achieving high-fidelity quantum gates.

Addressability is another noteworthy point in the 1P–1P system, as the qubits' energies, originating from the Zeeman effect, are the same in a global magnetic field, ESR operations to drive the qubits independently must be addressed properly. There are different methods for tackling the addressability problem, including leveraging local ionized nuclei to provide different hyperfine interactions compared with the electron-bond nuclear state [247], using micromagnet-induced field gradients [43], or utilizing fine-tuned J to achieve different resonant frequencies [35]. Notably, although turning on J can yield different ESR frequencies resolving the addressability issue, it induces cross-talk error due to the unwanted two-qubit Hamiltonian dynamics, where methods need to be developed to address the cross-talk in the presence of the residual J.

The multidonor quantum dot presents another promising route for scaling up. A fast 0.8-ns $\sqrt{\text{SWAP}}$ gate has been successfully demonstrated in an STM-fabricated 2P–3P double dot device featuring a 3.4-GHz exchange coupling with switchable exchange J operation [248]. Furthermore, another device encapsulating 2P–3P dot clusters, separated by 12 nm, allowed the observation of exchange oscillations [249]. This device was used to characterize the charge noise environment and to reveal the donor nuclear spin arrangements [250]. The asymmetric donor number system has some appealing advantages due to its greater flexibility in parameter engineering. Specifically, the asymmetric multidonor design mitigates the J oscillation induced by valley interference and permits extensive electrical tuning of J across a few orders of magnitude [245,248], offering the electrical switchability of J utilizing voltage pulses. Furthermore, initializing nuclear spins in the multidonor dots can generate a large magnetic field gradient, which could help reduce the charge noise influences and enhance CROT gate fidelity [250]. Nonetheless, some specific mechanisms in the multidonor dots that could degrade T_1 and T_2 should be noticed and mitigated. These include hyperfine-mediated spin relaxation [251] and nuclear spin flips induced by measurement backaction [252]. Mitigation tactics entail carefully engineering donor configurations, adjusting stark shifts [253], and utilizing the nuclear freezing effect [254].

Limited donor separation tolerance and short pitch distance pose challenges for placing controlling gates and implementing fan-out [255], particularly for realizing exchange coupling-assisted electron–electron two-qubit gates. Different schemes have been proposed to address these constraints. One approach involves coupling each donor to a MOS gate-defined dot above [256], with the donor electrons indirectly connected via these MOS dots. Along this path, coherent singlet–triplet oscillations have been demonstrated in a donor coupled MOS quantum dot device [257]. This scheme could separate the basic computing unit cell by over 100 nm, with appreciably effective exchange strength for a two-qubit gate. However, it imparts additional complexity to device fabrication and increases susceptibility to charge noise due to the larger electron wave function spread over the MOS dot. A second approach employs the FF mechanism, enabling fast EDSR-based single-qubit driving, and is proposed for devices based on the ion-implanted method, offering considerably longer distances and greater placement precision tolerance [74]. The FF qubit possesses a larger dipole moment by pulling the bonded electron away from donor nuclei. Therefore, a two-qubit gate based on dipole–dipole interaction is feasible. However, the FF qubit requires precise control of the tunneling rate between the bond state and ionized state near the operation "sweet-spot", which is necessary to reduce the impact of charge noise. A third method explores the application of cavity photon-mediated coupling between donor spins [74]. Employing the FF qubit [74] or other EDSR coupling mechanisms [239], donor electrons can be linked via cavity photons. Its physical picture resembles the recently demonstrated long-distance two-qubit gate in the gate-defined quantum dots platform [258]. Nevertheless, the cavity-based approach presents challenges, such as cavity fabrication, achieving strong spin–photon coupling, and the requirement of superconductivity under a strong magnetic field.

Remarkably, two-qubit gates between electron and nuclear spins are relatively easy to realize. In scenarios of a single donor, ESR pulses can conditionally flip the electron spin relative to a specific nuclear spin base state, realizing controlled rotation for the electron spin depending on the nuclear spin [223]. Utilizing this electron-nuclear CROT gate, the construction of a Bell state between donor electron and nuclear spins has been achieved, with a reported state fidelity of $F_{\text{Bell}} > 96\%$ [259]. On another MOS device, where a single electron is shared between two nuclei [37], a geometric two-qubit CZ gate between the nuclear spin qubits has been demonstrated, with asymmetric hyperfine couplings of $A_1 = 95$ MHz and $A_2 = 9$ MHz, respectively. The average single-qubit gate fidelities of the nuclear spins reached 99.95%, and the two-qubit gate fidelity between those two nuclear spins reached 99.37% (see Fig. 6A and B). Moreover, the authors pushed this system to a one-electron–two-nuclei tripartite entanglement, manifesting a 3-qubit GHZ state with a fidelity of 92.5%. Recently, on an STM-fabricated 3P donor cluster device, high-fidelity initialization and control of electron and nuclear spins were demonstrated, and a 4-qubit register was realized on the three nuclear spins and their bonded electron spin [260]. Afterwards, high-fidelity gate operations, 3-qubit GHZ state, and high-performance Grover's algorithm were also demonstrated on this device [41] (see Fig. 6C to E).

Donor arrays and their prospects

The development of a one-dimensional (1D) donor array plays a pivotal role in the quest for scalable donor-based quantum computers. Demonstrations of the feasibility of several critical scaling-up techniques on the 1D donor array are important stepping stones in the process of transitioning to large systems. The most imperative task is developing a multiplexed spin readout technique [232], which requires a high-fidelity spin

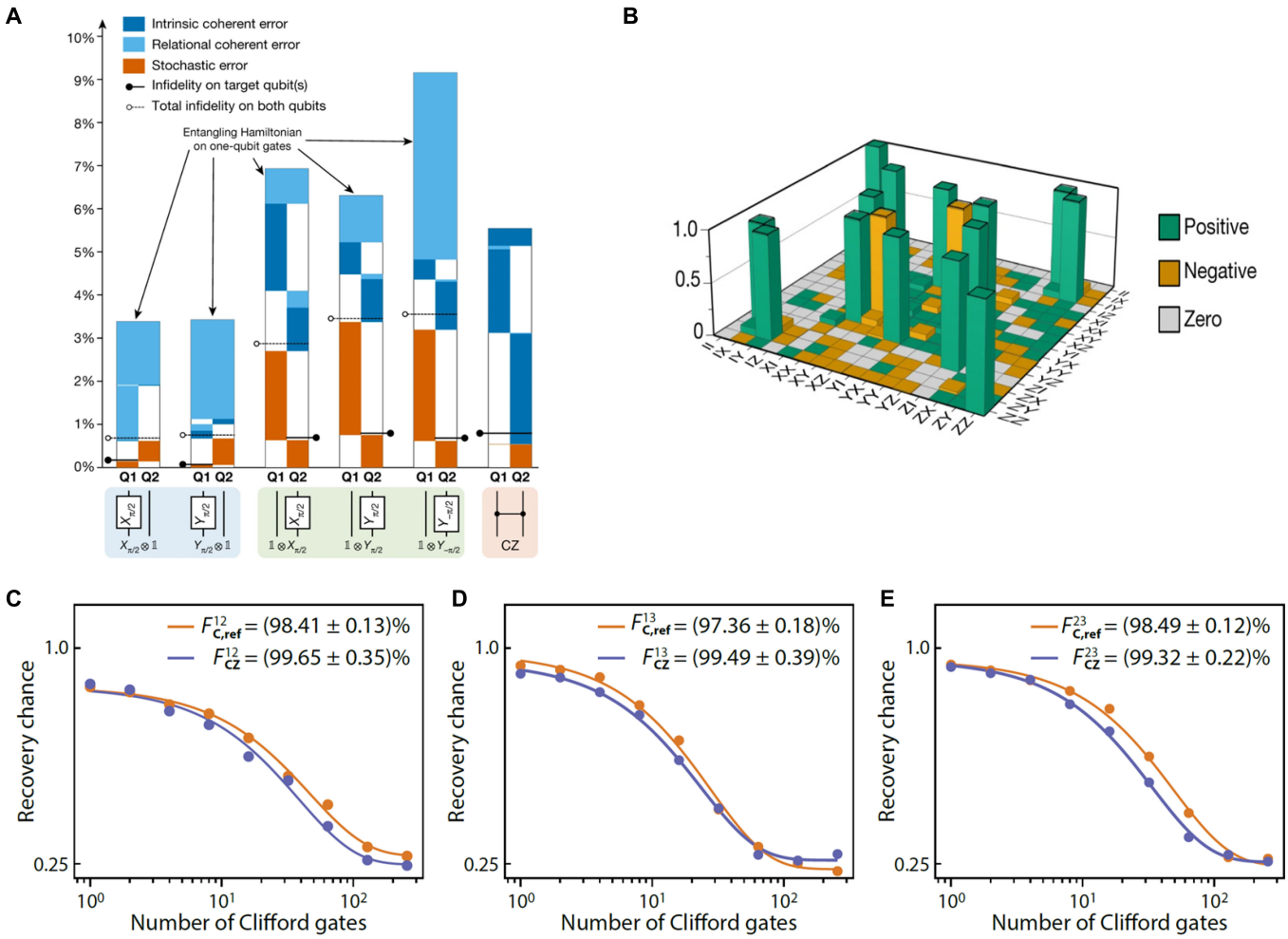

Fig. 6. Two-qubit gate characterization in a donor-based quantum dot. The fidelity of a two-qubit gate based on exchange-coupled electron spins in ^{nat}Si remains below the fault-tolerance threshold [248], and its demonstration in ^{28}Si is yet to be reported. Conversely, the geometric CZ gate between nuclear spins in ^{28}Si has been demonstrated with high fidelity, surpassing the fault-tolerance threshold [37,41]. The GST method enables precise extraction of gate fidelity, distinguishing between various error contributions and separating local errors from cross-talk errors, as illustrated in (A) and (B) [37]. The interleaved randomized benchmarking method was applied for the first time to characterize CZ gates between different nuclei within a donor dot in silicon, achieving fidelities exceeding 99% for all three CZ gates (C to E) [41]. Additionally, different groups have employed Bell states to demonstrate the entanglement capabilities of the two-qubit gates [37,41]. (A) and (B) are adapted from Ref. [37], with permission, Springer Nature. (C), (D), and (E) are adapted from Ref. [41], Springer Nature, under a CC BY license.

readout array. For larger systems, an SET becomes impractical due to the excessive number of electrodes needed for fan-out [195]. A more viable alternative is using a single electron box array combined with a dispersive readout, which reduces the number of electrodes and allows longer sensing distances, consequently facilitating a more straightforward multiplexing process. In addition, the cross-talk issue must be investigated on the 1D donor array. Although a fixed J supports "always-on" type quantum gates [35], achieving ideal single-qubit gates necessitates extensive pulse engineering to effectively mitigate significant J couplings between donors and to isolate a single spin through quantum control methods [246]. Despite those efforts, careful management of cross-talk, as demonstrated in gate-defined quantum dots [43], still needs to be carefully handled for realizing high-fidelity gates, even with switchable J couplings.

Moreover, solving the issue of addressability is equally critical. In unit cells with fixed donor numbers, whether single phosphorus (1P) or multidonor dots, the footprint of tens of nanometers is much smaller than the ESR antenna. Consequently, qubits must be engineered with different energies to solve the addressability issue. Potential means include engineering a tunable Stark effect [253], fabricating a micromagnet to create a magnetic field gradient [43], or using the FF mechanism to achieve hyperfine-assisted tunable single-qubit frequencies at different detuning voltages [74,239]. Furthermore, we also emphasize that the frequency crowding problem is more prominent in large systems; it could be mitigated by resorting to electrical control methods, which would make it easier to realize local interaction than using an AC magnetic field. Thus, EDSR-type single-qubit gates, such as FF gates [74] and multidonor FF gates [239], are more suitable options for much larger systems.

A 2D-donor array is recognized as a suitable platform for realizing fault-tolerant quantum computing, and different architectures have been proposed, such as coherent transport via adiabatic passage [261], MOS dot coupled donor arrays [256], two-donor array planes with cyclic motion [262], donor arrays with shared control lines compatible with surface code [247] (shown in Fig. 7A), and the combination of the FF qubit and superconducting cavities [74] (shown in Fig. 7B). However,

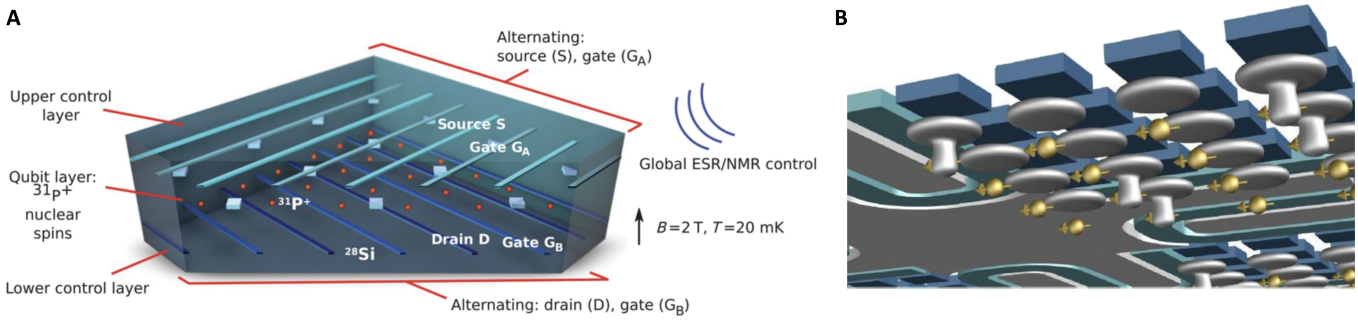

Fig. 7. Scaling-up designs of donor arrays. (A) A two-dimensional donor lattice architecture with shared control lines, which is designed to implement surface code quantum error correction [247] with permission, AAAS. (B) A scalable design optimized for flip-flop qubit configurations, composed of qubit clusters with localized coupling through dipole–dipole interactions and intercluster coupling mediated by shared superconducting microwave cavities [74], Springer Nature, image adapted under a CC BY license.

transitioning from a 1D to a 2D array presents considerable technological challenges. Foremost among these is the issue of fan-out and associated heat dissipation in densely packed arrays [195]. Managing the control and readout lines in a dense donor array is a complex task, necessitating alternatives such as shared control lines, as preliminarily demonstrated in gate-defined quantum dots [200]. In addition, implementing distributed donor arrays and interconnected superconducting cavities [74] will be important in alleviating fan-out difficulties and providing sufficient space for classical control circuits. Addressing fabrication challenges is equally important, calling for considerations of 3D fabrication technology [263,264], silicon vias, precise alignment techniques, flip chip technology, and chiplet technology.

Along with the endeavor of building universal programmable quantum computers, quantum simulation [17] emerges as another vital field for harnessing quantum technology for specific critical tasks in the NISQ era. Donor array systems offer precise control over electron and nuclear arrays and exhibit great potential for numerous quantum simulation tasks. Many renowned physics models can be effectively mapped onto the donor array, such as the Fermi-Hubbard model, the Ising model, and novel topological physics. The Fermi-Hubbard model is particularly important due to its profound relevance to phenomena in high-temperature superconductivity. Previously, the minimal Fermi-Hubbard model was studied in the context of a two-donor system using in situ STM techniques [265]. Furthermore, an extended Fermi-Hubbard model featuring topological states was realized in an STM lithographed 1D multidonor dot array [266]. Theoretical investigations have also explored the single-donor-based dimerized Fermi-Hubbard chain and associated Su-Schrieffer-Heeger topological physics [267,268]. Moreover, theoretical examinations of a 2D array for the extended Fermi-Hubbard model have been conducted [269]. Recently, a 3 × 3 multidonor dot array with the finite disorder was fabricated, yielding preliminary observations of a transport transition from the metallic phase to the Mott insulating phase [270]. Although technologies for precise control of donor numbers and tunneling rates are still under development, the avenue toward donor array quantum simulation for many-body physics has been already opened.

Spin–Photon Interface for Scaling up

As discussed above, rapid development in spin qubits coupled via direct exchange interactions has granted this platform credibility as a leading candidate for quantum computation. However, while being highly compatible with advanced semiconductor manufacturing technology [25,28,42,50,134,136], the complexity in multiplexing due to intrinsic nonuniformity and cross-talk in quantum operations makes fan-out of control and read-out wires in a large qubit array a challenge that is yet to be solved. The most promising solution is to build distributed modules consisting of exchange-coupled spin qubits and interconnect them with long-range couplers. A variety of attempts to achieve long-distance spin coupling have been made, such as directly shuttling the charge carriers electrically via the bucket-brigade mode [143,144,271–273] or the conveyor (or moving quantum dot) mode [274–280] using voltage pulses or acoustically using surface acoustic waves [281,282]. On the other hand, circuit quantum electrodynamics (cQED) using microwave photons in superconducting resonators has been demonstrated as a powerful approach that can easily transfer quantum information between spin qubits that are several hundred micrometers apart and the operation speed is not constrained by the distance. Moreover, the spin-cQED architecture also opens up opportunities in rapid spin qubit readout [283,284] and quantum simulation [285]. Here, we briefly review the key breakthroughs in spin-cQED studies.

To ensure efficient interaction between spin qubits and microwave photons before the system loses coherence, the strong coupling [286] condition must be satisfied: $g_s > \max\left[\gamma_s,\kappa\right]$, where the g_s is the spin–photon coupling strength, γ_s is the spin qubit decoherence rate, and κ represents the photon loss rate in the cavity. Although the extremely small magnetic dipole makes spin qubits immune to environment noise and allows for long coherence times, it also poses challenges in achieving strong coupling between spins and external microwave photons; coupling is typically limited to a strength of ~1 kHz [287]. To overcome this bottleneck, methods for hybridizing the spin and charge degrees of freedom have been proposed and demonstrated, facilitating a sizeable coupling between the spin and cavity modes [286,288].

The spin–photon coupling strength g_s is directly dependent on the charge-photon coupling strength g_c. To maximize g_c, the first step is to delocalize the electron (or hole) between two tunnel-coupled quantum dots, meaning the charge state is degenerate between (1,0) and (0,1) (or at an equivalent interdot transition), where the electric dipole moment is maximized. Second, as g_c is proportional to $\sqrt{Z_c}$ (where Z_c is the characteristic impedance of the resonator), resonators are typically made of superconducting materials with high kinetic inductance materials such as NbTiN [289] and granular Al [290,291],

or arrays of superconducting quantum interference devices [292]. Last, since the resonators are galvanically connected to the gates that confine the quantum dots, g_c therefore is also determined by the lever arm [58], which is related to the capacitive coupling between the confined electrons in the dot and the surrounding gates, and can be optimized through electrostatic gate layout design.

A charge-photon coupling rate of a few hundred megahertz can now be easily achieved in different types of devices [58,291,293], which paves the way toward strong spin–photon couplings. In order to couple the spin degree of freedom to photons in a resonator, the spins must be coupled to the charge states that mediate the coupling to photons, as previously discussed. The most straightforward mechanism is the SOI, which is intrinsically lacking for electrons in silicon, and therefore, micromagnets have been implemented to provide synthetic SOI to enable spin–photon couplings [294,295]. In contrast, intrinsic SOI can be utilized for hole spins in silicon and germanium [58,291,296,297]. The second method for coupling spin and charge states is via exchange interactions, which is directly dependent on the distance between adjacent spins. This mechanism can be utilized to couple singlet–triplet qubits and exchange-only qubits, where the qubit is defined in a subspace of multiple spin states [298,299].

Strong coupling between spin and photon in silicon-based DQDs was first realized in 2018 by two groups [294,295]. A typical device for spin–photon coupling is shown in Fig. 8A, where the electron is confined under the overlapping plunger and barrier gates. In this device, which utilizes the DQD design with a micromagnet, the oscillating electron experiences an inhomogeneous stray field (Fig. 8B), which hybridizes spin and charge states and entails an indirect spin–photon coupling. The vacuum Rabi splitting at cavity transmission is observed (Fig. 8C) by scanning the probe frequency and magnetic field. The g_s is determined to be 5.5 MHz, which is larger than $\gamma_s = 2.4$ MHz and $\kappa = 1.8$ MHz. Figure 8E shows the similar vacuum Rabi splitting observed in another device, a device with single-layer gate electrodes, as shown in Fig. 8D. The corresponding g_s, γ_s, and κ of this device are 10, 1.8, and 4.2 MHz, respectively. Apart from the transverse component of synthetic SOC, longitudinal spin–photon coupling, which is not affected by the Purcell effect, has also recently been demonstrated with $g_s > 1$ MHz [300].

To realize intermodule quantum information processing, resonators have been applied to couple qubits at a distance. Several groups have achieved distant couplings between the charge states of two distant DQDs [301,302], coherent coupling between a single charge and a superconducting qubit [303], and collective coupling involving 5 DQDs coupled to a common resonator [304]. However, coupling spins at a distance via the resonator is more challenging compared to charge–dipole coupling, as it requires establishing strong spin–photon coupling as a prerequisite. Long-distance coupling between two remote spins was demonstrated shortly after realizing the strong coupling [294,295]. As shown in Fig. 9A and B, two remote spins in a silicon DQD, separated by about 4 mm, are coupled to each end of the SC cavity [305]. To individually tune the frequencies of the two spin qubits, a cobalt micromagnet is arranged with a

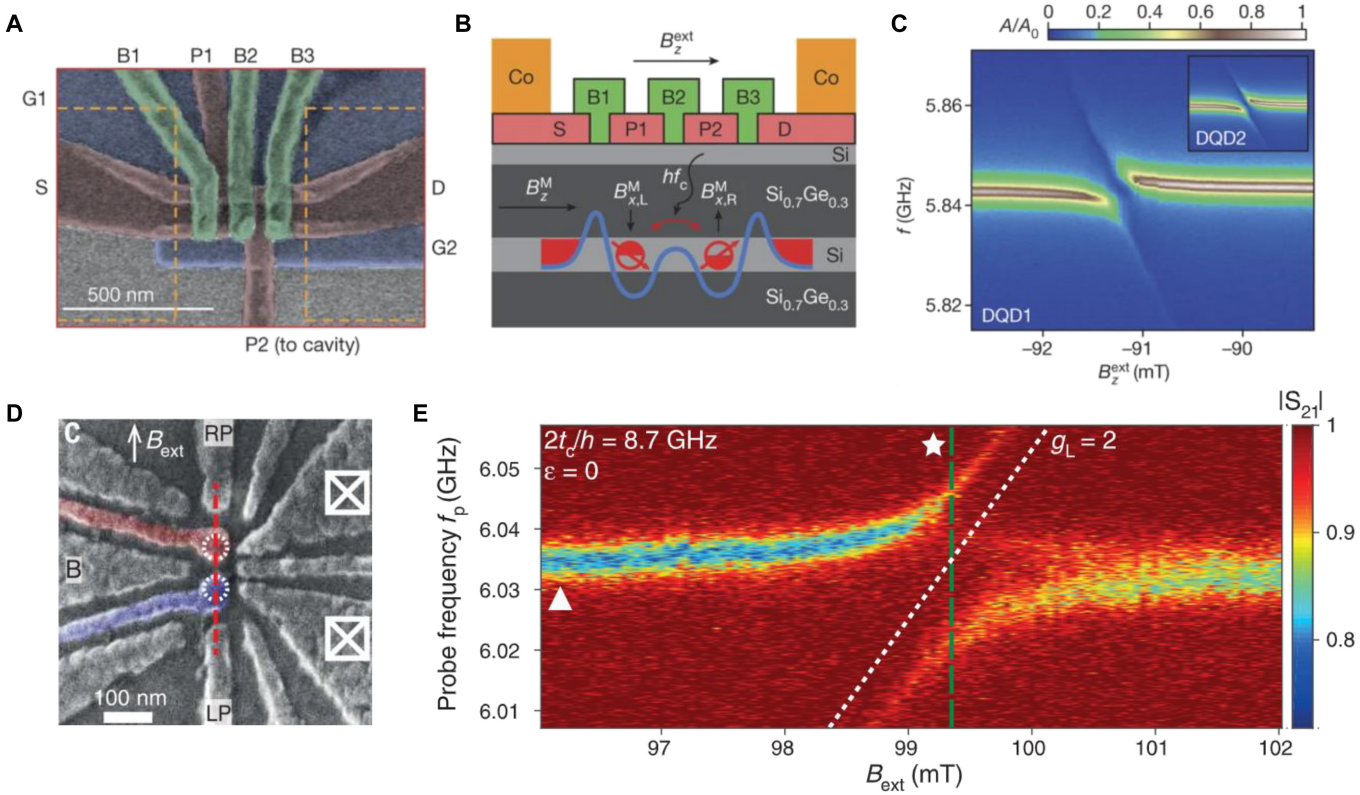

Fig. 8. Strong coupling between silicon spin qubit and microwave photon. (A) A scanning electron microscope image of a silicon DQD device with overlapping gate electrodes. (B) Schematic of a DQD device cross-section. (C) Vacuum Rabi splitting indicates strong spin–photon coupling, observed in the device shown in (A). (D) Scanning electron microscope image of a DQD device with single-layer electrodes. (E) Vacuum Rabi splitting from the device in (D). (A) to (C) are adapted from Ref. [294], with permission, Springer Nature. (D) and (E) are adapted from Ref. [295], with permission, AAAS.

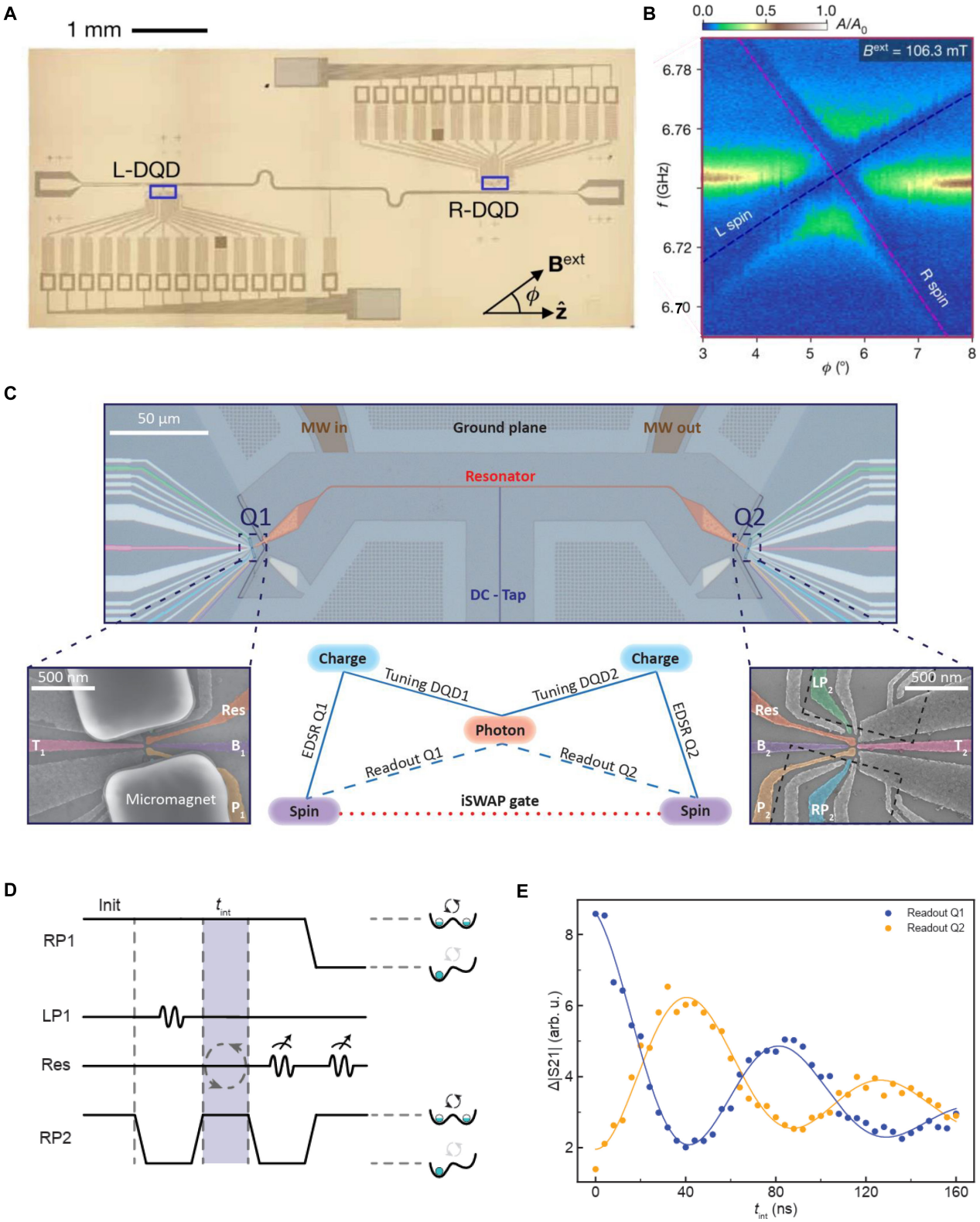

Fig. 9. Cavity-mediated long-distance coupling and a SWAP gate between remote spin qubits. (A) Optical picture of a superconducting resonator that couples two distant DQDs at its ends. (B) Resonate coupling between two spin qubits via the superconducting resonator by fine-tuning of the magnetic field angle. (C) Optical picture of a hybridized device for long-distance SWAP operation. Insets (from left to right): scanning electron microscope image of left DQD (Q1) with tilted micromagnet arrangement; schematic of the distant spin–spin coupling architecture; scanning electron microscope image of right DQD (Q2). (D) Pulse sequence for the virtual photon-mediated long-distance SWAP operation. (E) State evolution of Q1 and Q2 during SWAP operation. (A) and (B) are adapted from Ref. [305], with permission, Springer Nature. (C) to (E) are adapted from Ref. [258], with permission, Springer Nature.

tilted angle of 15° (see the inset in Fig. 9C for details). By adjusting the magnitude and direction of the magnetic field, two spin qubits simultaneously resonate with the microwave photon, resulting in an enhanced vacuum Rabi splitting, with a collective coupling of 32.1 MHz. Moreover, dispersive coupling between two remote spins via virtual photon interaction has also been realized [293], where the exchange coupling strength between the two remote spin qubits was measured at 19 MHz, exceeding the spin linewidths.

All of the above efforts make the cQED a critical method for spin-qubit scalability. Microwave photon-mediated coherent quantum state transfer is a key step for quantum multicore processors and distributed architectures [195,306]. Recently, Dijkema et al. [258] successfully demonstrated the virtual photon-mediated long-distance SWAP operation in a hybrid quantum dot–resonator dot device (Fig. 9C), which stands as a milestone for scalable silicon quantum network. The time-domain control of spin–photon coupling by pulsing on the detuning of quantum dot as schematized in Fig. 9D makes quantum information sequentially transfer between the left DQD (Q1), resonator, and right DQD (Q2). Therefore, the long-distance coupled two-spin qubit state oscillates during the evolution process and is directly detected by the resonator, as shown in Fig. 9E. These results suggest that superconducting resonators can provide a feasible approach for connecting distant qubit arrays and therefore achieve a large-scale spin-based quantum computing chip.

Outlook

In summary, the spin qubit for quantum computing has experienced fast development over the last decades, with advancements including high-fidelity operation, high-temperature operation, fast spin manipulation, and strong spin–phonon coupling. However, further improvement of gate fidelity, cross-talk migration, multiqubit operation, spin transportation, and multidimensional spin–photon coupling is needed for scaling up. Novel schemes and architectures are also needed for global control [109,194] and scalable engineered driving mechanisms, such as site-dependent spin quantization axes for hopping qubits [40,307] and micromagnet arrays for EDSR-type driving spin qubits [308]. Here, we outline possible future directions for spin qubits in silicon.

Gate-defined quantum dots

The future of silicon qubits in quantum computing looks promising due to major improvements in materials science, microfabrication, and quantum control. Silicon works well with existing semiconductor technology, which facilitates the integration of qubits into microelectronic systems. Improvements in materials like Si/SiGe and Si-MOS have enhanced control over key properties such as valley splitting [119] and electron mobility [122]. However, the task of improving material quality and searching for new materials is far from complete [115]. Newly emerging materials such as planar germanium have shown potential in fast spin operation [202] and large array construction [44,60]. Improved gate designs have also increased the density and uniformity of qubit arrays, making it possible to create large arrays of qubits. The ability to operate at temperatures ranging from 1 to 4 K [38,46] provides opportunities for integration with cryo-electronics [48,49].

Readout [142,146,148] and control fidelity [32,33,35,36,39,43,103,141] are sufficient for error correction. Looking ahead, integrating silicon qubits with on-chip classical control, exploring new 2D and 3D qubit array layouts [195–197], and possibly operating at higher temperatures are important research areas. These efforts aim to tackle scalability and functionality challenges. Open questions remain, including how to effectively communicate with classical electronics, the optimal wiring scheme for connectivity, the ideal size for quantum dot modules, and the scaling law of noise properties. In particular, spatially correlated noise [174,178] creates interdependencies across qubits, prompting questions about the optimal encoding scheme and material stack for qubit performance.

Donor dots

We anticipate diverse and promising future directions for donor quantum computing systems. Furthermore, combining such systems with "hot qubits" [45–47] and cryo-CMOS technology [48,309] opens up the potential for an on-chip silicon quantum computing system operating within the 1 to 4 K temperature range. Considering the deep potential of donors to confine bonded electrons [219], "hot qubits" will enhance the attainability of higher gate fidelities at elevated temperatures. As mentioned, leveraging high-spin nuclei combined with nuclear electric resonance control provides a novel platform for donor nuclear spin systems [237]. With high-spin nuclei, quantum computing based on qudits presents intriguing topics for exploration, such as demonstrating spin state squeezing and cat states. Recently, the creation and manipulation of Schrödinger cat states using the spin-7/2 nucleus of an Sb donor were also realized [310]. Meanwhile, integrating a flying photon into the donor systems is possible. Other dopants, such as erbium [311] and selenium [312], offer the potential for coupling a flying qubit to the donor spin, which can considerably extend the coupling distance between dopants for distributed quantum computing and quantum internet. Notably, a recent study demonstrated 0.8 to 1.2 ms coherence time for erbium ions in silicon [311].

Regarding large-scale universal quantum computing, donor array fabrication techniques are still challenging and require further development. Although deterministic ion implantation has been demonstrated [212], methods that could further reduce spatial variation during ion implantation—such as using AFM apertures, EBL lithographed masks, and heavy ions—are still developing and have not yet become mature and reliable [61,62]. In terms of the STM lithography route, integrating the deterministic donor array technique [221] into chip fabrication is crucial to ensuring compatibility with the overall fabrication process.

For the integration of quantum functionalities, several potential solutions must be considered, optimized, and implemented, including multiplexed single-lead quantum dots for RF readout [232], micromagnets to address the addressability issue [43], fine-tuned J gates for high on–off ratio two-qubit gates [35], incorporation of MOS gate-defined dots with the application of FF qubits [74], and spin–photon coupling cavities for a modular architecture [74]. Meanwhile, other scaling-up issues are commonly shared between the donor-based approach and gate-defined quantum dots. These issues are discussed in the following section. Despite the inherent challenges associated with fabricating donor devices, technological advancements are underway. We are optimistic that donor systems have a promising future in building large-scale donor-based quantum computers.

Scaling up

One of the outstanding advantages of spin qubits in quantum dots is the small footprint of only tens to hundreds of nanometers depending on the exact gate structures [29], which makes it possible to place dense arrays at large scale on a small chip. At the same time, the fabrication of quantum dots is based on a precise process. In pioneer works, silicon quantum dots are usually fabricated in a laboratory process by EBL and lift-off metallization. This process has low yield [136] and induces considerable charge noise at the interface, resulting in a low success rate for quantum dot arrays. Recently, leveraging advanced semiconductor manufacturing technologies, Intel adopted the FinFET structure to integrate more than 10,000 1D quantum dot arrays with a yield exceeding 90% [136]. Then, 1D arrays of overlapping gates combined with Co micromagnets have also been fully manufactured by an industrial 300-mm semiconductor wafer process line [313]. However, a 2D array is crucial for future scaling up. Although researchers have attempted to fabricate small 2D arrays by adopting single-layer or overlapping gate structures in lab processes, the relatively poor connectivity remains a challenge for the wiring and fan-out of future large-scale 2D arrays. To increase 2D connectivity, SLEDGE devices have been successfully fabricated [57]. SLEDGE devices consist of uniplanar gate electrodes etched in quantum dot shapes and back-end-of-line metal layers vertically connected to gate electrodes for wiring [57]. Very recently, SLEDGE quantum dots have also been successfully fabricated in industrial lines [42]. Moreover, the fidelity of single-qubit operation in triangle 2D SLEDGE quantum dots array has exceeded 99%, further indicating that SLEDGE is a promising technology for future larger 2D arrays with high connectivity [56]. The crossbar structure [198,200] is also a promising choice, one that can considerably decrease the complexity of wiring and fan-out, but it requires a high uniformity of quantum dots.

From an operation perspective, the continuous improvement of fidelity to well beyond 99% is necessary. So far, most high-fidelity (>99%) spin qubit operations have been performed on small quantum dot arrays [32,33,36,37,39,103,258]. For large-scale arrays, inhomogeneity and disorder in the wafer decrease the performance of qubit operations compared to that in small arrays. The optimization of wafer growth, especially for SiGe, through solving lattice mismatch [314] and interface state [315,316] will reduce charge noise and mitigate valley splitting [317] to homogenize the whole wafer, which is a benefit for increasing the fidelity of qubit operations in a large-scale array. In addition, the heating effect from qubit operations should not be ignored, especially for large-scale arrays. The "hot" spin qubit is an important advancement [38,45–47,184] and can operate above 1 and even 4 K. It would provide much larger cooling power and more conveniently integrate with cryo-electronics [318].

From an architecture perspective, the multimodular quantum chip [306] can be used to integrate all of the above advantages, which should further reduce the complexity of wiring, fan-out, and cross-talk. For intramodular design, the industrial foundry processes will accelerate the construction of 2D crossbar [198,200] and 3D wiring structure [57] of spin qubit arrays to reduce the demand for electrode resources. For intermodular connection, cQED remains a powerful scheme, although the improvement of γ_s and κ in quantum dot-cavity hybridization devices is necessary [258,293,305]. As the number of integrated modules and resonators continues to increase, layout complexity is an unavoidable challenge, but can be solved using the 3D stacking flip-chip technique [300]. In addition, conveyor-mode spin qubit shuttling [280] has achieved important successes on micrometer-scale quantum information transfer with fidelity exceeding 99%, and is also a promising choice for intermodular connection. Super-exchange between distant spins, jellybean quantum dots [319], and surface acoustic waves [282] can serve as alternative methods for medium long-range coupling.

Acknowledgments

Funding: This work was supported by the National Natural Science Foundation of China (grant nos. 92165210, 62174076, 12304560, 92265113, 12074368, and 12034018), the Innovation Program for Quantum Science and Technology (no. 2021ZD0302300), the Science, Technology and Innovation Commission of Shenzhen Municipality (grant no. KQTD-20200820113010023), and the China Postdoctoral Science Foundation (grant nos. BX20220281 and 2023M733408). X.X. acknowledges support from the Dutch Research Council (NWO) via the National Growth Fund programme Quantum Delta NL (grant no. NGF.1623.23.024).
Author contributions: Y.H. and G.H. wrote the abstract and introduction. P.H. and L.W. wrote the theory section. W.W.H. and C.H.Y. wrote the gate-defined quantum dots section. G.H. and Y.H. wrote the dopants section. X.X., R.C., and G.C. wrote the spin–photon interface section. G.H., P.H., W.W.H., Y.H., X.X., and R.C. wrote the outlook section. The manuscript was revised by all authors.
Competing interests: The authors declare that they have no competing interests.

Data Availability

There is no dataset associated with this review article.

References

1. 40 Years of quantum computing. *Nat Rev Phys*. 2022;4:1.
2. Dowling JP, Milburn GJ. Quantum technology: The second quantum revolution. *Philos Trans A Math Phys Eng Sci*. 2003;361(1809):1655–1674.
3. Nielsen MA, Chuang IL. *Quantum computation and quantum information*, 10th anniversary edition ed. Cambridge (NY): Cambridge University Press; 2010.
4. Bharti K, Cervera-Lierta A, Kyaw TH, Haug T, Alperin-Lea S, Anand A, Degroote M, Heimonen H, Kottmann JS, Menke T, et al. Noisy intermediate-scale quantum algorithms. *Rev Mod Phys*. 2022;94(1):Article 015004.
5. Montanaro A. Quantum algorithms: An overview. *npj Quantum Inf*. 2016;2(1):15023.
6. Preskill J. Quantum computing in the NISQ era and beyond. *Quantum*. 2018;2:79.
7. Arute F, Arya K, Babbush R, Bacon D, Bardin JC, Barends R, Biswas R, Boixo S, Brandao FGSL, Buell DA, et al. Quantum supremacy using a programmable superconducting processor. *Nature*. 2019;574:505–510.
8. Wu Y, Bao WS, Cao S, Chen F, Chen MC, Chen X, Chung TH, Deng H, Du Y, Fan D, et al. Strong quantum computational advantage using a superconducting quantum processor. *Phys Rev Lett*. 2021;127(18):Article 180501.

9. Zhong HS, Wang H, Deng YH, Chen MC, Peng LC, Luo YH, Qin J, Wu D, Ding X, Hu Y, et al. Quantum computational advantage using photons. *Science*. 2020;370:1460–1463.
10. Zhong HS, Deng YH, Qin J, Wang H, Chen MC, Peng LC, Luo YH, Wu D, Gong SQ, Su H, et al. Phase-programmable Gaussian boson sampling using stimulated squeezed light. *Phys Rev Lett*. 2021;127(18):Article 180502.
11. Madsen LS, Laudenbach F, Askarani MF, Rortais F, Vincent T, Bulmer JFF, Miatto FM, Neuhaus L, Helt LG, Collins MJ, et al. Quantum computational advantage with a programmable photonic processor. *Nature*. 2022;606:75–81.
12. Deng YH, Gu YC, Liu HL, Gong SQ, Su H, Zhang ZJ, Tang HY, Jia MH, Xu JM, Chen MC, et al. Gaussian boson sampling with pseudo-photon-number-resolving detectors and quantum computational advantage. *Phys Rev Lett*. 2023;131(15):Article 150601.
13. Ni Z, Li S, Deng X, Cai Y, Zhang L, Wang W, Yang ZB, Yu H, Yan F, Liu S, et al. Beating the break-even point with a discrete-variable-encoded logical qubit. *Nature*. 2023;616:56–60.
14. Sivak VV, Eickbusch A, Royer B, Singh S, Tsioutsios I, Ganjam S, Miano A, Brock BL, Ding AZ, Frunzio L, et al. Real-time quantum error correction beyond break-even. *Nature*. 2023;616:50–55.
15. Google Quantum AI and Collaborators. Quantum error correction below the surface code threshold. *Nature*. 2024;638:920–926.
16. Andersen TI, Lensky YD, Kechedzhi K, Drozdov IK, Bengtsson A, Hong S, Morvan A, Mi X, Opremcak A, Acharya R, et al. Non-abelian braiding of graph vertices in a superconducting processor. *Nature*. 2023;618(7946):264–269.
17. Georgescu IM, Ashhab S, Nori F. Quantum simulation. *Rev Mod Phys*. 2014;86(1):153–185.
18. Zaletel MP, Lukin M, Monroe C, Nayak C, Wilczek F, Yao NY. Colloquium: Quantum and classical discrete time crystals. *Rev Mod Phys*. 2023;95(3):Article 031001.
19. Da Silva MP, Ryan-Anderson C, Bello-Rivas JM, Chernoguzov A, Dreiling JM, Foltz C, Frachon F, Gaebler JP, Gatterman TM, Grans-Samuelsson L, et al. Demonstration of logical qubits and repeated error correction with better-than-physical error rates. arXiv. 2024. https://doi.org/10.48550/arXiv.2404.02280
20. Bluvstein D, Evered SJ, Geim AA, Li SH, Zhou H, Manovitz T, Ebadi S, Cain M, Kalinowski M, Hangleiter D, et al. Logical quantum processor based on reconfigurable atom arrays. *Nature*. 2024;626(7997):58–65.
21. Steane AM. Space, time, parallelism and noise requirements for reliable quantum computing. *Fortschritte der Physik*. 1998;46(4–5):443–457.
22. Gidney C, Ekerå M. How to factor 2048 bit RSA integers in 8 hours using 20 million noisy qubit. *Quantum*. 2021;5:433.
23. Bravyi S, Cross AW, Gambetta JM, Maslov D, Rall P, Yoder TJ. High-threshold and low-overhead fault-tolerant quantum memory. *Nature*. 2024;627(8005):778–782.
24. Vinet M. The path to scalable quantum computing with silicon spin qubits. *Nat Nanotechnol*. 2021;16(12):1296–1298.
25. Neyens S, Zietz OK, Watson TF, Luthi F, Nethwewala A, George HC, Henry E, Islam M, Wagner AJ, Borjans F, et al. Probing single electrons across 300-mm spin qubit wafers. *Nature*. 2024;629(8010):80–85.
26. Steinacker P, Stuyck ND, Lim WH, Tanttu T, Feng M, Nickl A, Serrano S, Candido M, Cifuentes JD, Hudson FE, et al. A 300 mm foundry silicon spin qubit unit cell exceeding 99% fidelity in all operations. arXiv. 2024. https://doi.org/10.48550/arXiv.2410.15590
27. Ansaloni F, Chatterjee A, Bohuslavskyi H, Bertrand B, Hutin L, Vinet M, Kuemmeth F. Single-electron operations in a foundry-fabricated array of quantum dots. *Nat Commun*. 2020;11(1):6399.
28. Stuyck ND, Saraiva A, Gilbert W, Pardo JC, Li R, Escott CC, Greve KD, Voinigescu S, Reilly DJ, Dzurak AS. CMOS compatibility of semiconductor spin qubits. arXiv. 2024. https://doi.org/10.48550/arXiv.2409.03993
29. Burkard G, Ladd TD, Pan A, Nichol JM, Petta JR. Semiconductor spin qubits. *Rev Mod Phys*. 2023;95(2):Article 025003.
30. Muhonen JT, Dehollain JP, Laucht A, Hudson FE, Kalra R, Sekiguchi T, Itoh KM, Jamieson DN, McCallum JC, Dzurak AS, et al. Storing quantum information for 30 seconds in a nanoelectronic device. *Nat Nanotechnol*. 2014;9(12):986–991.
31. Muhonen JT, Laucht A, Simmons S, Dehollain JP, Kalra R, Hudson FE, Freer S, Itoh KM, Jamieson DN, McCallum JC, et al. Quantifying the quantum gate fidelity of single-atom spin qubits in silicon by randomized benchmarking. *J Phys Condens Matter*. 2015;27(15):Article 154205.
32. Yang CH, Chan KW, Harper R, Huang W, Evans T, Hwang JCC, Hensen B, Laucht A, Tanttu T, Hudson FE, et al. Silicon qubit fidelities approaching incoherent noise limits via pulse engineering. *Nat Electron*. 2019;2:151–158.
33. Mills AR, Guinn CR, Gullans MJ, Sigillito AJ, Feldman MM, Nielsen E, Petta JR. Two qubit silicon quantum processor with operation fidelity exceeding 99%. *Sci Adv*. 2022;8(14):eabn5130.
34. Lawrie WIL, Rimbach-Russ M, Fv R, Hendrickx NW, Snoo SL, Sammak A, Scappucci G, Helsen J, Veldhorst M. Simultaneous single-qubit driving of semiconductor spin qubits at the fault-tolerant threshold. *Nat Commun*. 2023;14(1):3617.
35. Noiri A, Takeda K, Nakajima T, Kobayashi T, Sammak A, Scappucci G, Tarucha S. Fast universal quantum gate above the fault-tolerance threshold in silicon. *Nature*. 2022;601:338–342.
36. Xue X, Russ M, Samkharadze N, Undseth B, Sammak A, Scappucci G, Vander Sypen LMK. Quantum logic with spin qubits crossing the surface code threshold. *Nature*. 2022;601(7893):343–347.
37. Madzik MT, Asaad S, Youssry A, Joecker B, Rudinger KM, Nielsen E, Young KC, Proctor TJ, Baczewski AD, Laucht A, et al. Precision tomography of a three-qubit donor quantum processor in silicon. *Nature*. 2022;601:348–353.
38. Huang JY, Su RY, Lim WH, Feng M, van Straaten B, Severin B, Gilbert W, Dumoulin Stuyck N, Tanttu T, Serrano S, et al. High-fidelity spin qubit operation and algorithmic initialization above 1 K. *Nature*. 2024;627(8005):772–777.
39. Tanttu T, Lim WH, Huang JY, Dumoulin Stuyck N, Gilbert W, Su RY, Feng M, Cifuentes JD, Seedhouse AE, Seritan SK, et al. Assessment of the errors of high-fidelity two-qubit gates in silicon quantum dots. *Nat Phys*. 2024;20(11):1804–1809.
40. Wang CA, John V, Tidjani H, Yu CX, Ivlev AS, Déprez C, van Riggelen-Doelman F, Woods BD, Hendrickx NW, Lawrie WI, et al. Operating semiconductor quantum processors with hopping spins. *Science* 2024;385(6707):447–52.
41. Thorvaldson I, Poulos D, Moehle CM, Misha SH, Edlbauer H, Reiner J, Geng H, Voisin B, Jones MT, Donnelly MB, et al. Grover's algorithm in a four-qubit silicon processor above the

fault-tolerant threshold. *Nat Nanotechnol*. 2025. https://doi.org/10.1038/s41565-024-01853-5
42. Weinstein AJ, Reed MD, Jones AM, Andrews RW, Barnes D, Blumoff JZ, Euliss LE, Eng K, Fong BH, Ha SD, et al. Universal logic with encoded spin qubits in silicon. *Nature*. 2023;615(7954):817–822.
43. Philips SGJ, Mądzik MT, Amitonov SV, de Snoo SL, Russ M, Kalhor N, Volk C, Lawrie WIL, Brousse D, Tryputen L, et al. Universal control of a six-qubit quantum processor in silicon. *Nature* 2022;609(7929):919–924.
44. Hendrickx NW, Lawrie WIL, Russ M, van Riggelen F, de Snoo SL, Schouten RN, Sammak A, Scappucci G, Veldhorst M. A four-qubit germanium quantum processor. *Nature* 2021;591(7851):580–585.
45. Petit L, Eenink HGJ, Russ M, Lawrie WIL, Hendrickx NW, Philips SGJ, Clarke JS, Vander Sypen LMK, Veldhorst M. Universal quantum logic in hot silicon qubits. *Nature*. 2020;580(7803):355–359.
46. Yang CH, Leon RCC, Hwang JCC, Saraiva A, Tanttu T, Huang W, Lemyre JC, Chan KW, Tan KY, Hudson FE, et al. Operation of a silicon quantum processor unit cell above one kelvin. *Nature*. 2020;580(7803):350–354.
47. Camenzind LC, Geyer S, Fuhrer A, Warburton RJ, Zumbühl DM, Kuhlmann AV. A hole spin qubit in a fin field-effect transistor above 4 kelvin. *Nat Electron*. 2022;5(3):178–183.
48. Xue X, Patra B, van Dijk JPG, Samkharadze N, Subramanian S, Corna A, Paquelet Wuetz B, Jeon C, Sheikh F, Juarez-Hernandez E, et al. CMOS-based cryogenic control of silicon quantum circuits. *Nature*. 2021;593(7858):205–210.
49. Pellerano S, Subramanian S, Park JS, Patra B, Mladenov T, Xue X, Vandersypen LMK, Babaie M, Charbon E, Sebastiano F. Cryogenic CMOS for Qubit Control and Readout. In: *2022 IEEE custom integrated circuits conference (CICC)*. Newport Beach (CA): IEEE; 2022. p. 1–8.
50. Li R, Stuyck NID, Kubicek S, Jussot J, Chan BT, Mohiyaddin FA, Elsayed A, Shehata M, Simion G, Godfrin C, et al. A flexible 300 mm integrated Si MOS platform for electron- and hole-spin qubits exploration. In*: 2020 IEEE International Electron Devices Meeting (IEDM)*. San Francisco (CA): IEEE; 2020. p. 38.3.1–38.3.4.
51. Shi Z, Simmons CB, Ward DR, Prance JR, Mohr RT, Koh TS, Gamble JK, Wu X, Savage DE, Lagally MG, et al. Coherent quantum oscillations and echo measurements of a Si charge qubit. *Phys Rev B*. 2013;88(7):Article 075416.
52. MacQuarrie E, Neyens SF, Dodson J, Corrigan J, Thorgrimsson B, Holman N, Palma M, Edge L, Friesen M, Coppersmith S, et al. Progress toward a capacitively mediated CNOT between two charge qubits in Si/SiGe. *npj Quantum Inf*. 2020;6(1):81.
53. Liles SD, Halverson DJ, Wang Z, Shamim A, Eggli RS, Jin IK, Hillier J, Kumar K, Vorreiter I, Rendell MJ, et al. A singlet-triplet hole-spin qubit in MOS silicon. *Nat Commun*. 2024;15(1):7690.
54. Zhang X, Morozova E, Rimbach-Russ M, Jirovec D, Hsiao TK, Fariña PC, Wang CA, Oosterhout SD, Sammak A, Scappucci G, et al. Universal control of four singlet–triplet qubits. *Nat Nanotechnol*. 2025;20:209–215.
55. Penthorn NE, Schoenfield JS, Rooney JD, Edge LF, Jiang H. Two-axis quantum control of a fast valley qubit in silicon. *npj Quantum Inf*. 2019;5(1):94.
56. Acuna E, Broz JD, Shyamsundar K, Mei AB, Feeney CP, Smetanka V, Davis T, Lee K, Choi MD, Boyd B, et al. Coherent control of a triangular exchange-only spin qubit. *Phys Rev Appl*. 2024;22(3):Article 044057.
57. Ha W, Ha SD, Choi MD, Tang Y, Schmitz AE, Levendorf MP, Lee K, Chappell JM, Adams TS, Hulbert DR, et al. A flexible design platform for Si/SiGe exchange-only qubits with low disorder. *Nano Lett*. 2022;22:1443–1448.
58. Yu CX, Zihlmann S, Abadillo-Uriel JC, Michal VP, Rambal N, Niebojewski H, Bedecarrats T, Vinet M, Dumur É, Filippone M, et al. Strong coupling between a photon and a hole spin in silicon. *Nat Nanotechnol*. 2023;18(7):741–746.
59. Scappucci G, Kloeffel C, Zwanenburg FA, Loss D, Myronov M, Zhang JJ, De Franceschi S, Katsaros G, Veldhorst M. The germanium quantum information route. *Nat Rev Mater*. 2021;6(10):926–943.
60. Fang Y, Philippopoulos P, Culcer D, Coish W, Chesi S. Recent advances in hole-spin qubits. *Mater Quantum Technol*. 2023;3(1):Article 012003.
61. Morello A, Pla JJ, Bertet P, Jamieson DN. Donor spins in silicon for quantum technologies. *Adv Quantum Technol*. 2020;3(11):2000005.
62. McCallum JC, Johnson BC, Botzem T. Donor-based qubits for quantum computing in silicon. *Appl Phys Rev*. 2021;8(3):Article 031314.
63. Hanson R, Kouwenhoven LP, Petta JR, Tarucha S, Vandersypen LMK. Spins in few electron quantum dots. *Rev Mod Phys*. 2007;79(4):1217–1265.
64. Zwanenburg FA, Dzurak AS, Morello A, Simmons MY, Hollenberg LCL, Klimeck G, Rogge S, Coppersmith SN, Eriksson MA. Silicon quantum electronics. *Rev Mod Phys*. 2013;85(3):961–1019.
65. Dresselhaus G, Kip AF, Kittel C. Cyclotron resonance of electrons and holes in silicon and germanium crystals. *Phys Rev*. 1955;98:368–384.
66. Bychkov YA, Rashba EI. Oscillatory effects and the magnetic susceptibility of carriers in inversion layers. *J Phys C Solid State Phys*. 1984;17(33):6039.
67. Zawadzki W, Pfeffer P. Spin splitting of subband energies due to inversion asymmetry in semiconductor heterostructures. *Semicond Sci Technol*. 2003;19(1):R1.
68. Golovach VN, Khaetskii A, Loss D. Phonon-induced decay of the electron spin in quantum dots. *Phys Rev Lett*. 2004;93:Article 016601.
69. Tokura Y, Obata T, Hatano T, and Tarucha S. Electron-spin manipulation in quantum dot systems. In: *Electron spin resonance and related phenomena in low-dimensional structures*. Berlin, Heidelberg: Springer Berlin Heidelberg; 2009. p. 15–34.
70. Hu X, Das SS. Charge-fluctuation-induced dephasing of exchange-coupled spin qubits. *Phys Rev Lett*. 2006;96(10):Article 100501.
71. Scarlino P, Ungerer JH, van Woerkom DJ, Mancini M, Stano P, Müller C, Landig AJ, Koski JV, Reichl C, Wegscheider W, et al. In situ tuning of the electric-dipole strength of a double-dot charge qubit: Charge-noise protection and ultrastrong coupling. *Phys Rev X*. 2022;12(3):Article 031004.
72. Tokura Y, van der Wiel WG, Obata T, Tarucha S. Coherent Single Electron Spin Control in a Slanting Zeeman Field. *Phys Rev Lett*. 2006;96:Article 047202.
73. Pioro-Ladriere M, Obata T, Tokura Y, Shin YS, Kubo T, Yoshida K, Taniyama T, Tarucha S. Electrically driven single-electron spin resonance in a slanting Zeeman field. *Nat Phys*. 2008;4(10):776-779.

74. Tosi G, Mohiyaddin FA, Schmitt V, Tenberg S, Rahman R, Klimeck G, Morello A. Silicon quantum processor with robust long-distance qubit couplings. *Nat Commun*. 2017;8(1):450.
75. Wu Y, Yang X. Strong-coupling theory of periodically driven two-level systems. *Phys Rev Lett*. 2007;98(1):Article 013601.
76. Meunier T, Calado VE, Vandersypen LMK. Efficient controlled-phase gate for single-spin qubits in quantum dots. *Phys Rev B*. 2011;83(12):Article 121403.
77. Duan LM, Guo GC. Reducing decoherence in quantum-computer memory with all quantum bits coupling to the same environment. *Phys Rev A*. 1998;57(2):737–741.
78. Astafiev O, Pashkin YA, Nakamura Y, Yamamoto T, Tsai JS. Quantum noise in the Josephson charge qubit. *Phys Rev Lett*. 2004;93(26):Article 267007.
79. Huang P. Dephasing of exchange-coupled spins in quantum dots for quantum computing. *Adv Quantum Technol*. 2021;4(11):2100018.
80. Amasha S, MacLean K, Radu IP, Zumbühl DM, Kastner MA, Hanson MP, Gossard AC. Electrical control of spin relaxation in a quantum dot. *Phys Rev Lett*. 2008;100:Article 046803.
81. Xiao M, House MG, Jiang HW. Measurement of the spin relaxation time of single electrons in a silicon metal-oxide-semiconductor-based quantum dot. *Phys Rev Lett*. 2010;104:Article 096801.
82. Yang CH, Rossi A, Ruskov R, Lai NS, Mohiyaddin FA, Lee S, Tahan C, Klimeck G, Morello A, Dzurak AS. Spin-valley lifetimes in a silicon quantum dot with tunable valley splitting. *Nat Commun*. 2013;4:2069.
83. Zhang X, Hu RZ, Li HO, Jing FM, Zhou Y, Ma RL, Ni M, Luo G, Cao G, Wang GL, et al. Giant anisotropy of spin relaxation and spin-valley mixing in a silicon quantum dot. *Phys Rev Lett*. 2020;124:Article 257701.
84. Huang P, Hu X. Electron spin relaxation due to charge noise. *Phys Rev B*. 2014;89:Article 195302.
85. Huang P, Hu X. Spin relaxation in a Si quantum dot due to spin-valley mixing. *Phys Rev B*. 2014;90(23):Article 235315.
86. Huang P, Hu X. Fast spin-valley-based quantum gates in Si with micromagnets. *npj Quantum Inf*. 2021;7:162.
87. Veldhorst M, Hwang JCC, Yang CH, Leenstra AW, Ronde BD, Dehollain JP, Muhonen JT, Hudson FE, Itoh KM, Morello A, et al. An addressable quantum dot qubit with fault-tolerant control-fidelity. *Nat Nanotechnol*. 2014;9(12):981–985.
88. Tyryshkin AM, Lyon SA, Astashkin AV, Raitsimring AM. Electron spin relaxation times of phosphorus donors in silicon. *Phys Rev B*. 2003;68:Article 193207.
89. Tyryshkin AM, Tojo S, Morton JJL, Riemann H, Abrosimov NV, Becker P, Pohl HJ, Schenkel T, Thewalt MLW, Itoh KM, et al. Electron spin coherence exceeding seconds in high-purity silicon. *Nat Mater*. 2012;11:143–147.
90. Khaetskii AV, Nazarov YV. Spin-flip transitions between Zeeman sublevels in semiconductor quantum dots. *Phys Rev B*. 2001;64(12):Article 125316.
91. Tahan C, Joynt R. Relaxation of excited spin, orbital, and valley qubit states in ideal silicon quantum dots. *Phys Rev B*. 2014;89(7):Article 075302.
92. Hosseinkhani A, Burkard G. Relaxation of single-electron spin qubits in silicon in the presence of interface steps. *Phys Rev B*. 2021;104(8):Article 085309.
93. Borjans F, Zajac DM, Hazard TM, Petta JR. Single-spin relaxation in a synthetic spin-orbit field. *Phys Rev Appl*. 2019;11:Article 044063.
94. de Sousa R, Das Sarma S. Theory of nuclear-induced spectral diffusion: Spin decoherence of phosphorus donors in Si and GaAs quantum dots. *Phys Rev B*. 2003;68:Article 115322.
95. Coish WA, Loss D. Singlet-triplet decoherence due to nuclear spins in a double quantum dot. *Phys Rev B*. 2005;72:Article 125337.
96. Yao W, Liu RB, Sham LJ. Restoring coherence lost to a slow interacting mesoscopic spin bath. *Phys Rev Lett*. 2007;98:Article 077602.
97. Cywinski L, Witzel WM, Das Sarma S. Pure quantum dephasing of a solid-state electron spin qubit in a large nuclear spin bath coupled by long-range hyperfine-mediated interactions. *Phys Rev B*. 2009;79:Article 245314.
98. Dobrovitski VV, Feiguin AE, Hanson R, Awschalom DD. Decay of Rabi oscillations by dipolar-coupled dynamical spin environments. *Phys Rev Lett*. 2009;102:Article 237601.
99. Witzel WM, Carroll MS, Cywinski L, Das SS. Quantum decoherence of the central spin in a sparse system of dipolar coupled spins. *Phys Rev B*. 2012;86:Article 035452.
100. Barnes E, Cywinski L, Das SS. Nonperturbative master equation solution of central spin dephasing dynamics. *Phys Rev Lett*. 2012;109:Article 140403.
101. Maune BM, Borselli MG, Huang B, Ladd TD, Deelman PW, Holabird KS, Kiselev AA, Alvarado-Rodriguez I, Ross RS, Schmitz AE, et al. Coherent singlet-triplet oscillations in a silicon-based double quantum dot. *Nature*. 2012;481:344–347.
102. Veldhorst M, Yang CH, Hwang JCC, Huang W, Dehollain JP, Muhonen JT, Simmons S, Laucht A, Hudson FE, Itoh KM, et al. A two-qubit logic gate in silicon. *Nature*. 2015;526(7573):410–414.
103. Yoneda J, Takeda K, Otsuka T, Nakajima T, Delbecq MR, Allison G, Honda T, Kodera T, Oda S, Hoshi Y, et al. A quantum-dot spin qubit with coherence limited by charge noise and fidelity higher than 99.9%. *Nat Nanotechnol*. 2018;13:102–106.
104. Huang P, Hu X. Spin manipulation and decoherence in a quantum dot mediated by a synthetic spin–orbit coupling of broken T-symmetry. *New J Phys*. 2021;24:Article 013002.
105. Bertrand B, Flentje H, Takada S, Yamamoto M, Tarucha S, Ludwig A, Wieck AD, Bäuerle C, Meunier T. Quantum manipulation of two-electron spin states in isolated double quantum dots. *Phys Rev Lett*. 2015;115(9):Article 096801.
106. Reed MD, Maune BM, Andrews RW, Borselli MG, Eng K, Jura MP, Kiselev AA, Ladd TD, Merkel ST, Milosavljevic I, et al. Reduced sensitivity to charge noise in semiconductor spin qubits via symmetric operation. *Phys Rev Lett*. 2016;116(11):Article 110402.
107. Martins F, Malinowski FK, Nissen PD, Barnes E, Fallahi S, Gardner GC, Manfra MJ, Marcus CM, Kuemmeth F. Noise suppression using symmetric exchange gates in spin qubits. *Phys Rev Lett*. 2016;116(11):Article 116801.
108. Nichol JM, Orona LA, Harvey SP, Fallahi S, Gardner GC, Manfra MJ, Yacoby A. High-fidelity entangling gate for double-quantum-dot spin qubits. *npj Quantum Inf*. 2017;3:3.
109. Vahapoglu E, Slack-Smith JP, Leon RCC, Lim WH, Hudson FE, Day T, Tanttu T, Yang CH, Laucht A, Dzurak AS, et al. Single-electron spin resonance in a nanoelectronic device using a global field. *Sci Adv*. 2021;7(33):eabg9158.
110. Vahapoglu E, Slack-Smith JP, Leon RCC, Lim WH, Hudson FE, Day T, Cifuentes JD, Tanttu T, Yang CH, Saraiva A, et al.

Coherent control of electron spin qubits in silicon using a global field. *npj Quantum Inf*. 2022;8:126.
111. Gullans MJ, Petta JR. Protocol for a resonantly driven three-qubit Toffoli gate with silicon spin qubits. *Phys Rev B*. 2019;100:Article 085419.
112. Takeda K, Noiri A, Nakajima T, Kobayashi T, Tarucha S. Quantum error correction with silicon spin qubits. *Nature*. 2022;608:682–686.
113. Loss D, DiVincenzo DP. Quantum computation with quantum dots. *Phys Rev A*. 1998;57(1):120–126.
114. Itoh KM, Watanabe H. Isotope engineering of silicon and diamond for quantum computing and sensing applications. *MRS Commun*. 2014;4:143–157.
115. Scappucci G, Taylor P, Williams J, Ginley T, Law S. Crystalline materials for quantum computing: Semiconductor heterostructures and topological insulators exemplars. *MRS Bull*. 2021;46:596–606.
116. Simmons CB, Thalakulam M, Shaji N, Klein LJ, Qin H, Blick RH, Savage DE, Lagally MG, Coppersmith SN, Eriksson MA. Single-electron quantum dot in Si/SiGe with integrated charge sensing. *Appl Phys Lett*. 2007;91:Article 213103.
117. Shaji N, Simmons CB, Thalakulam M, Klein LJ, Qin H, Luo H, Savage DE, Lagally MG, Rimberg AJ, Joynt R, et al. Spin blockade and lifetime-enhanced transport in a few-electron Si/SiGe double quantum dot. *Nat Phys*. 2008;4:540–544.
118. Kawakami E, Scarlino P, Ward DR, Braakman FR, Savage DE, Lagally MG, Friesen M, Coppersmith SN, Eriksson MA, Vandersypen LMK. Electrical control of a long-lived spin qubit in a Si/SiGe quantum dot. *Nat Nanotechnol*. 2014;9:666–670.
119. Degli Esposti D, Stehouwer LEA, Gül Ö, Samkharadze N, Déprez C, Meyer M, Meijer IN, Tryputen L, Karwal S, Botifoll M, et al. Low disorder and high valley splitting in silicon. *npj Quantum Inf*. 2024;10:32.
120. Phillips JC. Band structure of silicon, germanium, and related semiconductors. *Phys Rev*. 1962;125(6):1931–1936.
121. Losert MP, Eriksson MA, Joynt R, Rahman R, Scappucci G, Coppersmith SN, Friesen M. Practical strategies for enhancing the valley splitting in Si/SiGe quantum wells. *Phys Rev B*. 2023;108(12):Article 125405.
122. Camenzind TN, Elsayed A, Mohiyaddin FA, Li R, Kubicek S, Jussot J, Van Dorpe P, Govoreanu B, Radu I, Zumbühl DM. High mobility SiMOSFETs fabricated in a full 300 mm CMOS process. *Mater Quantum Technol*. 2021;1:Article 041001.
123. Sabbagh D, Thomas N, Torres J, Pillarisetty R, Amin P, George H, Singh K, Budrevich A, Robinson M, Merrill D, et al. Quantum transport properties of industrial $^{28}Si/^{28}SiO_2$. *Phys Rev Appl*. 2019;12(1):Article 014013.
124. Bersano F, De Palma F, Oppliger F, Braakman F, Radu I, Scarlino P, Poggio M, Ionescu AM. Multi-gate FD-SOI single electron transistor for hybrid SET-MOSFET quantum computing. In: *ESSCIRC 2022- IEEE 48th European Solid State Circuits Conference (ESSCIRC)*. Milan (Italy): IEEE; 2022. p. 49–52.
125. Kuhlmann AV, Deshpande V, Camenzind LC, Zumbühl DM, Fuhrer A. Ambipolar quantum dots in undoped silicon fin field-effect transistors. *Appl Phys Lett*. 2018;113:Article 122107.
126. Rossi A, Tanttu T, Hudson FE, Sun Y, Möttönen M, Dzurak AS. Silicon metal-oxidesemiconductor quantum dots for single-electron pumping. *J Vis Exp*. 2015;100:Article e52852.
127. Lai NS, Lim WH, Yang CH, Zwanenburg FA, Coish WA, Qassemi F, Morello A, Dzurak AS. Pauli spin blockade in a highly tunable silicon double quantum dot. *Sci Rep*. 2011;1:110.
128. Zajac DM, Hazard TM, Mi X, Nielsen E, Petta JR. Scalable gate architecture for a one-dimensional array of semiconductor spin qubits. *Phys Rev Appl*. 2016;6(5):Article 054013.
129. Spruijtenburg PC, Amitonov SV, vander Wiel WG, Zwanenburg FA. A fabrication guide for planar silicon quantum dot heterostructures. *Nanotechnology*. 2018;29:Article 143001.
130. Geyer S, Camenzind LC, Czornomaz L, Deshpande V, Fuhrer A, Warburton RJ, Zumbühl DM, Kuhlmann AV. Self-aligned gates for scalable silicon quantum computing. *Appl Phys Lett*. 2021;118:Article 104004.
131. Rochette S, Rudolph M, Roy AM, Curry MJ, Eyck GAT, Manginell RP, Wendt JR, Pluym T, Carr SM, Ward DR, et al. Quantum dots with split enhancement gate tunnel barrier control. *Appl Phys Lett*. 2019;114:Article 083101.
132. Thorbeck T, Zimmerman NM. Formation of strain-induced quantum dots in gated semiconductor nanostructures. *AIP Adv*. 2015;5:Article 087107.
133. Stuyck NID, Li R, Godfrin C, Elsayed A, Kubicek S, Jussot J, Chan BT, Mohiyaddin FA, Shehata M, Simion G, et al. Uniform spin qubit devices with tunable coupling in an all-silicon 300 mm integrated process. In: *2021 Symposium on VLSI circuits*. Kyoto (Japan): IEEE; 2021. p. 1–2.
134. Maurand R, Jehl X, Kotekar-Patil D, Corna A, Bohuslavskyi H, Laviéville R, Hutin L, Barraud S, Vinet M, Sanquer M, et al. A CMOS silicon spin qubit. *Nat Commun*. 2016;7:13575.
135. Bédécarrats T, Paz BC, Diaz BM, Niebojewski H, Bertrand B, Rambal N, Comboroure C, Sarrazin A, Boulard F, Guyez E, et al. A new FDSOI spin qubit platform with 40nm effective control pitch. In: *2021 IEEE international electron devices meeting (IEDM)*. San Francisco (CA): IEEE; 2021. p. 1–4.
136. Zwerver AMJ, Krähenmann T, Watson TF, Lampert L, George HC, Pillarisetty R, Bojarski SA, Amin P, Amitonov SV, Boter JM, et al. Qubits made by advanced semiconductor manufacturing. *Nat Electron*. 2022;5:184–190.
137. Pillarisetty R, Watson T, Mueller B, Henry E, George H, Bojarski S, Lampert L, Luthi F, Kotlyar R, Zietz O, et al. Si MOS and Si/SiGe quantum well spin qubit platforms for scalable quantum computing. In: *2021 IEEE International Electron Devices Meeting (IEDM)*. San Francisco (CA): IEEE; 2021. p. 14.1.1–14.1.4.
138. Elzerman JM, Hanson R, Willems van Beveren LH, Witkamp B, Vandersypen LMK, Kouwenhoven LP. Single-shot read-out of an individual electron spin in a quantum dot. *Nature*. 2004;430:431–435.
139. Johnson AC, Petta JR, Marcus CM, Hanson MP, Gossard AC. Singlet-triplet spin blockade and charge sensing in a few-electron double quantum dot. *Phys Rev B*. 2005;72(16):Article 165308.
140. Keith D, Gorman SK, Kranz L, He Y, Keizer JG, Broome MA, Simmons MY. Benchmarking high fidelity single-shot readout of semiconductor qubits. *New J Phys*. 2019;21:Article 063011.
141. Mills A, Guinn C, Feldman M, Sigillito A, Gullans M, Rakher M, Kerckhoff J, Jackson C, Petta J. High-fidelity state preparation, quantum control, and readout of an isotopically

enriched silicon spin qubit. *Phys Rev Appl*. 2022;18(6): Article 064028.
142. Oakes GA, Ciriano-Tejel VN, Wise DF, Fogarty MA, Lundberg T, Lainé C, Schaal S, Martins F, Ibberson DJ, Hutin L, et al. Fast high-fidelity single-shot readout of spins in silicon using a single-electron box. *Phys Rev X*. 2023;13(1):Article 011023.
143. Baart TA, Shafiei M, Fujita T, Reichl C, Wegscheider W, Vandersypen LMK. Single-spin CCD. *Nat Nanotechnol*. 2016;11:330–334.
144. Fujita T, Baart TA, Reichl C, Wegscheider W, Vandersypen LMK. Coherent shuttle of electron-spin states. *npj Quantum Inf*. 2017;3:22.
145. Borjans F, Mi X, Petta J. Spin digitizer for high-fidelity readout of a cavity-coupled silicon triple quantum dot. *Phys Rev Appl*. 2021;15(4):Article 044052.
146. Connors EJ, Nelson J, Nichol JM. Rapid high-fidelity spin-state readout in Si/Si-Ge quantum dots via rf reflectometry. *Phys Rev Appl*. 2020;13(2):Article 024019.
147. Noiri A, Takeda K, Yoneda J, Nakajima T, Kodera T, Tarucha S. Radio-frequency detected fast charge sensing in undoped silicon quantum dots. *Nano Lett*. 2020;20:947–952.
148. Takeda K, Noiri A, Nakajima T, Camenzind LC, Kobayashi T, Sammak A, Scappucci G, Tarucha S. Rapid single-shot parity spin readout in a silicon double quantum dot with fidelity exceeding 99%. *npj Quantum Inf*. 2024;10:22.
149. Blumoff JZ, Pan AS, Keating TE, Andrews RW, Barnes DW, Brecht TL, Croke ET, Euliss LE, Fast JA, Jackson CA, et al. Fast and high-fidelity state preparation and measurement in triple-quantum-dot spin qubits. *PRX Quantum*. 2022;3(1):Article 010352.
150. Seedhouse AE, Tanttu T, Leon RC, Zhao R, Tan KY, Hensen B, Hudson FE, Itoh KM, Yoneda J, Yang CH, et al. Pauli blockade in silicon quantum dots with spin-orbit control. *PRX Quantum*. 2021;2(1):Article 010303.
151. Yoneda J, Takeda K, Noiri A, Nakajima T, Li S, Kamioka J, Kodera T, Tarucha S. Quantum non-demolition readout of an electron spin in silicon. *Nat Commun*. 2020;11:1144.
152. Xue X, D'Anjou B, Watson TF, Ward DR, Savage DE, Lagally MG, Friesen M, Coppersmith SN, Eriksson MA, Coish WA, et al. Repetitive quantum nondemolition measurement and soft decoding of a silicon spin qubit. *Phys Rev X*. 2020;10(2):Article 021006.
153. Koppens FHL, Buizert C, Tielrooij KJ, Vink IT, Nowack KC, Meunier T, Kouwenhoven LP, Vandersypen LMK. Driven coherent oscillations of a single electron spin in a quantum dot. *Nature*. 2006;442:766–771.
154. Nadj-Perge S, Frolov SM, Bakkers EPAM, Kouwenhoven LP. Spin-orbit qubit in a semiconductor nanowire. *Nature*. 2010;468:1084–1087.
155. Petta JR, Johnson AC, Taylor JM, Laird EA, Yacoby A, Lukin MD, Marcus CM, Hanson MP, Gossard AC. Coherent manipulation of coupled electron spins in semiconductor quantum dots. *Science*. 2005;309(5744):2180–2184.
156. Foletti S, Bluhm H, Mahalu D, Umansky V, Yacoby A. Universal quantum control of two electron spin quantum bits using dynamic nuclear polarization. *Nat Phys*. 2009;5:903–908.
157. Fogarty MA, Chan KW, Hensen B, Huang W, Tanttu T, Yang CH, Laucht A, Veldhorst M, Hudson FE, Itoh KM, et al. Integrated silicon qubit platform with single-spin addressability, exchange control and single-shot singlet-triplet readout. *Nat Commun*. 2018;9:4370.
158. Jock RM, Jacobson NT, Harvey-Collard P, Mounce AM, Srinivasa V, Ward DR, Anderson J, Manginell R, Wendt JR, Rudolph M, et al. A silicon metal-oxide-semiconductor electron spin-orbit qubit. *Nat Commun*. 2018;9:1768.
159. Hayashi T, Fujisawa T, Cheong HD, Jeong YH, Hirayama Y. Coherent manipulation of electronic states in a double quantum dot. *Phys Rev Lett*. 2003;91(22): Article 226804.
160. Petta JR, Johnson AC, Marcus CM, Hanson MP, Gossard AC. Manipulation of a single charge in a double quantum dot. *Phys Rev Lett*. 2004;93(18):Article 186802.
161. Petersson KD, Petta JR, Lu H, Gossard AC. Quantum coherence in a one-electron semiconductor charge qubit. *Phys Rev Lett*. 2010;105(24):Article 246804.
162. Cao G, Li HO, Tu T, Wang L, Zhou C, Xiao M, Guo GC, Jiang HW, Guo GP. Ultrafast universal quantum control of a quantum-dot charge qubit using Landau-Zener-Stückelberg interference. *Nat Commun*. 2013;4:1401.
163. Shi Z, Simmons CB, Prance JR, Gamble JK, Koh TS, Shim YP, Hu X, Savage DE, Lagally MG, Eriksson MA, et al. Fast hybrid silicon double-quantum-dot qubit. *Phys Rev Lett*. 2012;108(14):Article 140503.
164. Koh TS, Gamble JK, Friesen M, Eriksson MA, Coppersmith SN. Pulse-gated quantum dot hybrid qubit. *Phys Rev Lett*. 2012;109(25):Article 250503.
165. Shi Z, Simmons CB, Ward DR, Prance JR, Wu X, Koh TS, Gamble JK, Savage DE, Lagally MG, Friesen M, et al. Fast coherent manipulation of three-electron states in a double quantum dot. *Nat Commun*. 2014;5:3020.
166. Kim D, Ward DR, Simmons CB, Savage DE, Lagally MG, Friesen M, Coppersmith SN, Eriksson MA. High-fidelity resonant gating of a silicon-based quantum dot hybrid qubit. *npj Quantum Inf*. 2015;1:15004.
167. Malinowski FK, Martins F, Nissen PD, Fallahi S, Gardner GC, Manfra MJ, Marcus CM, Kuemmeth F. Symmetric operation of the resonant exchange qubit. *Phys Rev B*. 2017;96(4): Article 045443.
168. Sala A, Danon J. Exchange-only singlet-only spin qubit. *Phys Rev B*. 2017;95(24):Article 241303.
169. Laird EA, Taylor JM, DiVincenzo DP, Marcus CM, Hanson MP, Gossard AC. Coherent spin manipulation in an exchange-only qubit. *Phys Rev B*. 2010;82(7):Article 075403.
170. Russ M, Petta JR, Burkard G. Quadrupolar exchange-only spin qubit. *Phys Rev Lett*. 2018;121(17):Article 177701.
171. Veldhorst M, Ruskov R, Yang CH, Hwang JCC, Hudson FE, Flatté ME, Tahan C, Itoh KM, Morello A, Dzurak AS. Spin-orbit coupling and operation of multivalley spin qubits. *Phys Rev B*. 2015;92(20):Article 201401.
172. Gilbert W, Tanttu T, Lim WH, Feng M, Huang JY, Cifuentes JD, Serrano S, Mai PY, Leon RCC, Escott CC, et al. On-demand electrical control of spin qubits. *Nat Nanotechnol*. 2023;18:131–136.
173. Fowler AG, Mariantoni M, Martinis JM, Cleland AN. Surface codes: Towards practical large-scale quantum computation. *Phys Rev A*. 2012;86(3):Article 032324.
174. Zou J, Bosco S, Loss D. Spatially correlated classical and quantum noise in driven qubits. *npj Quantum Inf*. 2024;10(1):46.
175. Huang W, Yang CH, Chan KW, Tanttu T, Hensen B, Leon RCC, Fogarty MA, Hwang JCC, Hudson FE, Itoh KM, et al. Fidelity benchmarks for two-qubit gates in silicon. *Nature*. 2019;569:532–536.

176. Hensen B, Wei Huang W, Yang CH, Wai Chan K, Yoneda J, Tanttu T, Hudson FE, Laucht A, Itoh KM, Ladd TD, et al. A silicon quantum-dot-coupled nuclear spin qubit. *Nat Nanotechnol*. 2020;15:13–17.
177. Boter JM, Xue X, Krähenmann T, Watson TF, Premakumar VN, Ward DR, Savage DE, Lagally MG, Friesen M, Coppersmith SN, et al. Spatial noise correlations in a Si/SiGe two qubit device from bell state coherences. *Phys Rev B*. 2020;101(23):Article 235133.
178. Rojas-Arias J, Noiri A, Stano P, Nakajima T, Yoneda J, Takeda K, Kobayashi T, Sammak A, Scappucci G, Loss D, et al. Spatial noise correlations beyond nearest neighbors in ^{28}Si/Si-Ge spin qubits. *Phys Rev Appl*. 2023;20(5): Article 054024.
179. Kratochwil B, Koski JV, Landig AJ, Scarlino P, Abadillo-Uriel JC, Reichl C, Coppersmith SN, Wegscheider W, Friesen M, Wallraff A, et al. Charge qubit in a triple quantum dot with tunable coherence. *Phys Rev Res*. 2021;3(1): Article 013171.
180. Xue X, Watson TF, Helsen J, Ward DR, Savage DE, Lagally MG, Coppersmith SN, Eriksson MA, Wehner S, Vandersypen LMK. Benchmarking gate fidelities in a Si/SiGe two-qubit device. *Phys Rev X*. 2019;9(2):Article 021011.
181. Rimbach-Russ M, Philips SGJ, Xue X, Vandersypen LMK. Simple framework for systematic high-fidelity gate operations. *Quantum Sci Technol*. 2023;8(4):Article 045025.
182. Takeda K, Yoneda J, Otsuka T, Nakajima T, Delbecq MR, Allison G, Hoshi Y, Usami N, Itoh KM, Oda S, et al. Optimized electrical control of a Si/SiGe spin qubit in the presence of an induced frequency shift. *npj Quantum Inf*. 2018;4:54.
183. Watson TF, Philips SGJ, Kawakami E, Ward DR, Scarlino P, Veldhorst M, Savage DE, Lagally MG, Friesen M, Coppersmith SN, et al. A programmable two-qubit quantum processor in silicon. *Nature*. 2018;555(7698):633–637.
184. Undseth B, Pietx-Casas O, Raymenants E, Mehmandoost M, Mądzik MT, Philips SGJ, de Snoo SL, Michalak DJ, Amitonov SV, Tryputen L, et al. Hotter is easier: Unexpected temperature dependence of spin qubit frequencies. *Phys Rev X* 2023;13(4):Article 041015.
185. Petit L, Russ M, Eenink GHGJ, Lawrie WIL, Clarke JS, Vandersypen LMK, Veldhorst M. Design and integration of single-qubit rotations and two-qubit gates in silicon above one kelvin. *Commun Mater*. 2022;3:82.
186. Nowack KC, Shafiei M, Laforest M, Prawiroatmodjo GEDK, Schreiber LR, Reichl C, Wegscheider W, Vandersypen LMK. Single-shot correlations and two-qubit gate of solid state spins. *Science*. 2011;333:1269–1272.
187. Zajac DM, Sigillito AJ, Russ M, Borjans F, Taylor JM, Burkard G, Petta JR. Resonantly driven CNOT gate for electron spins. *Science*. 2018;359(6374):439–442.
188. Kalra R, Laucht A, Hill CD, Morello A. Robust two-qubit gates for donors in silicon controlled by hyperfine interactions. *Phys Rev X*. 2014;4(2):Article 021044.
189. Vandersypen LMK, Chuang IL. NMR techniques for quantum control and computation. *Rev Mod Phys*. 2005;76(4):1037–1069.
190. Tanttu T, Hensen B, Chan KW, Yang CH, Huang WW, Fogarty M, Hudson F, Itoh K, Culcer D, Laucht A, et al. Controlling spin-orbit interactions in silicon quantum dots using magnetic field direction. *Phys Rev X*. 2019;9(2): Article 021028.
191. Burkard G, Loss D, DiVincenzo DP, Smolin JA. Physical optimization of quantum error correction circuits. *Phys Rev B*. 1999;60(16):11404–11416.
192. Russ M, Zajac DM, Sigillito AJ, Borjans F, Taylor JM, Petta JR, Burkard G. High-fidelity quantum gates in Si/SiGe double quantum dots. *Phys Rev B*. 2018;97(8):Article 085421.
193. Wu YH, Camenzind LC, Noiri A, Takeda K, Nakajima T, Kobayashi T, Chang CY, Sammak A, Scappucci G, Goan HS, et al. Hamiltonian phase error in resonantly driven CNOT gate above the fault-tolerant threshold. *npj Quantum Inf*. 2024;10(1):8.
194. Hansen I, Seedhouse AE, Chan KW, Hudson FE, Itoh KM, Laucht A, Saraiva A, Yang CH, Dzurak AS. Implementation of an advanced dressing protocol for global qubit control in silicon. *Appl Phys Rev*. 2022;9(3):Article 031409.
195. Vandersypen LMK, Bluhm H, Clarke JS, Dzurak AS, Ishihara R, Morello A, Reilly DJ, Schreiber LR, Veldhorst M. Interfacing spin qubits in quantum dots and donors—Hot, dense, and coherent. *npj Quantum Inf*. 2017;3(1):34.
196. Boter JM, Dehollain JP, van Dijk JP, Xu Y, Hensgens T, Versluis R, Naus HW, Clarke JS, Veldhorst M, Sebastiano F, et al. Spiderweb Array: A sparse spin-qubit array. *Phys Rev Appl*. 2022;18(2):Article 024053.
197. Veldhorst M, Eenink HGJ, Yang CH, Dzurak AS. Silicon CMOS architecture for a spin based quantum computer. *Nat Commun*. 2017;8(1):1766.
198. Li R, Petit L, Franke DP, Dehollain JP, Helsen J, Steudtner M, Thomas NK, Yoscovits ZR, Singh KJ, Wehner S, et al. A crossbar network for silicon quantum dot qubits. *Sci Adv*. 2018;4:eaar3960.
199. Unseld FK, Meyer M, Mądzik MT, Borsoi F, de Snoo SL, Amitonov SV, Sammak A, Scappucci G, Veldhorst M, Vandersypen LMK. A 2D quantum dot array in planar 28Si/SiGe. *Appl Phys Lett*. 2023;123(8):Article 084002.
200. Borsoi F, Hendrickx NW, John V, Meyer M, Motz S, van Riggelen F, Sammak A, de Snoo SL, Scappucci G, Veldhorst M. Shared control of a 16 semiconductor quantum dot crossbar array. *Nat Nanotechnol*. 2024;19(1):21–27.
201. John V, Yu CX, van Straaten B, Rodríguez-Mena EA, Rodríguez M, Oosterhout S, Stehouwer LEA, Scappucci G, Bosco S, Rimbach-Russ M, et al. A two-dimensional 10-qubit array in germanium with robust and localised qubit control. arXiv. 2025. https://doi.org/10.48550/arXiv.2412.16044
202. Hendrickx NW, Lawrie WIL, Petit L, Sammak A, Scappucci G, Veldhorst M. A single-hole spin qubit. *Nat Commun*. 2020;11(1):3478.
203. Van Riggelen F, Lawrie WIL, Russ M, Hendrickx NW, Sammak A, Rispler M, Terhal BM, Scappucci G, Veldhorst M. Phase flip code with semiconductor spin qubits. *npj Quantum Inf* 2022;8(1):124.
204. Kane BE. A silicon-based nuclear spin quantum computer. *Nature*. 1998;393(6681):133–137.
205. Hansen I, Seedhouse AE, Saraiva A, Laucht A, Dzurak AS, Yang CH. Pulse engineering of a global field for robust and universal quantum computation. *Phys Rev A*. 2021;104(6):Article 062415.
206. Moraru D, Udhiarto A, Anwar M, Nowak R, Jablonski R, Hamid E, Tarido JC, Mizuno T, Tabe M. Atom devices based on single dopants in silicon nanostructures. *Nanoscale Res Lett*. 2011;6(1):479.
207. Morello A, Pla JJ, Zwanenburg FA, Chan KW, Tan KY, Huebl H, Mottonen M, Nugroho CD, Yang C,

van Donkelaar JA, et al. Single-shot readout of an electron spin in silicon. *Nature*. 2010;467(7316):687–691.
208. Pla JJ, Tan KY, Dehollain JP, Lim WH, Morton JJ, Jamieson DN, Dzurak AS, Morello A. A single-atom electron spin qubit in silicon. *Nature*. 2012;489(7417):541–545.
209. Tan KY, Chan KW, Möttönen M, Morello A, Yang C, Jv D, Alves A, Pirkkalainen JM, Jamieson DN, Clark RG, et al. Transport spectroscopy of single phosphorus donors in a silicon nanoscale transistor. *Nano Lett*. 2010;10(1):11–15.
210. Singh M, Pacheco JL, Perry D, Garratt E, Ten Eyck G, Bishop NC, Wendt JR, Manginell RP, Dominguez J, Pluym T, et al. Electrostatically defined silicon quantum dots with counted antimony donor implants. *Appl Phys Lett*. 2016;108(6):Article 062101.
211. Rudolph M, Sarabi B, Murray R, Carroll MS, Zimmerman NM. Long-term drift of Si-MOS quantum dots with intentional donor implants. *Sci Rep*. 2019;9(1):7656.
212. Jakob AM, Robson SG, Schmitt V, Mourik V, Posselt M, Spemann D, Johnson BC, Firgau HR, Mayes E, McCallum JC, et al. Deterministic shallow dopant implantation in silicon with detection confidence upper-bound to 99.85% by ion–solid interactions. *Adv Mater*. 2022;34(3):2103235.
213. Simmons MY, Schofield SR, O'Brien JL, Curson NJ, Oberbeck L, Hallam T, Clark RG. Towards the atomic-scale fabrication of a silicon-based solid state quantum computer. *Surf Sci*. 2003;532–535:1209–1218.
214. Rueß FJ, Pok W, Reusch TCG, Butcher MJ, Goh KEJ, Oberbeck L, Scappucci G, Hamilton AR, Simmons MY. Realization of atomically controlled dopant devices in silicon. *Small*. 2007;3(4):563–567.
215. Rueß FJ, Oberbeck L, Simmons MY, Goh KEJ, Hamilton AR, Hallam T, Schofield SR, Curson NJ, Clark RG. Toward atomic-scale device fabrication in silicon using scanning probe microscopy. *Nano Lett*. 2004;4:1969–1973.
216. Randall JN, Owen JHG, Lake J, Saini R, Fuchs E, Mahdavi M, Moheimani SOR, Schaefer BC. Highly parallel scanning tunneling microscope based hydrogen depassivation lithography. *J Vac Sci Technol B*. 2018;36(6):06JL05.
217. Achal R, Rashidi M, Croshaw J, Churchill D, Taucer M, Huff T, Cloutier M, Pitters J, Wolkow RA. Lithography for robust and editable atomic-scale silicon devices and memories. *Nat Commun*. 2018;9(1):2778.
218. Bussmann E, Butera RE, Owen JHG, Randall JN, Rinaldi SM, Baczewski AD, Misra S. Atomic-precision advanced manufacturing for Si quantum computing. *MRS Bull*. 2021;46:607–615.
219. Fuechsle M, Miwa JA, Mahapatra S, Ryu H, Lee S, Warschkow O, Hollenberg LCL, Klimeck G, Simmons MY. A single-atom transistor. *Nat Nanotechnol*. 2012;7(4):242–246.
220. Liu Q, Lei Y, Shao X, Ming F, Xu H, Wang K, Xiao X. Controllable dissociations of PH_3 molecules on Si (001). *Nanotechnology*. 2016;27(13):Article 135704.
221. Wyrick J, Wang X, Namboodiri P, Kashid RV, Fei F, Fox J, Silver R. Enhanced atomic precision fabrication by adsorption of phosphine into engineered dangling bonds on H–Si using STM and DFT. *ACS Nano*. 2022;16(11):19114–19123.
222. Kranz L, Roche S, Gorman SK, Keizer JG, Simmons MY. High-fidelity CNOT gate for donor electron spin qubits in silicon. *Phys Rev Appl*. 2023;19(2):Article 024068.
223. Pla JJ, Tan KY, Dehollain JP, Lim WH, Morton JJL, Zwanenburg FA, Jamieson DN, Dzurak AS, Morello A. High-fidelity readout and control of a nuclear spin qubit in silicon. *Nature*. 2013;496(7445):334–338.
224. Laucht A, Kalra R, Simmons S, Dehollain JP, Muhonen JT, Mohiyaddin FA, Freer S, Hudson FE, Itoh KM, Jamieson DN, et al. A dressed spin qubit in silicon. *Nat Nanotechnol*. 2017;12(1):61–66.
225. DiVincenzo DP, Bacon D, Kempe J, Burkard G, Whaley KB. Universal quantum computation with the exchange interaction. *Nature*. 2000;408(6810):339–342.
226. Broome MA, Watson TF, Keith D, Gorman SK, House MG, Keizer JG, Hile SJ, Baker W, Simmons MY. High-fidelity single-shot singlet-triplet readout of precision-placed donors in silicon. *Phys Rev Lett*. 2017;119(4):Article 046802.
227. Crippa A, Ezzouch R, Aprá A, Amisse A, Laviéville R, Hutin L, Bertrand B, Vinet M, Urdampilleta M, Meunier T, et al. Gate-reflectometry dispersive readout and coherent control of a spin qubit in silicon. *Nat Commun*. 2019;10(1):2776.
228. Vigneau F, Fedele F, Chatterjee A, Reilly D, Kuemmeth F, Gonzalez-Zalba MF, Laird E, Ares N. Probing quantum devices with radio-frequency reflectometry. *Appl Phys Rev*. 2023;10(2):Article 021305.
229. Watson TF, Weber B, House MG, Büch H, Simmons MY. High-fidelity rapid initialization and read-out of an electron spin via the single donor D^- charge state. *Phys Rev Lett*. 2015;115(16):Article 166806.
230. Keith D, House MG, Donnelly MB, Watson TF, Weber B, Simmons MY. Single-shot spin readout in semiconductors near the shot-noise sensitivity limit. *Phys Rev X*. 2019;9(4):Article 041003.
231. Keith D, Chung Y, Kranz L, Thorgrimsson B, Gorman SK, Simmons MY. Ramped measurement technique for robust high-fidelity spin qubit readout. *Sci Adv*. 2022;8:eabq0455.
232. Hogg M, Pakkiam P, Gorman S, Timofeev A, Chung Y, Gulati G, House M, Simmons M. Single-shot readout of multiple donor electron spins with a gate-based sensor. *PRX Quantum*. 2023;4(1):Article 010319.
233. Watson TF, Weber B, Hsueh YL, Hollenberg LCL, Rahman R, Simmons MY. Atomically engineered electron spin lifetimes of 30 s in silicon. *Sci Adv*. 2017;3:Article e1602811.
234. Weber B, Hsueh YL, Watson TF, Li R, Hamilton AR, Hollenberg LCL, Rahman R, Simmons MY. Spin–orbit coupling in silicon for electrons bound to donors. *npj Quantum Inf*. 2018;4:61.
235. Fricke L, Hile SJ, Kranz L, Chung Y, He Y, Pakkiam P, House MG, Keizer JG, Simmons MY. Coherent control of a donor-molecule electron spin qubit in silicon. *Nat Commun*. 2021;12:3323.
236. Wolfowicz G, Tyryshkin AM, George RE, Riemann H, Abrosimov NV, Becker P, Pohl HJ, Thewalt MLW, Lyon SA, Morton JJL. Atomic clock transitions in silicon-based spin qubits. *Nat Nanotechnol*. 2013;8:561–564.
237. Asaad S, Mourik V, Joecker B, Johnson MA, Baczewski AD, Firgau HR, Mądzik MT, Schmitt V, Pla JJ, Hudson FE, et al. Coherent electrical control of a single high-spin nucleus in silicon. *Nature*. 2020;579:205–209.
238. Dehollain JP, Muhonen JT, Blume-Kohout R, Rudinger KM, Gamble JK, Nielsen E, Laucht A, Simmons S, Kalra R, Dzurak AS, et al. Optimization of a solid-state electron spin qubit using gate set tomography. *New J Phys*. 2016;18:Article 103018.

239. Krauth F, Gorman S, He Y, Jones M, Macha P, Kocsis S, Chua C, Voisin B, Rogge S, Rahman R, et al. Flopping-mode electric dipole spin resonance in phosphorus donor qubits in silicon. *Phys Rev Appl*. 2022;17(5):Article 054006.
240. Savytskyy R, Botzem T, de Fuentes IF, Joecker B, Pla JJ, Hudson FE, Itoh KM, Jakob AM, Johnson BC, Jamieson DN, et al. An electrically driven single-atom "flip-flop" qubit. *Sci Adv*. 2023;9(6):eadd9408.
241. Freer S, Simmons S, Laucht A, Muhonen JT, Dehollain JP, Kalra R, Mohiyaddin FA, Hudson FE, Itoh KM, McCallum JC, et al. A single-atom quantum memory in silicon. *Quantum Sci Technol*. 2017;2:Article 015009.
242. Voisin B, Bocquel J, Tankasala A, Usman M, Salfi J, Rahman R, Simmons MY, Hollenberg LCL, Rogge S. Valley interference and spin exchange at the atomic scale in silicon. *Nat Commun*. 2020;11:6124.
243. Mądzik MT, Laucht A, Hudson FE, Jakob AM, Johnson BC, Jamieson DN, Itoh KM, Dzurak AS, Morello A. Conditional quantum operation of two exchange-coupled single-donor spin qubits in a Mos-compatible silicon device. *Nat Commun*. 2021;12:181.
244. Stemp HG, Asaad S, van Blankenstein MR, Vaartjes A, Johnson MAI, Mądzik MT, Heskes AJA, Firgau HR, Su RY, Yang CH, et al. Tomography of entangling two-qubit logic operations in exchange-coupled donor electron spin qubits. *Nat Commun*. 2024;15:8415.
245. Wang Y, Tankasala A, Hollenberg LC, Klimeck G, Simmons MY, Rahman R. Highly tunable exchange in donor qubits in silicon. *npj Quantum Inf*. 2016;2:16008.
246. Hai Y, Li J, Zeng J, Deng X. Universal robust quantum gates by geometric correspondence of noisy quantum dynamics. arXiv. 2023. https://doi.org/10.48550/arXiv.2210.14521
247. Hill CD, Peretz E, Hile SJ, House MG, Fuechsle M, Rogge S, Simmons MY, Hollenberg LCL. A surface code quantum computer in silicon. *Sci Adv*. 2015;1:Article e1500707.
248. He Y, Gorman SK, Keith D, Kranz L, Keizer JG, Simmons MY. A two-qubit gate between phosphorus donor electrons in silicon. *Nature*. 2019;571:371–375.
249. Kranz L, Gorman SK, Thorgrimsson B, He Y, Keith D, Keizer JG, Simmons MY. Exploiting a single-crystal environment to minimize the charge noise on qubits in silicon. *Adv Mater*. 2020;32(40):Article e2003361.
250. Kranz L, Gorman SK, Thorgrimsson B, Monir S, He Y, Keith D, Charde K, Keizer JG, Rahman R, Simmons MY. The use of exchange coupled atom qubits as atomic-scale magnetic field sensors. *Adv Mater*. 2023;35(6):2201625.
251. Hsueh YL, Kranz L, Keith D, Monir S, Chung Y, Gorman SK, Rahman R, Simmons MY. Hyperfine-mediated spin relaxation in donor-atom qubits in silicon. *Phys Rev Res*. 2023;5(2):Article 023043.
252. Monir S, Osika EN, Gorman SK, Thorvaldson I, Hsueh YL, Macha P, Kranz L, Reiner J, Simmons MY, Rahman R. Impact of measurement backaction on nuclear spin qubits in silicon. *Phys Rev B*. 2024;109(3):Article 035157.
253. Jones MT, Monir MS, Krauth FN, Macha P, Hsueh YL, Worrall A, Keizer JG, Kranz L, Gorman SK, Chung Y, et al. Atomic engineering of molecular qubits for high-speed, high-fidelity single qubit gates. *ACS Nano*. 2023;17:22601–22610.
254. Mądzik MT, Ladd TD, Hudson FE, Itoh KM, Jakob AM, Johnson BC, McCallum JC, Jamieson DN, Dzurak AS, Laucht A, et al. Controllable freezing of the nuclear spin bath in a single-atom spin qubit. *Sci Adv*. 2020;6:eaba3442.
255. Vandersypen LMK, Eriksson MA. Quantum computing with semiconductor spins. *Phys Today*. 2019;72:38–45.
256. Schenkel T, Lo CC, Weis CD, Bokor J, Tyryshkin AM, Lyon SA. A spin quantum bit architecture with coupled donors and quantum dots in silicon. arXiv. 2011. https://doi.org/10.48550/arXiv.1110.2228
257. Harvey-Collard P, Jacobson NT, Rudolph M, Dominguez J, Ten Eyck GA, Wendt JR, Pluym T, Gamble JK, Lilly MP, Pioro-Ladrière M, et al. Coherent coupling between a quantum dot and a donor in silicon. *Nat Commun*. 2017;8:1029.
258. Dijkema J, Xue X, Harvey-Collard P, Rimbach-Russ M, de Snoo SL, Zheng G, Sammak A, Scappucci G, Vandersypen LM. Cavity-mediated iSWAP oscillations between distant spins. *Nat Phys* 2024:21;168–174.
259. Dehollain JP, Simmons S, Muhonen JT, Kalra R, Laucht A, Hudson F, Itoh KM, Jamieson DN, McCallum JC, Dzurak AS, et al. Bell's inequality violation with spins in silicon. *Nat Nanotechnol*. 2016;11:242–246.
260. Reiner J, Chung Y, Misha SH, Lehner C, Moehle C, Poulos D, Monir S, Charde KJ, Macha P, Kranz L, et al. High-fidelity initialization and control of electron and nuclear spins in a four-qubit register. *Nat Nanotechnol*. 2024;19:605–611.
261. Hollenberg LCL, Greentree AD, Fowler AG, Wellard CJ. Two-dimensional architectures for donor-based quantum computing. *Phys Rev B*. 2006;74(4):Article 045311.
262. O'Gorman J, Nickerson NH, Ross P, Morton JJL, Benjamin SC. A silicon-based surface code quantum computer. *npj Quantum Inf*. 2016;2:15019.
263. Donnelly MB, Keizer JG, Chung Y, Simmons MY. Monolithic three-dimensional tuning of an atomically defined silicon tunnel junction. *Nano Lett*. 2021;21:10092–10098.
264. Koch M, Keizer JG, Pakkiam P, Keith D, House MG, Peretz E, Simmons MY. Spin readout in atomic qubits in an all-epitaxial three-dimensional transistor. *Nat Nanotechnol*. 2019;14:137–140.
265. Salfi J, Mol JA, Rahman R, Klimeck G, Simmons MY, Hollenberg LCL, Rogge S. Quantum simulation of the Hubbard model with dopant atoms in silicon. *Nat Commun*. 2016;7:11342.
266. Kiczynski M, Gorman SK, Geng H, Donnelly MB, Chung Y, He Y, Keizer JG, Simmons MY. Engineering topological states in atom-based semiconductor quantum dots. *Nature*. 2022;606:694–699.
267. Le NH, Fisher AJ, Curson NJ, Ginossar E. Topological phases of a dimerized fermi–Hubbard model for semiconductor nano-lattices. *npj Quantum Inf*. 2020;6:24.
268. Mikhail D, Voisin B, St Medar DD, Buchs G, Rogge S, Rachel S. Quasiparticle excitations in a one-dimensional interacting topological insulator: Application for dopant-based quantum simulation. *Phys Rev B*. 2022;106(19):Article 195408.
269. Le NH, Fisher AJ, Ginossar E. Extended Hubbard model for mesoscopic transport in donor arrays in silicon. *Phys Rev B*. 2017;96(24):Article 245406.
270. Wang X, Khatami E, Fei F, Wyrick J, Namboodiri P, Kashid R, Rigosi AF, Bryant G, Silver R. Experimental realization of an extended fermi-Hubbard model using a 2D lattice of dopant-based quantum dots. *Nat Commun*. 2022;13:6824.
271. Taylor JM, Engel HA, Dür W, Yacoby A, Marcus CM, Zoller P, Lukin MD. Fault-tolerant architecture for quantum

computation using electrically controlled semiconductor spins. *Nat Phys*. 2005;1:177.
272. Seidler I, Struck T, Xue R, Focke N, Trellenkamp S, Bluhm H, Schreiber LR. Conveyor-mode single-electron shuttling in Si/SiGe for a scalable quantum computing architecture. *npj Quantum Inf*. 2022;8:100.
273. Huang P, Hu X. Spin qubit relaxation in a moving quantum dot. *Phys Rev B*. 2013;88:Article 075301.
274. Zhao X, Huang P, Hu X. Doppler effect induced spin relaxation boom. *Sci Rep*. 2016;6(1):23169.
275. Noiri A, Takeda K, Nakajima T, Kobayashi T, Sammak A, Scappucci G, Tarucha S. A shuttling-based two-qubit logic gate for linking distant silicon quantum processors. *Nat Commun*. 2022;13:5740.
276. Langrock V, Krzywda JA, Focke N, Seidler I, Schreiber LR, Cywiński Ł. Blueprint of a scalable spin qubit shuttle device for coherent mid-range qubit transfer in disordered Si/SiGe/SiO_2. *PRX Quantum*. 2023;4(2):Article 020305.
277. Zwerver A, Amitonov S, de Snoo S, Mądzik M, Rimbach-Russ M, Sammak A, Scappucci G, Vandersypen L. Shuttling an electron spin through a silicon quantum dot Array. *PRX Quantum*. 2023;4(3):Article 030303.
278. Struck T, Volmer M, Visser L, Offermann T, Xue R, Tu JS, Trellenkamp S, Cywinski L, Bluhm H, Schreiber LR. Spin-EPR-pair separation by conveyor-mode single electron shuttling in Si/SiGe. *Nat Commun*. 2024;15:1325.
279. Xue R, Beer M, Seidler I, Humpohl S, Tu JS, Trellenkamp S, Struck T, Bluhm H, Schreiber LR. Si/SiGe QuBus for single electron information-processing devices with memory and micron-scale connectivity function. *Nat Commun*. 2024;15:2296.
280. De Smet M, Matsumoto Y, Zwerver AMJ, Tryputen L, Snoo SL de, Amitonov SV, Sammak A, Samkharadze N, Gül Ö, Wasserman RNM, et al. High-fidelity single-spin shuttling in silicon. arXiv. 2024. https://doi.org/10.48550/arXiv.2406.07267
281. Jadot B, Mortemousque PA, Chanrion E, Thiney V, Ludwig A, Wieck AD, Urdampilleta M, Bäuerle C, Meunier T. Distant spin entanglement via fast and coherent electron shuttling. *Nat Nanotechnol*. 2021;5(16):570–575.
282. Delsing P, Cleland AN, Schuetz MJA, Knörzer J, Giedke G, Cirac JI, Srinivasan K, Wu M, Balram KC, Bäuerle C, et al. The 2019 surface acoustic waves roadmap. *J Phys D Appl Phys*. 2019;52:Article 353001.
283. Zheng G, Samkharadze N, Noordam ML, Kalhor N, Brousse D, Sammak A, Scappucci G, Vandersypen LMK. Rapid gate-based spin read-out in silicon using an on-chip resonator. *Nat Nanotechnol*. 2019;14(8):742–746.
284. Ibberson DJ, Lundberg T, Haigh JA, Hutin L, Bertrand B, Barraud S, Lee CM, Stelmashenko NA, Oakes GA, Cochrane L, et al. Large dispersive interaction between a CMOS double quantum dot and microwave photons. *PRX Quantum*. 2021;2(2):Article 020315.
285. Jouanny V, Frasca S, Weibel VJ, Peyruchat L, Scigliuzzo M, Oppliger F, De Palma F, Sbroggio D, Beaulieu G, Zilberberg O, et al. Band engineering and study of disorder using topology in compact high kinetic inductance cavity arrays. arXiv. 2024. https://doi.org/10.48550/arXiv.2403.18150
286. Benito M, Mi X, Taylor JM, Petta JR, Burkard G. Input-output theory for spin-photon coupling in Si double quantum dots. *Phys Rev B*. 2017;96(23):Article 235434.
287. Haikka P, Kubo Y, Bienfait A, Bertet P, Mølmer K. Proposal for detecting a single electron spin in a microwave resonator. *Phys Rev A*. 2017;95(2):Article 022306.
288. Hu X, Yx L, Nori F. Strong coupling of a spin qubit to a superconducting stripline cavity. *Phys Rev B*. 2012;86(3):Article 035314.
289. Samkharadze N, Bruno A, Scarlino P, Zheng G, Divincenzo DP, Dicarlo L, Vandersypen LMK. High-kinetic-inductance superconducting nanowire resonators for circuit QED in a magnetic field. *Phys Rev Appl*. 2016;5(4):Article 044004.
290. Grünhaupt L, Spiecker M, Gusenkova D, Maleeva N, Skacel ST, Takmakov I, Valenti F, Winkel P, Rotzinger H, Wernsdorfer W, et al. Granular aluminium as a superconducting material for high-impedance quantum circuits. *Nat Mater*. 2019;18:816–819.
291. Janík M, Roux K, Espinosa CB, Sagi O, Baghdadi A, Adletzberger T, Calcaterra S, Botifoll M, Manjón AG, Arbiol J, et al. Strong charge-photon coupling in planar germanium enabled by granular aluminium superinductors. *Nat Commun*. 2025;16(1):2103.
292. Stockklauser A, Scarlino P, Koski JV, Gasparinetti S, Andersen CK, Reichl C, Wegscheider W, Ihn T, Ensslin K, Wallraff A. Strong coupling cavity QED with gate-defined double quantum dots enabled by a high impedance resonator. *Phys Rev X*. 2017;7(1):Article 011030.
293. Harvey-Collard P, Dijkema J, Zheng G, Sammak A, Scappucci G, Vandersypen LMK. Coherent spin-spin coupling mediated by virtual microwave photons. *Phys Rev X*. 2022;12(2):Article 021026.
294. Mi X, Benito M, Putz S, Zajac DM, Taylor JM, Burkard G, Petta JR. A coherent spin photon interface in silicon. *Nature*. 2018;555(7698):599–603.
295. Samkharadze N, Zheng G, Kalhor N, Brousse D, Sammak A, Mendes UC, Blais A, Scappucci G, Vandersypen LMK. Strong spin-photon coupling in silicon. *Science*. 2018;359(6380):1123–1127.
296. Palma FD, Oppliger F, Jang W, Bosco S, Janík M, Calcaterra S, Katsaros G, Isella G, Loss D, Scarlino P. Strong hole-photon coupling in planar Ge: Probing the charge degree and Wigner molecule states. *Nat Commun*. 2023;15:10177.
297. Kang Y, Li ZH, Kong ZZ, Li FG, Hao TY, Wei ZC, Deng SY, Wang BC, Li HO, Wang GL, et al. Coupling of a hole double quantum dot in planar germanium to a microwave cavity. *Phys Rev Appl*. 2024;22(2):Article 024054.
298. Ungerer JH, Pally A, Kononov A, Lehmann S, Ridderbos J, Potts PP, Thelander C, Dick KA, Maisi VF, Scarlino P, et al. Strong coupling between a microwave photon and a singlet-triplet qubit. *Nat Commun*. 2024;15:1068.
299. Landig AJ, Koski JV, Scarlino P, Mendes UC, Blais A, Reichl C, Wegscheider W, Wallraff A, Ensslin K, Ihn T. Coherent spin–photon coupling using a resonant exchange qubit. *Nature*. 2018;560:179–184.
300. Corrigan J, Harpt B, Holman N, Ruskov R, Marciniec P, Rosenberg D, Yost D, Das R, Oliver WD, McDermott R, et al. Longitudinal coupling between a $Si/Si_{1-x}Ge_x$ double quantum dot and an off-chip TiN resonator. *Phys Rev Appl*. 2023;20(6):Article 064005.
301. Van Woerkom DJ, Scarlino P, Ungerer JH, Müller C, Koski JV, Landig AJ, Reichl C, Wegscheider W, Ihn T, Ensslin K, et al. Microwave photon-mediated interactions between semiconductor qubits. *Phys Rev X*. 2018;8(4):Article 041018.

302. Wang B, Lin T, Li H, Gu S, Chen M, Guo G, Jiang H, Hu X, Cao G, Guo G. Correlated spectrum of distant semiconductor qubits coupled by microwave photons. *Sci Bull*. 2021;66(4):332–338.
303. Scarlino P, Van Woerkom DJ, Mendes UC, Koski JV, Landig AJ, Andersen CK, Gasparinetti S, Reichl C, Wegscheider W, Ensslin K, et al. Coherent microwave-photon-mediated coupling between a semiconductor and a superconducting qubit. *Nat Commun*. 2019;10:3011.
304. Lin T, Gu SS, Xu YQ, Jiang SL, Ye SK, Wang BC, Li HO, Guo GC, Zou CL, Hu X, et al. Collective microwave response for multiple gate-defined double quantum dots. *Nano Lett*. 2023;23:4176–4182.
305. Borjans F, Croot XG, Mi X, Gullans MJ, Petta JR. Resonant microwave-mediated interactions between distant electron spins. *Nature*. 2020;577(7789):195–198.
306. Jnane H, Undseth B, Cai Z, Benjamin SC, Koczor B. Multicore quantum computing. *Phys Rev Appl*. 2022;18(4):Article 044064.
307. Unseld FK, Undseth B, Raymenants E, Matsumoto Y, Karwal S, Pietx-Casas O, Ivlev AS, Meyer M, Sammak A, Veldhorst M, et al. Baseband control of single-electron silicon spin qubits in two dimensions. arXiv. 2024. https://doi.org/10.48550/arXiv.2412.05171
308. Tadokoro M, Nakajima T, Kobayashi T, Takeda K, Noiri A, Tomari K, Yoneda J, Tarucha S, Kodera T. Designs for a two-dimensional Si quantum dot array with spin qubit addressability. *Sci Rep*. 2021;11(1):19406.
309. Pauka SJ, Das K, Kalra R, Moini A, Yang Y, Trainer M, Bousquet A, Cantaloube C, Dick N, Gardner GC, et al. A cryogenic CMOS chip for generating control signals for multiple qubits. *Nat Electron*. 2021;4:64–70.
310. Yu X, Wilhelm B, Holmes D, Vaartjes A, Schwienbacher D, Nurizzo M, Kringhøj A, van Stein MR, Jakob AM, Gupta P, et al. Schrödinger cat states of a nuclear spin qudit in silicon. *Nat Phys*. 2025;21:362–367.
311. Berkman IR, Lyasota A, Boo GG de, Bartholomew JG, Lim SQ, Johnson BC, McCallum JC, Xu BB, Xie S, Abrosimov NV, et al. Millisecond electron spin coherence time for erbium ions in silicon. arXiv. 2023. https://doi.org/10.48550/arXiv.2307.10021
312. Morse KJ, Abraham RJS, DeAbreu A, Bowness C, Richards TS, Riemann H, Abrosimov NV, Becker P, Pohl HJ, Thewalt MLW, et al. A photonic platform for donor spin qubits in silicon. *Sci Adv*. 2017;3:Article e1700930.
313. Koch T, Godfrin C, Adam V, Ferrero J, Schroller D, Glaeser N, Kubicek S, Li R, Loo R, Massar S, et al. Industrial 300 mm wafer processed spin qubits in natural silicon/silicon-germanium. arXiv. 2024. https://doi.org/10.48550/arXiv.2409.12731
314. Kong Z, Li Z, Cao G, Su J, Zhang Y, Liu J, Liu J, Ren Y, Li H, Wei L, et al. Undoped strained Ge quantum well with ultrahigh mobility of two million. *ACS Appl Mater Interfaces*. 2023;15(23):28799–28805.
315. Degli Esposti D, Paquelet Wuetz B, Fezzi V, Lodari M, Sammak A, Scappucci G. Wafer-scale low-disorder 2DEG in 28Si/SiGe without an epitaxial Si cap. *Appl Phys Lett*. 2022;120(18):Article 184003.
316. Paquelet Wuetz B, Degli Esposti D, Zwerver AMJ, Amitonov SV, Botifoll M, Arbiol J, Sam-mak A, Vandersypen LMK, Russ M, Scappucci G. Reducing charge noise in quantum dots by using thin silicon quantum wells. *Nat Commun*. 2023;14(1):1385.
317. Wang G, Song ZG, Luo JW, Li SS. Origin of giant valley splitting in silicon quantum wells induced by superlattice barriers. *Phys Rev B*. 2022;105(16):Article 165308.
318. Gonzalez-Zalba MF, Franceschi S, Charbon E, Meunier T, Vinet M, Dzurak AS. Scaling silicon-based quantum computing using CMOS technology. *Nat Electron*. 2021;4(12):872–884.
319. Wang Z, Feng M, Serrano S, Gilbert W, Leon RCC, Tanttu T, Mai P, Liang D, Huang JY, Su Y, et al. Jellybean quantum dots in silicon for qubit coupling and on-chip quantum chemistry. *Adv Mater*. 2023;35(19):2208557.
320. Sigillito AJ, Gullans MJ, Edge LF, Borselli M, Petta JR. Coherent transfer of quantum information in a silicon double quantum dot using resonant SWAP gates. *npj Quantum Inf*. 2019;5(1):110.
321. Mi X, Cady JV, Zajac DM, Deelman PW, Petta JR. Strong coupling of a single electron in silicon to a microwave photon. *Science*. 2017;355(6321):156–158.
322. West A, Hensen B, Jouan A, Tanttu T, Yang CH, Rossi A, Gonzalez-Zalba MF, Hudson F, Morello A, Reilly DJ, et al. Gate-based single-shot readout of spins in silicon. *Nat Nanotechnol*. 2019;14(5):437–441.
323. Urdampilleta M, Niegemann DJ, Chanrion E, Jadot B, Spence C, Mortemousque PA, Bäuerle C, Hutin L, Bertrand B, Barraud S, et al. Gate-based high fidelity spin readout in a CMOS device. *Nat Nanotechnol*. 2019;14(8):737–741.
324. Takeda K, Noiri A, Nakajima T, Yoneda J, Kobayashi T, Tarucha S. Quantum tomography of an entangled three-qubit state in silicon. *Nat Nanotechnol*. 2021;16(9):965–969.
325. Fernández de Fuentes I, Botzem T, Johnson MAI, Vaartjes A, Asaad S, Mourik V, Hudson FE, Itoh KM, Johnson BC, Jakob AM, et al. Navigating the 16-dimensional Hilbert space of a high spin donor qudit with electric and magnetic fields. *Nat Commun*. 2024;15:1380.
326. Ciriano-Tejel VN, Fogarty MA, Schaal S, Hutin L, Bertrand B, Ibberson L, Gonzalez-Zalba MF, Li J, Niquet YM, Vinet M, et al. Spin readout of a CMOS quantum dot by gate reflectometry and spin-dependent tunneling. *PRX Quantum*. 2021;2(1):Article 010353.
327. Struck T, Hollmann A, Schauer F, Fedorets O, Schmidbauer A, Sawano K, Riemann H, Abrosimov NV, Cywiński Ł, Bougeard D, et al. Low-frequency spin qubit energy splitting noise in highly purified ^{28}Si/SiGe. *npj Quantum Inf*. 2020;6(1):40.
328. Chanrion E, Niegemann DJ, Bertrand B, Spence C, Jadot B, Li J, Mortemousque PA, Hutin L, Maurand R, Jehl X, et al. Charge detection in an array of CMOS quantum dots. *Phys Rev Appl*. 2020;14(2):Article 024066.
329. Tenberg SB, Asaad S, Mądzik MT, Johnson MA, Joecker B, Laucht A, Hudson FE, Itoh KM, Jakob AM, Johnson BC, et al. Electron spin relaxation of single phosphorus donors in metal-oxide-semiconductor nanoscale devices. *Phys Rev B*. 2019;99(20):Article 205306.